Simulating the effects of cosmic rays on the interstellar medium: outflows, phase structure and shocks

Masterarbeit

zur Erlangung des akademischen Grades
Master of Science
im Studiengang Astrophysics
der Mathematisch-Naturwissenschaftlichen Fakultät
der Universität Potsdam
in Zusammenarbeit mit dem
Leibniz Institut für Astrophysik Potsdam (AIP)

vorgelegt von
Alexander Gerhard Scherrmann

Potsdam, Januar 2020

Betreuer: Dr. Philipp Girichidis

Erstgutachter: Prof. Dr. Christoph Pfrommer

Zweitgutachter: Prof. Dr. Philipp Richter

Selbsständigkeitserklärung
Ich versichere hiermit, dass ich die vorliegende Arbeit
selbstständig verfasst und keine anderen als die
angegebenen Quellen und Hilfsmittel benutzt habe.

Potsdam, den 28. Januar 2020   (Alexander Gerhard Scherrmann)

Abstract

We study the effect of cosmic rays (CRs) injected by supernova (SN) feedback on the structure and outflows from a simplified interstellar medium (ISM) with solar neighborhood conditions, i.e. with a gas surface density of $\Sigma_{\mathrm{gas}} = 10\, M_\odot\, \mathrm{pc}^{-2}$. Therefore we run three-dimensional magnetohydrodynamical simulations, using the unstructured mesh code AREPO, in which we treat CRs as a relativistic fluid in the advection-diffusion approximation. Our setup includes an external gravitational potential, magnetic fields, radiative cooling and SN feedback in terms of local energy injection. We do not account for molecular gas, self-gravity, background radiation nor shearing at the boundaries by galactic rotation. We model anisotropic diffusion along the magnetic field lines using different diffusion coefficients ranging from $D = 10^{28}$-$10^{29}\, \mathrm{cm}^2\, \mathrm{s}^{-1}$ and consider different amounts of the total SN energy injected into CRs, namely 5, 10 and 20%. Further we apply a shock finding routine that accelerates CRs at shock fronts originating from SNe in three additional runs. We find very comparable ISM phases and structures independent of the different diffusion coefficients and CR injection fractions. The CR energy distribution along the z-coordinate is mainly determined by the applied CR injection fraction and the CR scale height, i.e. where the integrated CR energy reaches 70%, by the diffusion coefficient. Over time the runs with smaller diffusion coefficient drive slightly more total mass away from the galactic plane with mass loading factors, i.e. the ratio of outflowing mass and star formation rate, $\eta \sim 0.1$-8. First results by the applied shock finding routine indicate the applicability of such a routine as they yield comparable structures, CR energies and outflows to the simulations with CR injection.

Kurzzusammenfassung

Wir untersuchen den Effekt von kosmischer Strahlung (CRs), die in Supernovae (SN) entspringen auf die Struktur und Ausflüsse von einem vereinfachten interstellarem Medium (ISM) in Bedingungen die dem Umfeld der Sonne ähnlich sind, mit einer Oberflächendichte des Gases von $\Sigma_{\mathrm{gas}} = 10\, M_\odot\, \mathrm{pc}^{-2}$. Dazu nutzen wir den unstrukturierten Gitter Simulationscode AREPO um dreidimensionale magnetohydrodynamische Simulationen zu berechnen, in denen wir CRs als relativistisches Fluid in der Advektion-Diffusions Näherung behandeln. Unser Setup beinhaltet ein externes Gravitationspotential, Magnetfelder und SNe durch lokale Energieeinführung. Wir berücksichtigen kein molekulares Gas, Eigengravitation, Hintergrundstrahlung oder Scheereffekte, die durch die galactische Rotation induziert werden. Wir modellieren anisotrope Diffusion entlang der Magnetfeldlinien mit verschiedenen Diffusionskoeffizienten von 10^{28}-$10^{29}\, \mathrm{cm}^2\, \mathrm{s}^{-1}$ und berücksichtigen verschiedene Energiebeträge der gesamten SN-Energie die in CR gesteckt wird, 5, 10 und 20%. Zusätzlich wenden wir in drei weiteren Simulationen eine Schock-Detektions Routine an, die CRs an Schockfronten, die bei SNe entstehen, beschleunigt. Wir finden sehr vergleichbare Phasen und Strukturen des ISM, unabhängig von dem verwendeten Diffusionskoeffizienten und den hinzugefügten CR-Energien. Die Energieverteilung der CR entlang der z-Koordinate ist hauptsächlich durch den Betrag der hinzugefügten CR-Energie und

die Skalenhöhe der CRs, bei der die integrierte CR-Energie 70% der Gesamtenergie erreicht, durch den gewählten Diffusionskoeffizienten bestimmt. Über die Simulationszeit hinweg weisen die Simulationen mit kleineren Diffusionskoeffizienten eine höhere von der Galaktischenebene transportierte Masse auf. Dabei erhalten wir Masseladefaktoren, das Verhältnis von Massenausfluss- und Sternenformationsrate, von $\eta \sim 0.1$-8. Die ersten Resultate der Schock-Detektions Routine zeigen die Anwendbarkeit einer solchen Methode, da diese Simulationen sehr ähnliche Strukturen, CR-Energien und Ausflüsse aufweisen wie die anderen Simulationen.

Contents

1 Introduction

The interstellar medium (ISM) is a well studied, but complex and not yet fully understood regime in astrophysics. It is of particular interest as it covers large temperature and dynamical ranges over several orders of magnitude. It involves the life cycle of matter within galaxies, including gas in its various phases, i.e. cold, warm and hot, and different states, i.e. atomic, ionized and molecular. Latter state is of special importance as a correlation between star formation and presence of molecular gas has been observed (Krumholz & McKee, 2005; Krumholz & Thompson, 2007) and further investigated by e.g. Glover & Clark (2012). The ISM is the birth place of stars, which themselves strongly impact the dynamics in the ISM by stellar feedback, i.e. radiation, stellar winds and in case of more massive stars additionally by supernova explosions (Rogers & Pittard, 2013; Gatto et al., 2015; Geen et al., 2015; Haid et al., 2016; Gatto et al., 2017; Rahner et al., 2017).

These high energy releasing events induce ISM turbulence and are one of the most efficient sources of driving outflows, fountain flows (de Avillez & Breitschwerdt, 2004, 2005; Joung et al., 2009; Kim et al., 2011, 2013; Gatto et al., 2015; Walch et al., 2015; Girichidis et al., 2016b; Padoan et al., 2016; Gatto et al., 2016) and even galactic winds observed by e.g. Veilleux et al. (2005); Heckman & Thompson (2017). The outflows observed involve mass loading factors, i.e. the ratio of outflowing mass to star formation rate, ranging from 0.01-10 (Veilleux et al., 2005; Newman et al., 2012; Genzel et al., 2014; Heckman & Thompson, 2017).

The general idea and source for driving outflows is the overlapping of SN remnants which creates hot super bubbles ranging out of the galactic disk (Cox & Smith, 1974; McKee & Ostriker, 1977; Cox, 2005). Additionally to the high energy input by SN, they further enrich the surrounding ISM with metals produced inside the stars during their lifetime.

Thus the outflowing gas is observed in all its phases, the ionized one by e.g. Pettini et al. (2001); Heckman et al. (2015); Chisholm et al. (2017). Neutral gas outflows have been reported by e.g. Heckman et al. (2000); Rupke et al. (2005); Contursi et al. (2013) and even molecular gas has been detected in outflows e.g. Weiß et al. (1999); Leroy et al. (2015); Chisholm & Matsushita (2016). Numerical studies of a SN driven ISM have confirmed the multiphase outflowing gas character (Walch et al., 2015; Girichidis et al., 2016b; Li et al., 2017; Kim & Ostriker, 2018) and the powering of galactic winds (Marinacci et al., 2013; Aumer et al., 2014; Hopkins et al., 2014; Schaye et al., 2014; Hu et al., 2016).

However theoretical studies by e.g. Breitschwerdt et al. (1993); Dorfi & Breitschwerdt (2012) have shown the possibility of non-thermal, i.e. cosmic ray (CR), pressure gradients are able to launch outflows which was confirmed by Hanasz et al. (2013). Additionally Girichidis et al. (2016a) have shown the importance of CRs, as thermal feedback alone is

not sufficient to drive strong outflows and reproduce the observed structures within the galactic plane. Therefore CRs are essential for modeling the ISM and galaxies.

CRs are charged particles with large kinetic energies ranging from MeV to EeV, where the largest part of the total CR energy is found in protons of a few GeV (Strong et al., 2007; Grenier et al., 2015). CR gain their energy by either first order Fermi process, i.e. diffusive shock acceleration, at collisionless magnetized shocks, mainly at SN remnants (Axford et al., 1977; Bell, 1978; Blandford & Ostriker, 1978; Schlickeiser, 1989) or second order Fermi process, by scattering of magnetic irregularities. The net energy gain by the first process equals roughly to 10% of the released SN energy, which is transferred into the non-thermal CR component (Helder et al., 2012; Morlino & Caprioli, 2012; Ackermann et al., 2013). Overall CRs cool less efficient than thermal gas (Enßlin et al., 2007; Jubelgas et al., 2008) and occupy an average energy density of $\sim 1\,\mathrm{eV}$ which results them in being in energy equipartition with thermal gas and magnetic fields (Boulares & Cox, 1990; Cox, 2005).

CRs travel diffusely through the galactic magnetic field (Macdonald & Brown, 1972) and overall within their transport they can be treated as a fluid due to scattering of magnetic irregularities (Zweibel, 2013, 2017). Observations of a decreasing B/C ratio with particle energy per nucleon indicate an energy dependent diffusion coefficient (Blasi, 2013). Observations of particles with energies of $10\,\mathrm{GeV}$ per nucleon yield diffusion coefficients of $D(E) \approx 3 \times 10^{28}(\mathrm{H}/(3\,\mathrm{kpc}))\,\mathrm{cm}^2\,\mathrm{s}^{-1}$, with scale height H, and $D \approx 10^{29}\,\mathrm{cm}^2\,\mathrm{s}^{-1}$ for an escaping particle of energy $1\,\mathrm{GeV}$ and H set to $3\,\mathrm{kpc}$ (Blasi, 2013).

The usage of an energy depend diffusion coefficient requires additional computation and therefore most studies constrain the anisotropic diffusion coefficient to 10^{28}-$10^{29}\,\mathrm{cm}^2\,\mathrm{s}^{-1}$ depending on the models used. To perhaps constrain this we study the effect of three different diffusion coefficients $D = 10^{28}\,\mathrm{cm}^2\,\mathrm{s}^{-1}$, $D = 3 \times 10^{28}\,\mathrm{cm}^2\,\mathrm{s}^{-1}$ and $D = 10^{29}\,\mathrm{cm}^2\,\mathrm{s}^{-1}$ on outflows from, CR energy distribution and structure in a simplified ISM.

In most studies CRs sources are included by CR energy injection at SN events with 10% of the SN energy. The physical process of CR acceleration at the SN shock wave during the Sedov-Taylor phase is not resolved in galaxy or cosmological simulations. In our simulations we are able to resolve the individual Sedov-Taylor phases of SNe and therefore apply a shock finding routine developed by Schaal & Springel (2014), that detects the shocks and accelerates CRs rather than inject them with thermal energy directly in the SN events. To classify the results of the shock finder we first ran simulations with different CR injection fractions, i.e. we make use of the broadly used CR energy injection at SN events with different fractions being deposited in CRs, 5%, 10% and 20%. Thereby we further combine the different diffusion coefficients and CR injection fractions to study their impact on the ISM. For our simulations we use the unstructured mesh code AREPO developed by Springel (2010).

The thesis is structured as follows: Chapter 2 first provides an introduction to the ISM, CRs and in the numerical methodology before presenting the used simulation code AREPO. The following chapter presents our used setup consisting of the initial conditions, the SN positions and adaptations in the code. An overview of our simulations and their results are stated in chapter 4, which are then discussed summarized in chapter 5 and 6.

2 Theoretical Background

This chapter covers all basic knowledge for the physical processes in this work. It is split up as follows: 2.1 provides an overall knowledge about the structures, phases, components and dynamics of the ISM, where we mainly follow Klessen & Glover (2016). The most important component for this work, the cosmic rays (CRs) are addressed their own section 2.2. Section 2.3 introduces the conservation equations, assuming idealized magnetohydrodynamics (MHD), and how we solve them, before we introduce the simulation code AREPO in 2.4.

2.1 Interstellar Medium (ISM)

Unlike the first image/believes of an empty space between stars in the galaxy, the medium in the galaxy is filled up with atoms, molecules and dust. This medium is called the interstellar medium (ISM). Large fractions are dark and only investigatable by background stars. There are various structures in between that are observable such as HII regions, supernova (SN) remnants and (molecular) clouds.
The ISM consists mainly of 75% atomic hydrogen, 25 % helium and a small fraction of heavier elements. All of them have fractions of neutral, ionized or molecular form and are manifested in their gaseous state. There are various gaseous phases that characterize the ISM: cold molecular clouds, HI clouds, warm gas between clouds and hot coronal gas. Energy and heating sources of the gas are photons that originate from the stars, cosmic rays (CRs) and X-rays emitted by local hot gas. In galaxy evolution the ISM plays a central role with its phases as it is the storage of building material for new stars. This material is refilled by the previous stellar generations that launched winds and for some ended in a supernova explosion (SN). A fraction of the metal enriched gas is then used as foundation of the a new generation of stars. This recycling and enrichment of the ISM drives the galactic evolution.
Although the matter is spread diffusely and inhomogeneously in terms of total weight of the galactic disk the ISM accounts for 10-15%. Inside the Milky Way stars are separated by some 2 pc, within the solar neighborhood and a stellar density $\rho_\star = 6 \times 10^{-2}\,\mathrm{pc}^{-3}$). The ISM hosts in various structures like HII regions, dark clouds and SN remnants.

2.1.1 Composition of the ISM

The constituents of interstellar matter are determined by the galactic evolution. The ISM matter consists of 70.4% hydrogen (mass), 28.1% helium and 1.5% of metals. However

there is more than just matter in the ISM. It consists of 5 different components that all interact and influence each other: gas, dust grains, cosmic rays (CRs), magnetic fields and radiation (fields).

Interstellar gas

The gas in the ISM is concentrated within the galactic plane and along spiral arms. However on small scales it is spread inhomogeneously. About 50% of the ISM mass is found in cool molecular clouds that occupy 1-2% of the volume. These are either very cold clouds ($T \sim 10\,\mathrm{K}$) or cold ones ($T \sim 100\,\mathrm{K}$). Due to high densities of the clouds they only occupy 1-2% of the totals volume. Further high densities prevent ionizing photons reaching deeply into the clouds. Hence they consist mostly of neutral molecules. Clouds are distinguished by whether they contain more elements in their atomic or molecular state. The remaining gas is found in either neutral or ionized states, which are referred as different phases (see 2.1.2). The coolest and densest clouds form densities up to 10^{-20}-$10^{-18}\,\mathrm{g\,cm^{-3}}$. In contrast to cloud densities, the hot medium has lower densities of order $\sim 10^{-26}\,\mathrm{g\,cm^{-3}}$. The warm phase consisting of (mostly neutral) atomic gas, the warm and ionized phase ($\mathrm{T} \sim 10^4\,\mathrm{K}$) or the hot ionized phase $\mathrm{T} \sim 10^6\,\mathrm{K}$. It covers a wide range of densities and temperatures: dense cold gas $\rho \sim 10\,\mathrm{cm^{-3}}$ with $T < 100\,\mathrm{K}$, warm $\rho \sim 0.1 - 1\,\mathrm{cm^{-3}}$ with T of a few $1000\,\mathrm{K}$, coronal/hot $\rho < 0.01\,\mathrm{cm^{-3}}$ with $T > 10^5\,\mathrm{K}$. There is no real phase with $10^4\,\mathrm{K}$ as this belongs to fast cooling region, see below.

Dust

The reddening of star light cannot be explained entirely with atomic absorption alone. There is a further component contributing to the shift over a wide range of frequencies. This additional absorption has broad lines unlikely like atomic ones and heavy metals are only present in a negligible fraction. Additionally the absorption seems to be an almost perfect blackbody emission in the infrared component. Therefore the ISM must have an additional component rather than ionized, atomic or molecular ones. It has to have a particle like structure which is simply referred as dust.

Dust particles absorb light with smaller wavelength than their physical size. The overall absorption in the ultra violet and optical part of the spectrum leads to the conclusion that there are much more small dust grains than large ones. The characteristic of the absorption lines/ extinction curve allow an insight into the chemical composition of dust. Graphite and amorphous silicates are prominent particles in dust.

Dust contains an equal amount of metals as the gas phase. Even though dust contributes only to roughly 1% of the mass in the ISM its amount of metalicity makes it important factor for chemistry.

Cosmic Rays

Cosmic rays (CRs) are relativistic particles moving closely at the speed of light. They mainly consist of protons, 10% of helium nuclei, 1% heavier nuclei, 2% of electrons and
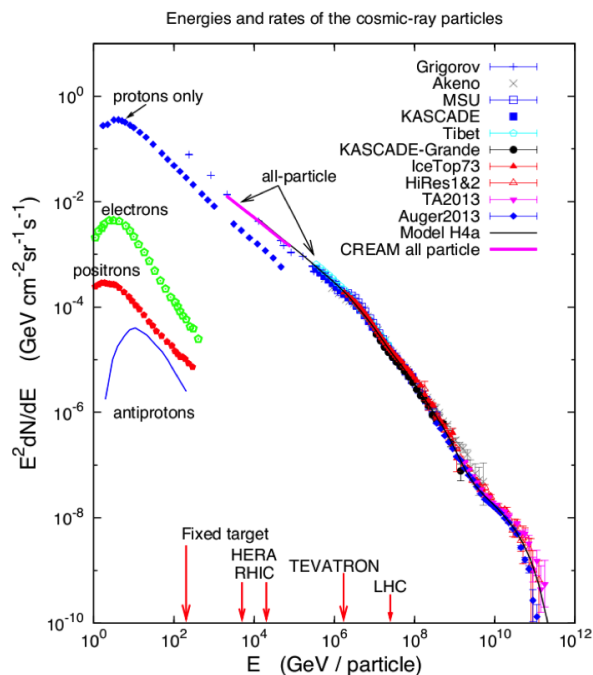
Figure 2.1: Spectral energy distribution of cosmic rays as observed on Earth from various observatories. Taken from (Klessen & Glover, 2016)

small fractions of positrons and antiprotons. As we observe on Earth they cover a wide range of kinetic energies as shown in figure 2.1. They are in equipartition with the gas and magnetic field with an energy density of $\sim 1\,\mathrm{eV\ cm^{-3}}$. CRs with energies below $0.1\,\mathrm{GeV/nucleon}$ originate from the sun, whereas more energetic CRs originate from our galaxy (up to $10^{15}\,\mathrm{eV}$ (up to the knee)) or extragalactic ISM $> 10^{15}\,\mathrm{eV}$. Because the Sun effects CRs below $1\,\mathrm{GeV/nucleon}$ the spectrum below that energy is still uncertain. At higher energies the energy spectrum follows a power law distribution with different exponents for different energy regimes of the spectrum. We recognize CRs in the ISM by the interactions with the ISM that produces γ-rays or produce molecular ions like H_3^+ which provide further constrains on the CR spectrum. More detailed information is provided in 2.2. CRs are accelerated in shocks or bouncing of magnetic irregularities. The strongest shocks are in SNe, but also in stellar wind shocks.

Magnetic field

The ISM is permeated by an irregular magnetic field. We know about the presence of the magnetic field by Zeemann splitting of absorption and emission lines and Faraday rotation. Overall it is orientated parallel to the galactic plane. Within the galactic disk its strength ranges from average $1\,\mu\mathrm{G}$ up to $5\,\mu\mathrm{G}$ generated by fluctuations. Even though its weak strength (compared to Earth's small magnetic field $\sim 0.3\,\mathrm{G}$) it strongly influences the dynamics and structures in the ISM, as it provides additional pressure support against

gravity. It controls the propagation of CRs and is essential for shaping the gas, except very neutral gas in star forming regions.

The origin of the magnetic field is not yet fully understood, but it is supposed to be maintained by a turbulent dynamo process. In this process ionized gas transfers part of its kinetic energy to the magnetic field. However a seed magnetic field is needed for the dynamo process. The seed field could originate from stellar magnetic fields that had been ejected into space. Another possibility is the presence of an extragalactic magnetic field when the galaxy was forming.

Radiation

Similar to the magnetic field the ISM is also permeated by a radiation field, the interstellar radiation. It covers the entire electromagnetic spectrum produced by various sources. The low frequency part of the spectrum is dominated by photons of synchrotron emission and the cosmic microwave background (CMB). These photons originate from the era of recombination and were redshifted by the expansion of the universe. The CMB is an almost perfect black-body spectrum at a temperature of $2.7\,\mathrm{K}$. The far and mid infrared part of the spectrum is dominated by emission of dust grains. They do absorbs light of the optical spectrum and reemits it at lower frequency. Star light dominates the range of near infrared to UV part of the spectrum, where more massive stars dominate the higher energetic part of the spectrum. The radiation field influences the ISM, especially the UV part. High energetic photons are able to either knock out electrons from atoms (ionization) or knock of electrons from dust grains which is referred to as photoelectric effect. In both cases the electrons transfer their kinetic to the surrounding gas thereby heating it. Thus the UV light plays are crucial role in the heating of gas (see also in 2.1.3). Further UV light is capable of breaking molecular bounds, i. e. photo dissociation of molecules.

2.1.2 Phases of the ISM

The ISM can be divided into different phases that describe the local characteristics of that particular region. They differ in their degree of ionization, density and temperature, see Table 2.1.

Two phase solution

If we assume purely atomic gas in the ISM, early developed models by Field et al. (1969) have shown that if thermal equilibrium is reached there are two stables solutions containing wide pressure ranges. The first is at temperature $T \sim 100\,\mathrm{K}$ referred to as cold neutral medium (CNM) that is in pressure equilibrium with the in contrast warm neutral medium (WNM) at $T \sim 10^4\,\mathrm{K}$, which is more diffuse than the CNM. The cooling of the gas suggests no separate stage in between, as the cooling function implies. By this the gas either cools down to the CNM or heats up to join the WNM.

However the initial two phase solution model was extended by McKee & Ostriker (1977)
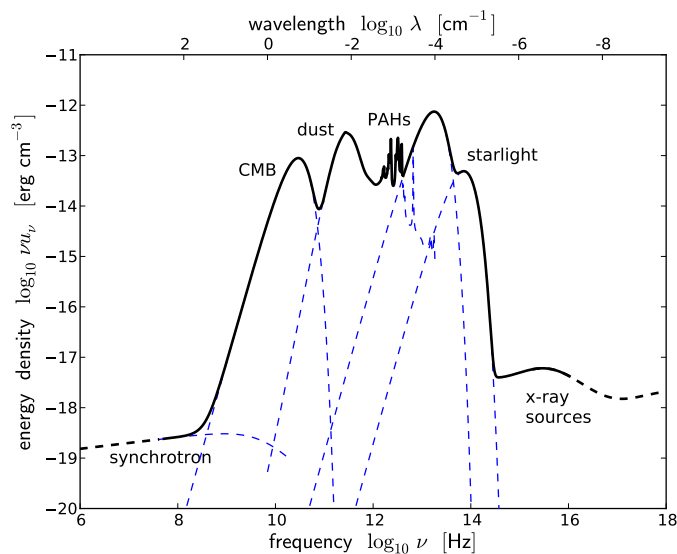
Figure 2.2: Total energy density distribution of interstellar radiation fields. Taken from (Klessen & Glover, 2016)

who included heating by SN that lead to a hot ionized gas state (HIM) with $T \sim 10^6$ K. In between the WNM and HIM there was found an additional phase by various observations of different processes e.g. (Hoyle & Ellis, 1963; Reynolds et al., 1973; Reynolds, 1989; Mierkiewicz et al., 2006; Gaensler et al., 2008). It is not as hot as the HIM but contains mostly ionized gas and is referred to as warm ionized medium (WIM), which's density is comparable to the WNM.

Last distinctions were made by Blitz et al. (2006) showing the presence of a fifth phase the molecular gas. The molecular gas is mostly bound in clouds of various sizes, surrounded by the slight warmer CNM.

Molecular gas

Molecular gas mainly contains molecular hydrogen. It is predominantly found in the inside gas clouds, where it is protected from UV radiation, that can dissociate the molecular bonds. The abundances of various molecules allow the gas to cool down to very low temperatures T of ~ 10 K, which further lead to high densities. Hence, self-gravity is important for shaping molecular regions and clouds. The most abundant molecules are H_2 and CO. Observations show a correlation between star formation and the existence of molecular gas (Klessen & Glover, 2016). Therefore the distribution of molecular gas is of special interest. Pineda et al. (2013) observed that inside the Milky Way, the molecular gas surface density peaks within a circle of 500 pc radius around the galactic center. Between 0.5-3 kpc the density steeply drops and increases and peaks again around 4-6 kpc. Further outside the density of molecular gas drops exponentially, but is traced out to 12-13 kpc (Heyer et al., 1998).

Table 2.1: Multiple ISM phases and their properties according to (Caselli et al., 1998; Ferriere, 2001; Wolfire et al., 2003; Jenkins, 2013; Klessen & Glover, 2016)

Component	Temperature [K]	Density [cm^{-3}]	Fractional ionization
Molecular gas	10-20	$> 10^2$	$< 10^{-6}$
Cold neutral medium (CNM)	50-100	20-50	$\sim 10^{-4}$
Warm neutral medium (WNM)	6000-10000	0.2-0.5	~ 0.1
Warm ionized medium (WIM)	~ 8000	0.2-0.5	1.0
Hot ionized medium (HIM)	$\sim 10^6$	$\sim 10^{-2}$	1.0

Cold neutral medium (CNM)

The CNM consists of neutral, cold and dense gas. This phase is formed within clouds. However, it differs from the molecular phase as the particles are in an atomic state. Overall it is less dense than the molecular gas because otherwise it would absorb UV light and be heated. Molecular clouds are surrounded by the CNM, as dissociative photons break the molecular bonds of the outer layers, transferring the gas into its atomic state. If clouds are not large or dense enough, the clouds can become fully atomic and are referred to as diffuse clouds.

Warm neutral medium (WNM)

Neutral gas with much lower densities and higher temperature than the CNM is called WNM. It is in pressure equilibrium with the CNM in the two phase model of the ISM. Observation have detected the WNM to be present in the outer parts of the galaxy (Kulkarni & Heiles, 1987) even out to 9-12 kpc from the galactic center with a scale height ~ 1 kpc (Carilli et al., 1998).

Warm ionized medium (WIM)

Gas surrounding stars is ionized by the star's UV radiation forming HII regions, these are not considered to be in the WIM. But not only the direct environment of stars is ionized, escaping UV radiation can pass through the gaseous vicinity and lead to ionization of extremely large and extended regions mainly within the halo of the galaxy with a scale height of order of 1 kpc (Reynolds, 1989). Haffner et al. (2009) observed that the majority ($\sim 90\%$ or more) of the ionized gas in the ISM is settled in the WIM.

Hot ionized medium (HIM)

Individual supernovae are capable of creating hot bubbles or even super bubbles if individual SNe overlap or are clustered. Furthermore, there are dilute and very high temperature regions. Connections of bubbles allow UV radiation to travel the galaxy allowing the creation of the WIM.
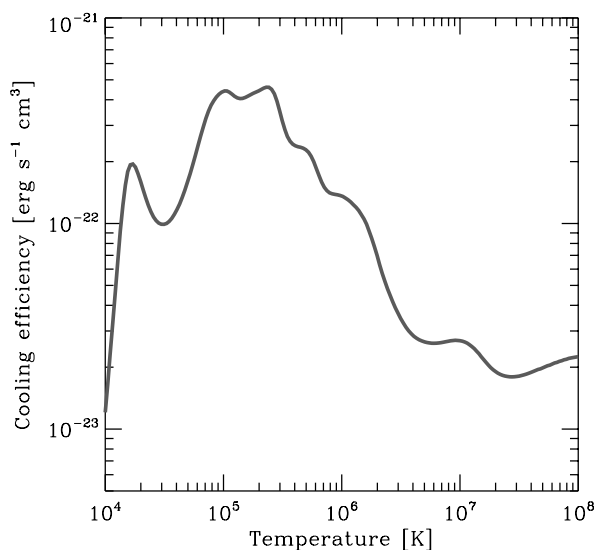
Figure 2.3: Cooling efficiency of thermal gas as function of gas temperature. Taken from (Klessen & Glover, 2016)

2.1.3 Heating and Cooling

There are many forms of heating and cooling within the ISM here we present the most prominent ones.

Cooling

Radiative cooling is one of many cooling mechanisms. It describes the loss of energy by radiation, i.e. photons. Atoms can get externally excited by collisions with other atoms or by photons. The stored energy is then released by emission of a photon that is then able to escape the environment, carrying that amount of energy with it away from the system. The efficiency of that process depends on the cooling rate Λ. The cooling rate is composed of the transition rate from excited to ground state, the energy of the transition and the number density of the excited state. With an analysis of the optically thin two-level atom it can be shown (e.g. (Klessen & Glover, 2016)), that the cooling rate Λ depends on the local atomic density. In low density regimes $\Lambda \propto n^2$ and in high density fields $\Lambda \propto n$.

Figure 2.3 shows the cooling efficiency of thermal gas adopted to the data of Gnat & Ferland (2012). The cooling of thermal gas is most efficient between 10^4-10^6 K, which explains that there are only minor gas fractions within that temperature range.

H_2 is the most abundant molecule in the ISM, one order of magnitude more abundant than other molecules. Even though it is the most abundant one its cooling rate is only important in shocks and is not efficient at low temperatures. Transitions between quantum states are really rare therefore the next possible transition is one with an equivalent temperature of 510 K. At very low temperatures this is very unlikely to occur, hence the cooling is inefficient.
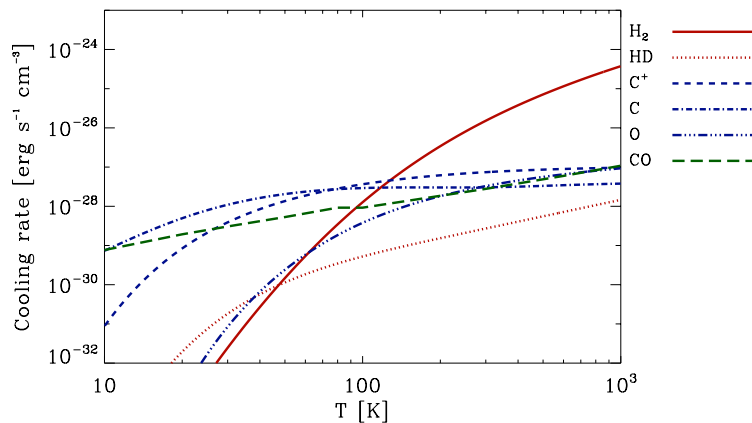
Figure 2.4: Comparison of cooling rates of different molecules at low temperature range. Taken from (Klessen & Glover, 2016)

Deuteride cools efficient at low temperatures, as the next excited state is at a temperature of 128 K. Nevertheless it has a very low abundance except for not fully molecular cold gas. Then it cools more efficient than H_2 even though it is 10^4 times less abundant than it. But both are not comparable to different types of carbon.

Carbon monoxide is the second most abundant molecule in the ISM and the best coolant at very low temperatures. At low densities the fine structure cooling from atomic carbon is more efficient and at temperatures below 20 K C^+ becomes more significant. Other molecules can play a role in cooling but the ones mentioned above are the most important ones. Figure 2.4 illustrates the the cooling rates of different coolants and shows the coolants properties mentioned above.

Heating

There are several heating processes in the ISM. There is the UV heating that either acts on molecular dissociation e.g. acting on H_2 which leads to a kinetic energy gain by the molecule that then is transferred into the gas. Another possibility is the so called UV pumping which is more common. The excited state decays into vibrationally excited state and frees the energy by collisional de-excitation, hence heats the gas. This process is faster than the radiative decay and thus more effective. This process becomes important at number densities around $10^4 \, cm^{-3}$ and is therefore the main heat source in clouds.

Another heat source are CRs. They play a crucial role in well shielded gas, the same as photoelectric heating. CR protons ionize gas particles and the additional energy is shared as kinetic energy between the ion and the freed electron. This can lead to secondary ionization on which the shared energy is transferred to the medium by collision and thereby heats it.

A similar but also important heating mechanism are X-rays. The process is similar to the heating by CRs. The ionization leads to secondary ionization but also the X-rays can be

absorbed as their mean free paths is much smaller. However this process is only really important in diffuse ISM or if dense gas is close to an X-ray source.

Molecules do not only play an important role in cooling but also in heating. The formation of molecular bonds leads to a release of energy. This energy is manifested in form of rotational/vibrational excitation of the newly formed molecule. That energy is then radiated away. In higher density regions collisional de-excitation takes over and produces heat. Of all molecules forming, the H_2 formation is the most dominant one, but yet still discussed on its efficiency.

The interstellar dynamics further provide a heat source. Gravity dominated regions show adiabatic compression (work load PdV) which can be locally the main source of heat. In supersonic gas flows turbulence dissipates energy down to the gas, which is known as shock heating.

Figure 2.5 shows the heating/ cooling as function of the number density n. Below a density of $2000\,\text{cm}^{-3}$ the photoelectric emission from dust dominates the field. In that range cooling is mostly caused by C^+. In the range of $2000\,\text{cm}^{-3}$ - $10^5\,\text{cm}^{-3}$ the rotational line emission by CO dominates the cooling. First photoelectric heating is dominant but then PdV takes over at $10^4\,\text{cm}^{-3}$ and at higher densities turbulence in shocks at CR heating take over. The coupling of gas to dust takes over at $10^5\,\text{cm}^{-3}$. The energy dissipated by turbulence is small on larger scales but can reach high values at small scales. Generally cooling depends on the present magnetic field. Within regions with a weak present field shocks dominate and energy is carried away by diffusion.

Another possibility of heating the gas is the well known photoelectric effect, referred as photoelectric heating. Here, the photoelectric effect acts on dust grains and frees electrons. That freed electron then transfers its energy to the gas and heats it. The efficiency depends on the ISRF, the size of dust grains and the charge of the grains. The charge matters as this determines the energy needed to free the electron, the size of the dust grains determines the interaction likelyhood and the ISRF has to have photons with the right frequency to free the electrons. Last but not least there is a coupling of gas and dust. Grains do play an important role in the cooling process as they are extremely good radiators. If the temperatures of the gas and dust are unequal there is a net energy flow from one to the other reservoir. If the dust temperatures exceeds the gas temperatures there is the energy flow from dust to gas, hence heating the gas. At lower densities that process is low compared to fine structure cooling and at high densities gas grains heating/cooling takes over such that the gas reaches the temperature equilibrium with the dust.

2.1.4 Life cycle of the ISM and galactic outflows

In the ISM the matter is constantly moved and influences various parts of the galaxy. The matter in the ISM originates to an extend from the local ISM but also a larger fraction originates from outside the galaxy. This is explained by the life cycle of the ISM

The cycle starts with new stars forming from the current matter supply in the ISM. Only a few regions in the ISM provide conditions to form new stars. High densities, very low
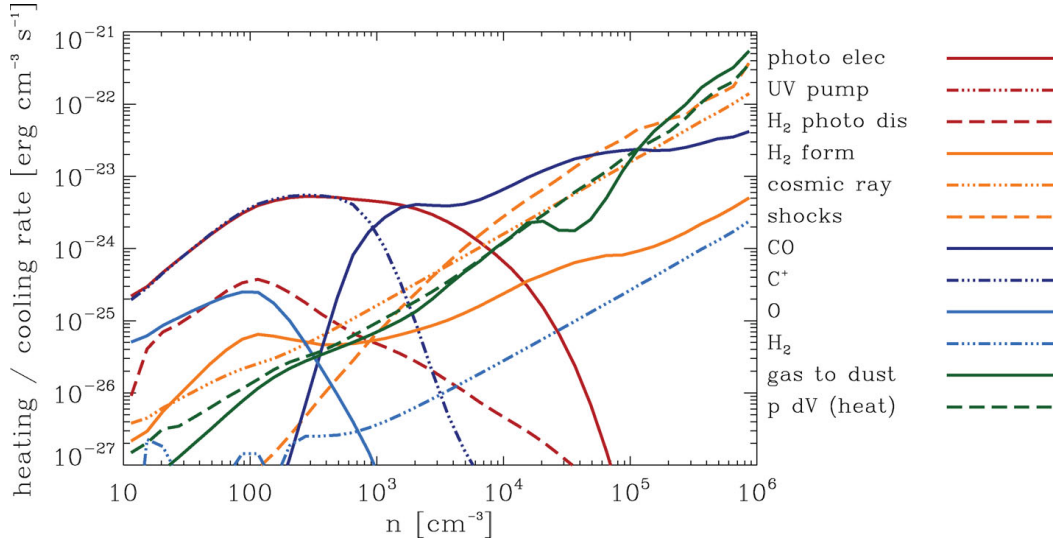
Figure 2.5: Heating and cooling rates of the most prominent heating and cooling effects in the ISM as function of number density. Taken from (Klessen & Glover, 2016)

temperatures and large molecular abundance are the requirements for star formation. The cold, dense molecular matter partly loses its magnetic support against gravity and hence becomes gravitationally unstable and collapses to form new stars. This is one side of the high contrast ISM and the only part that is capable of forming stars.

After the collapse of gas into a star, the material is locked inside the stars. By thermonuclear reactions the stars fuse up the material producing energy and heavier elements. Over time a fraction of those heavy elements is returned back to the ISM by strong stellar winds of high mass stars. At the end of high mass stellar life time there are immediate injections of heavy elements to the ISM by core collapse supernovae. These star loose part of their thermonuclear pressure support, resulting in a core collapses due to gravity. This strong ejection of material and energy into ISM not only drives turbulence but further enhances a highly heterogeneous structure and distribution of mass throughout the ISM, by forming regions of very high temperatures and low densities. Those regions are the other high contrast side of the ISM. The SN feedback is a self regulated process as the energy input influences the structure and distribution of mass, that itself effects new star formation.

The energy input by SNe is further capable of ejecting matter from the galaxy into the circum galactic medium (CGM) in terms of outflows (see Outflows below). This material either cools and falls back into the galaxy or enriches the CGM. Matter from the CGM can be accreted to the galaxy and enrich it from outside and thus form new star forming regions. These can also be formed after cooling of material ejected by SNe (Ferriere, 2001).

Outflows

Galactic outflows/winds are clumps and streams of matter moving at high velocities ($\sim$ 100 km s^{-1}) perpendicular to the galactic plane. They can carry up to $\sim$ 2-4 $M_\odot$ yr^{-1}, with

respect to the entire galaxy, and are characterized by the mass loading factor

$$\eta = \frac{\dot{M}_{\text{out}}}{\dot{M}_{\text{SFR}}} \tag{2.1}$$

where $\dot{M}_{\text{out}}$ is the mass carried outwards by outflows and $\dot{M}_{\text{SFR}}$ is the star formation rate. Moving at high velocities outflows need powerful energy sources, such as either feedback of SNe, CRs or active galactic nuclei (AGN). When stars explode they enrich their surrounding ISM with metals and their momentum drags gas of the ISM with it hence transporting a highly mixed gas outwards.

The transport outwards can be divided into two different categories: real outflows, if the material escapes the gravitational potential of the galaxy, and fountain flows, in which the material is not moving fast enough to escape the galactic potential and hence falls back onto the galaxy. In the case of the fountain flow, the high temperature gas cools down in the less dense regions and hence is capable of feeding star formation on its fallback. When the gas escapes the galaxy it enriches the circum galactic medium providing new fuel for other galaxies and stars in the CGM.

Cosmic rays play an important role in launching galactic winds and outflows. Why is explained in more detail in the next section.

2.1.5 Dynamics of the ISM

Highly dynamical process and interactions shape the ISM. There are multiple possible sources of which we explain the most relevant ones. For further reading we refer to Klessen & Glover (2016).

Turbulence

Turbulence plays a major role in the formation of dense regions, stability, amplifying magnetic field and transport of CRs. Small velocities lead to laminar and smooth flows but high velocities tend to lead to unstable and chaotic motion referred as turbulent motion. Turbulent motions lead to unpredictable local properties and hence turbulence is studied in a statistical way.

Basic turbulence is described by the Navier-Stokes-equation for an incompressible fluid, i.e. $\rho = \text{const}$

$$\frac{\partial \boldsymbol{v}(\boldsymbol{x},t)}{\partial t} + \boldsymbol{v}(\boldsymbol{x},t) \cdot \nabla \boldsymbol{v}(\boldsymbol{x},t) = -\frac{\nabla P(\boldsymbol{x},t)}{\rho(\boldsymbol{x},t)} + \nu \nabla^2 \boldsymbol{v}(\boldsymbol{x},t) + \boldsymbol{F}(\boldsymbol{x},t) \tag{2.2}$$

that describes the change of velocity over time (first term left side) accounting for advection of the flow (second term left side), acceleration by the pressure gradient (first term right side), dissipation of the flow by kinetic viscosity of the flow ν (second term right side) and further sources/fluxes contributing to the velocity change (third term right side).

The turbulent strength is measured by the Reynolds number that is the ratio of the advection over dissipation and can be estimated by

$$Re = \frac{v_l l}{\nu} \tag{2.3}$$

with the typical system length l and velocity scale v_l. For the ISM the Reynolds number is roughly $\sim 10^9$ so that the ISM is highly turbulent.

Incompressible turbulence is indicated by rotational modes that are referred as eddies. Turbulent energy cascades from large eddies down to smaller scales. This process is timely restricted by the turn over time of an eddy which is given by $t_l = l/v_l$. Once the energy is transferred down to small eddies, these then decay into random thermal motion, turbulence. Hence turbulence converts kinetic energy from large scales down to heating on small scales, the dissipation scale λ_ν.

Energy flows through the eddy, such that the specific energy flow is given by

$$\dot{e} = \frac{e_l}{t_l} = \frac{v_l^2}{2}\left(\frac{l}{v_l}\right)^{-1} = \frac{v_l^3}{l} \tag{2.4}$$

with specific kinetic energy e_l and turn over time t_l. The energy flow through an eddy is conserved and thus independent on scale. Energy is injected on scale L with v_L larger than the dissipation scale. As the energy flow is independent of scale it can be used to estimate the velocity on scale l by

$$v_l = (\dot{e}l)^{1/3} = v_L \left(\frac{l}{L}\right)^{1/3}. \tag{2.5}$$

With this energy is carried by large scale modes that are driven by external sources e.g. SNe. When reaching the dissipation scale the Reynolds numbers reaches unity which gives an estimation of the orders of magnitudes turbulence scales down

$$\frac{L}{\lambda_\nu} = Re^{3/4} \tag{2.6}$$

so the ISM turbulence with $Re \sim 10^9$ scales down six orders of magnitude.

Concerning the energy input that drives turbulence in the ISM, SNe seem to be a promising origin as studies show that they contribute most. With an average supernova rate of $\sigma_{SN} =$ 2-5 SN year^{-1} with an average energy release of $E_{SN} = 10^{51}$ erg consider a star forming region of cylindrical shape with radius of $R = 15$ kpc and a scale height of $H = 100$ pc the energy input rate is obtained by

$$\dot{e} = \frac{\sigma_{SN}\zeta_{SN}E_{SN}}{\pi R^2 H} = 3 \times 10^{-26}\,\frac{\text{erg}}{\text{s cm}^3} \times \left(\frac{\zeta_{SN}}{0.1}\right)\left(\frac{\sigma_{SN}}{(100\,\text{yr})^{-1}}\right)$$
$$\left(\frac{H}{100\,\text{pc}}\right)^{-1}\left(\frac{R}{15\,\text{kpc}}\right)^{-2}\left(\frac{E_{SN}}{10^{51}\,\text{erg}}\right) \tag{2.7}$$

which is the strongest one compared to other sources (Klessen & Glover, 2016) $\dot{e} \sim 10^{-27}$-10^{-30} erg cm^{-3} s^{-1}. Overall turbulence occupies an average energy density of $e \sim$ 5-10 eV cm^{-3} which is up to one order of magnitude larger than the energy density of the equipartition of CRs, magnetic fields and thermal gas.

Supernovae

A supernova is an explosion with which a star can end its life depending on it initial characteristics or by their surroundings. There are two types of supernovae (SNe). Type I are explosions of very old ($\sim 1\,\mathrm{Gyr}$) initially low mass stars. They have accreted mass from their surroundings and once their mass exceeds the Chandrasekhar limit, the star collapses due to insufficient pressure support. Thereby the star explodes and releases an energy of $\mathrm{E} \sim 10^{51}\,\mathrm{erg}$. The second type, type II SNe, are explosions of high mass stars $\mathrm{M} \geq 8\,\mathrm{M}_\odot$ by core collapse, as their cores are no longer able to support their outer shells. They eject a lot of mass into the ISM and releasing a comparable amount of energy as the type I SNe (Chevalier, 1977).

With their mass ejection at very high velocities SNe are believed to have one of the strongest, if not the strongest dynamical impact on the ISM. The velocities can reach up to several $10^4\,\mathrm{km\ s^{-1}}$ which creates a supersonic flow of matter. This flow usually expands spherically with respect to the star. The supersonic motion creates a shock layer at which the matter is swept up. The first expansion phase is at constant velocity and then paired up with an adiabatic expansion, know as Sedov-Taylor phase. As almost the entire gas gets ionized during the expansion there is no effective radiative cooling. This leads to an isothermal bubble of hot gas. During the Sedov-Taylor phase the expansion radius can be estimated by

$$R_{\mathrm{ST}}(t) = \left(\frac{\zeta_0 E_{\mathrm{SN}}}{\rho_0} \right)^{1/5} t^{2/5} \tag{2.8}$$

with energy of the SN E_{SN}, surrounding density ρ_0 and ζ_0 is an assumed constant factor that is inversely proportional to the averaged kinetic and thermal energies. The expansion velocity can be similarly expressed by

$$v_{\mathrm{ST}} = \frac{2}{5} \left(\frac{\zeta_0 E_{\mathrm{SN}}}{\rho_0} \right)^{1/5} t^{-3/5}. \tag{2.9}$$

The adiabatic expansion continues until the swept up material becomes comparable to the ejected mass by the star. This occurs when the radius of the expanding sphere reaches

$$R_S \sim \left(\frac{3 M_{\mathrm{SN}}}{4\pi\rho_0} \right)^{1/3} \tag{2.10}$$

with the ejected mass M_{SN} and density of the surrounding ISM ρ_0. Once the swept up mass exceeds the ejected mass of the SN, the expansion slows down and radiative cooling starts to set in, the snowplough phase begins. When the shock has slowed down enough the hot bubble and the surrounding ISM reach a state of pressure equilibrium and start merging and mixing together. With high energies freed in the explosions, SNe are able to accelerate particles up to relativistic speeds. Those particles are referred to as CRs, which are discussed in the next section.

2.2 Cosmic Rays

2.2.1 Observational constrains

The cosmic ray energy spectrum is shown in Figure 2.1 The magnetic fields within the solar wind, a steadily ejected stream of magnetized plasma, prevent low energetic charged particles from reaching the inner solar system. Hence at Earth we are constrained to observe only particles with an energy $> 300\,\mathrm{MeV}$. At higher energies the impact of the solar wind becomes negligible. Charged particles gyrate around the magnetic field lines with their Lamor radii

$$r_L = \frac{p_\perp c}{ZeB} \sim 2Z^{-1} \left(\frac{E}{10\,\mathrm{GeV}} \right) \left(\frac{B}{1\,\mu\mathrm{G}} \right)^{-1} \mathrm{AU} \tag{2.11}$$

with the particle's charge number Z and energy E and B is the magnetic field strength.
Particles with an energy above $3 \times 10^{18}\,\mathrm{eV}$ have a Lamor radius greater than the thickness of the galactic disk. Thus these high energetic CRs have to originate from outside the galaxy. This is supported by the elemental abundances and the slope of the spectrum.
The observed flux of CRs varies extremely with the energy. We observe 0.1 particles per $\mathrm{m^2\,s}$ per steradian at an energy of $10^{12}\,\mathrm{eV}$ per particle. In comparison to that we observe only 1 particles per $\mathrm{km^2}$, per century per steradian at an energy of $10^{20}\,\mathrm{eV}$. In the range of $\sim 100\,\mathrm{MeV}$ up to the knee at $\sim 4 \times 10^{15}\,\mathrm{eV}$ the spectrum follows a power law with index -2.7. Beyond the knee up to the ankle at $\sim 5 \times 10^{18}\,\mathrm{eV}$ it steepens to an index of -3.1. Exceeding these energies the slope flattens again to -2.7.
Comparing the integrated energies of the CR spectrum, it is essential to notice the largest fraction being occupied by particles, mostly protons, with an average energy around $1\,\mathrm{GeV}$ per particle. This justifies the assumption and modeling of only CR protons and no other CR species in this work because we are interested in their dynamical impact. Therefore we neglect the other parts of the spectrum and only consider CR protons. Whenever we refer to CR properties/quantities in this work we refer to the modeled CR protons.

2.2.2 Origin of cosmic rays

There are two different types of origins of CR, injection and acceleration. The injection is covered by three sources first one being the corona of low mass stars (Shapiro, 1999). Second the similarity in abundance of CRs and dust in the ISM suggest the injection of CRs by ionized dust particles (Meyer et al., 1997; Ramaty et al., 1997). Stellar winds of massive stars are the third option. They inject CRs in analogy to the solar wind. The selection effect is explained by more efficient injection of double ionized elements.
The acceleration of particles up to high energies was first discovered by Baade & Zwicky (1934). The standard theoretical approach describes the acceleration of CRs by diffusive shock acceleration (DSA) in SN shock waves. The shock sweeps up the powerful magnetized winds of the predecessor star until they run into the ISM. The theory of DSA of CRs is able to explain particle energies up to $3 \times 10^{18}\,\mathrm{eV}$. The knee can be explained due to the

decrease of acceleration efficiency once the Lamor radius matches the spatial extend of the shock. At even higher energies CRs are not isotropized and confined down stream, hence have a higher probability to escape from the ISM.

Due to the spatial constrain on acceleration there is a maximum energy CRs can reach which explains the transition towards heavier elements abundances in CRs at energies beyond the knee.

2.2.3 CR interactions and losses

Coulomb and hadronic losses

Both the Coulomb and hadronic losses strongly depend on the CR momentum. The hadronic interactions mainly effect high-momentum CRs whereas Coulomb interactions increase in the lower momentum regime.

The energy loss of a proton via Coulomb interactions in a plasma is calculated by Gould (1972)

$$-\left(\frac{\mathrm{d}E_p(p)}{\mathrm{d}t}\right)_{\text{Coul}} = \frac{4\pi e^4 n_e}{m_e \beta c}\left[\ln\left(\frac{2m_e c^2 \beta p}{\hbar \omega_{\text{pl}}}\right) - \frac{\beta^2}{2}\right] \tag{2.12}$$

with dimensionless momentum $p = P_p/(m_p c)$, kinetic energy of the proton $E_p(p) = \left(\sqrt{1+p^2}-1\right)m_p c^2$, plasma frequency $\omega_{\text{pl}} = \sqrt{4\pi e^2 n_e/m_e}$, number density of free electrons n_e and the dimensionless velocity $\beta = v_p/c$.

Inelastic reactions of CRs with atoms and molecules of the ISM lead to hadronic interactions. In those reactions both neutral and charged pions are produced if the energy of the CR exceeds $p_{\text{thr}} = 0.78\,\text{GeV}$. The neutral pions decay into γ-rays and the charged pions decay into secondary electrons and neutrinos:

$$\pi^{\pm} \rightarrow \mu^{\pm} + \nu_\mu/\bar{\nu}_\mu \rightarrow e^{\pm} + \nu_e/\bar{\nu}_e + \nu_\mu + \bar{\nu}_\mu \tag{2.13}$$

$$\pi^0 \rightarrow 2\gamma. \tag{2.14}$$

The energy loss of a CR proton can be expressed by

$$-\left(\frac{\mathrm{d}E_p(p)}{\mathrm{d}t}\right)_{\text{hadr}} = n_{\text{N}}\sigma_{\text{pp}}K_{\text{p}}m_p c^3(\gamma-1)\theta(p-p_{\text{thr}}) \tag{2.15}$$

with the total pion cross-section $\sigma_{\text{pp}} = 44.2\,\text{mbarn}$ (Pfrommer & Ensslin, 2004), inelasticity of the hadronic interaction $K_{\text{p}} \approx 0.5$ (Mannheim & Schlickeiser, 1994), the target nucleon density in the intra cluster medium at primordial element composition, i.e. $X_{\text{He}} = 0.24$, $n_{\text{N}} = n_e/(1-X_{\text{He}})$ and the kinematic momentum threshold for the hadronic interaction p_{thr} within the Heavyside function θ, which is 1 for positive arguments and 0 for negative.

Inverse Compton losses

Charged particles moving at relativistic speed can experience Compton scattering with photons or the magnetic field by means of virtual photons. When the photon transmits

a part of its energy to the particle, this process is identified as Compton scattering. If the photon gains energy in the interaction, the interaction is classified as inverse Compton scattering. Thereby the particle looses energy which is described as friction force acting in the opposite momentum direction.

Cosmic ray cooling properties

The combined CR energy losses are also referred to as CR cooling. When modeling both thermal gas and CRs it is important to note the different cooling timescales. Enßlin et al. (2007) and Jubelgas et al. (2008) have shown that CR maintain their energy on larger timescales, considering Coulomb and hadronic cooling, compared to radiative cooling of thermal gas, see Figure 2.6. The left panel shows the cooling timescales of Coulomb and hadronic losses as function of a CR proton low momentum cutoff $q = m_\mathrm{p} v_{Tp} \gamma_\mathrm{p}$, with particle velocity v_{Tp} and relativistic Lorentz factor γ, for a gas with density 2.386×10^{-25} g cm^{-3}. The Coulomb cooling is shown by the rising solid line, the hadronic cooling by the almost horizontal solid line and the combined cooling timescale is indicated by the rising dashed-dotted line. In the right panel the radiative cooling timescale, for a gas of the same density, is plotted as solid line. The dashed line marks the CR cooling timescale for a high momentum CRs ($q \gg 1$). When comparing both cooling time scales it is becomes evident that CRs possess their energy on larger time scales than thermal gas within a temperature range of 10^4-10^8 K. This becomes important for the dynamical impact of CRs and their energies on the gas dynamics.

Acceleration, Diffusive shock acceleration

The shape of the observed CR spectrum follows a power law (non thermal property) which is explained best by an acceleration at shock waves/fronts. This process is explained by the diffusive shock acceleration mechanism that is build on Fermi's first ideas. Collisionless shock waves are able to accelerate ions from the high energy tail of the Maxwellian distribution. In this process ions are reflected from magnetic irregularities through magnetic resonances between their gyro motion and wave irregularities in the magnetized plasma. The induced back and forth crossing of the shock front results in an net energy gain of the particles.

Second order Fermi process

Charged particles gyrate around the magnetic field lines. They scatter of the magnetic irregularities and plasma waves, also referred to as Alfvén waves. Their movement is described by a random walk with pitch angle θ enclosed by the new direction and the magnetic field orientation. Scattering of moving targets leads to a systematic energy gain through momentum change. In momentum space second order Fermi process is described by a diffusion process.
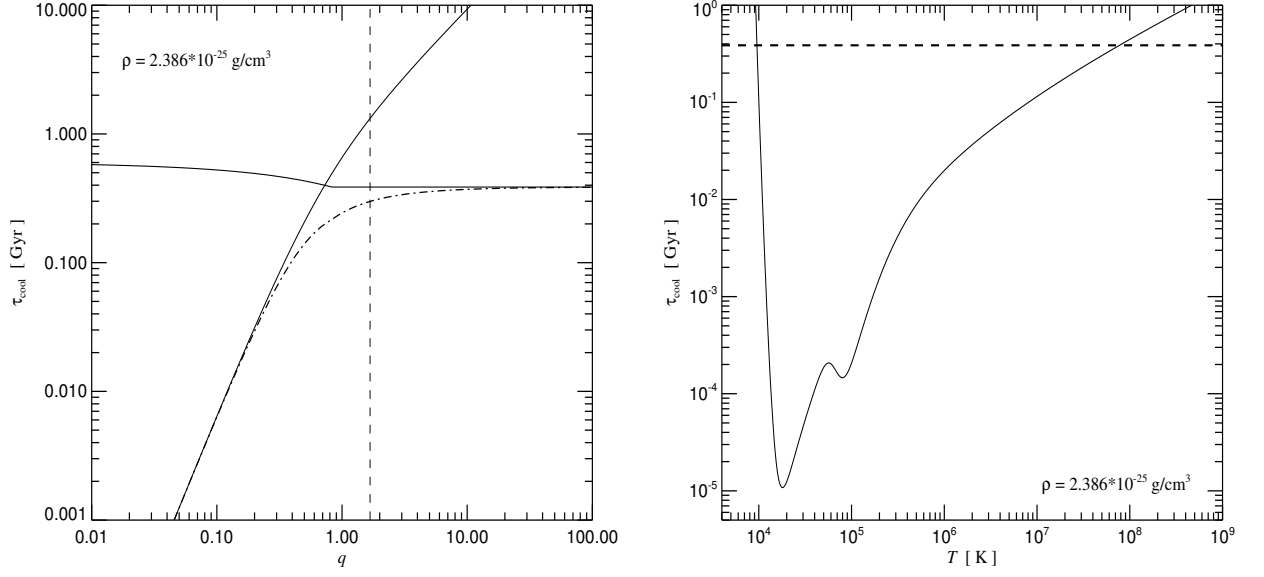
Figure 2.6: (left): Cooling time of Cosmic Rays as a function of the spectral cutoff q (low momentum by Jubelgas). The solid rising line represents the cooling time of CRs via coulomb interactions and the solid almost horizontal line the cooling time via hadronic losses. The resulting effective cooling time is given by the dashed dotted line saturating to the horizontal line. (right): Cooling time of thermal gas as function of the gas temperature due to radiative cooling. Figures taken from (Jubelgas et al., 2008)

2.2.4 CR transport

Fluid treatment

Similar to the fluid dynamics of thermal gas, CRs are treated not as individual particles but as a fluid. For fluids there is a statistical description of the particles, given by Boltzmann's equation

$$\frac{\partial f}{\partial t} + \frac{\mathrm{d}\boldsymbol{x}}{\mathrm{d}t} \cdot \frac{\partial f}{\partial \boldsymbol{x}} + \frac{\mathrm{d}\boldsymbol{p}}{\mathrm{d}t} \cdot \frac{\partial f}{\partial \boldsymbol{p}} = 0, \tag{2.16}$$

with the particle number distribution function $f = f(\boldsymbol{x}, \boldsymbol{p})$ in phase space $(\boldsymbol{x}, \boldsymbol{p})$. Inserting the equation of motion of a charged particle, given by the classic Lorentz force $\mathrm{d}\boldsymbol{p}/\mathrm{d}t = q(\boldsymbol{v} \times \boldsymbol{B}/c)$, this leads to the Vlasov-equation

$$\frac{\partial f}{\partial t} + \frac{\mathrm{d}\boldsymbol{x}}{\mathrm{d}t} \cdot \frac{\partial f}{\partial \boldsymbol{x}} + q\left(\frac{\boldsymbol{v}}{c} \times \boldsymbol{B}\right) \cdot \frac{\partial f}{\partial \boldsymbol{p}} = \left.\frac{\partial f}{\partial t}\right|_{\mathrm{scatt}}. \tag{2.17}$$

Here $\left.\frac{\partial f}{\partial t}\right|_{\mathrm{scatt}}$ denotes the contributions of small scale fields. The assumption of small field perturbations yields that the timescales on which they effect the dynamics, are larger than the gyration timescales of CRs. Hence the Vlasov-equation can be averaged over a CR gyro-orbit, which results in the focused transport equation derived by Skilling (1975);

Isenberg (1997); Zank et al. (2000).

By applying a moment method, e.g. (Zank, 2014), to the focused transport equation, the CR energy density can be derived

$$\epsilon_{\mathrm{cr}} = \int \mathrm{d}^3 p\, T(p) f(p, \mu) = \int_0^\infty \mathrm{d}p\, 4\pi p^2 T(p) f_0(p), \tag{2.18}$$

with the relativistic kinetic energy $T(p) = \sqrt{p^2 c^2 + (mc^2)^2} - mc^2$, the CR particle distribution function f and its monopole moment f_0, and the related pitch angle $\mu = \boldsymbol{v} \cdot \boldsymbol{b}/v$ with velocity $\boldsymbol{v}$ and normalized magnetic field vector $\boldsymbol{b}$ and momentum p. The pressure is closely related and defined as

$$P_{\mathrm{cr}} = \int \mathrm{d}^3 p\, \frac{pv}{3} f(p, \mu) = \int_0^\infty \mathrm{d}p\, \frac{4\pi}{3} p^2 pv f_0(p). \tag{2.19}$$

Both energy and pressure are related by the equation of state given by

$$P_{\mathrm{cr}} = (\gamma_{\mathrm{cr}} - 1)\epsilon_{\mathrm{cr}}, \tag{2.20}$$

with $\gamma_{\mathrm{cr}} = 4/3$ in the ultra-relativistic limit. Those are the expression for the isotropic transport. Similarly the equations for the anisotropic transport are given by

$$f_{\mathrm{cr}} = \int_0^\infty \mathrm{d}p\, 4\pi p^2 T(p) v f_1(p), \tag{2.21}$$

$$K_{\mathrm{cr}} = \int_0^\infty \mathrm{d}p\, 4\pi p^2 \frac{pv}{3} v f_1(p). \tag{2.22}$$

with first moment f_1, the CR flux f_{cr} and CR pressure flux K_{cr} along the magnetic field lines. They describe the CR energy and pressure flux along the magnetic field lines. They are linked by the same equation of state as CR pressure and energy density

$$K_{\mathrm{cr}} = (\gamma_{\mathrm{cr}} - 1)f_{\mathrm{cr}}. \tag{2.23}$$

Those are used to evaluate the general CR transport equation and particle distribution function and lead to

$$\frac{\partial \epsilon_{\mathrm{cr}}}{\partial t} + \boldsymbol{\nabla} \cdot (\boldsymbol{u}(\epsilon_{\mathrm{cr}} + P_{\mathrm{cr}}) + \boldsymbol{b} f_{\mathrm{cr}}) = \boldsymbol{u} \cdot \boldsymbol{\nabla} P_{\mathrm{cr}} + \left. \frac{\partial \epsilon_{\mathrm{cr}}}{\partial t} \right|_{\mathrm{scatt}}, \tag{2.24}$$

$$\frac{\partial f_{\mathrm{cr}}}{\partial t} + \boldsymbol{\nabla} \cdot (\boldsymbol{u} f_{\mathrm{cr}}) + \frac{c^2}{3} \boldsymbol{b} \cdot \boldsymbol{\nabla} \epsilon_{\mathrm{cr}} = -(\boldsymbol{b} \cdot \boldsymbol{\nabla} \boldsymbol{u}) \cdot (\boldsymbol{b} f_{\mathrm{cr}}) + \left. \frac{\partial f_{\mathrm{cr}}}{\partial t} \right|_{\mathrm{scatt}}, \tag{2.25}$$

in the ultra-relativistic limit $v = c$. Here, $\boldsymbol{u}$ is the non-relativistic velocity of a comoving reference frame, in which the particle's momentum and velocity are measured. Equation (2.24) describes the CR energy as a conserved quantity, which is advected with the gas. Therefore CRs gain or loose energy when ever the gas is compressed or expands. In equation (2.25) the first term on the right hand side accounts for the changes in the flux due to spatial changes in the MHD environment. The third term on the left hand side describes the transport mechanism of CR.

Advection

Magnetic field lines are frozen within the thermal plasma and are dragged with local gas flows, in the ideal MHD approximation. As CRs are coupled to the magnetic field by their gyration with their Lamor radii, they are also closely linked to the local gas. Hence bulk movements of the local gas drag the CRs with them, i.e. advecting them with the bulk velocity of the local gas. Therefore CRs which are advected with the gas flow also experience energy losses or gains from adiabatic expansion or compression of the flow.

Diffusion

Diffusion is a an energy conserving scattering process. It can be divided into an- and isotropic diffusion. The anisotropic diffusion constrains the particle movement to a certain direction or plane and in the isotropic diffusion particles are allowed to propagate equally in any direction. The basic diffusion equation is given by Fick's second law

$$\frac{\partial n}{\partial t} = \boldsymbol{\nabla} D_{xx} \cdot \boldsymbol{\nabla} n \qquad (2.26)$$

with particle number density n and spatial diffusion tensor D. For CRs, the anisotropic diffusion constrains their propagation parallel to the magnetic field lines. The anisotropic coefficient in the diffusion tensor D_{xx} is given by $D_{xx} = \langle v \rangle \lambda_{mfp}/3$. For a CR particle with an average energy of $E \sim 10\,\mathrm{GeV}$ per particle this yields $D_{xx} \approx 3 \times 10^{28}\,\mathrm{cm^2\,s^{-1}}$ (Zweibel, 2013).

The CR diffusion process can be explained on a microscopic scale as a result of particle scattering of magnetohydrodynamical waves and discontinuities due to local perturbations. CRs might advance a few gyro-radii along the field lines before they scatter off of local plasma waves of the medium. This results in a random walk along the field lines which results in a diffusion processes parallel to the magnetic field.

CR particles and waves interact resonantly and hence CRs are mainly scattered by irregularities of the magnetic field with their wave vectors projected onto the average magnetic field direction being equal to

$$k_{11} = \pm \frac{s}{r_L \mu} \qquad (2.27)$$

with Lamor radius (2.11), pitch angle μ and cyclotron resonance orders s. The efficiency of the scattering process is dependent on the polarization of the wave vectors. This total process results in a spatially highly anisotropic diffusion of CRs along the magnetic field lines. Stronger fluctuations of the magnetic field on small scales $\sim 100\,\mathrm{pc}$ can lead to a globally more isotropic diffusion process of CRs. Both the an- and isotropic diffusion used in AREPO (section 2.4) are described by Pakmor et al. (2016).

Streaming

Considering the second order of CR interactions with magnetic irregularities brings up inelastic scattering terms that allow momentum exchange from the CRs to the irregularities. These interactions depend on the presents of the streaming instability (Kulsrud &

Pearce, 1969). When CRs move along the magnetic field within the ambient medium at bulk drift speed v_D with $v_D > v_A$, the local Alfvén velocity, they excite magnetohydro-dynamic (MHD) Alfvén waves. When CR transport is determined by scattering off of self-generated Alfvén waves this is referred to as the self-confinement picture. Hence CRs can further loose part of their energy by those interactions leading to a streaming behavior (CR streaming) (Skilling, 1975; Thomas & Pfrommer, 2019).

2.2.5 Impact of CRs on galactic dynamics

The effects of CRs have been studied in various fields. They have an impact on the ISM, local clouds and entire galaxies. CRs are capable of driving steady flows of matter by their pressure gradient and heating mechanisms. Thus they play a role in evolution of galaxies and the inter-galactic medium. Studies have shown thermal gas pressure alone is not sufficient to drive outflows. However including CRs in equipartition with thermal gas certainly does drive outflows $\sim 2 M_\odot \, \mathrm{yr}^{-1}$ with respect to the entire galaxy. CRs could drive even larger amounts as the star formation rate (SFR) is tied to the SN rate and hence CRs acceleration. Nevertheless this seems to be self limited as too large CR pressures drive out large fractions of the ISM matter and thus reduces the SFR.

Further CR heating is an important process as Enßlin et al. (2007); Jubelgas et al. (2008) have shown that CR cool less efficient than thermal gas, see Figure 2.6. Being in energy equipartition with thermal gas and the magnetic field leads to a similar dynamical impact. CRs increase the gaseous scale height of the galaxy by providing further pressure support against gravity. Studies have shown that CRs do highly impact the intrinsic dynamics as they are capable of quenching star formation (Pfrommer et al., 2016). CR are able to quench star formation, drive outflows and winds. This is crucial for galaxy and star formation as the gas is able to hold on to its energy for longer times. Therefore the gas maintains a higher temperature, thus reducing or negating the collapse of gaseous clouds and therefore reducing or preventing star formation. A reduced star formation leads to less SNe and hence CR do have a large impact on the dynamics of the system. Girichidis et al. (2016a) have compared the impact of CRs on the internal structure of galaxies. They find that CRs do play a non negligible role in forming the structures observed in galaxies, i.e. creating large low density regions in the galaxy disk.

2.3 Numerical Methods

We perform our simulations with the unstructured moving mesh code AREPO (Springel, 2010) (see section 2.4). We solve idealized magnetohydrodynamic (MHD) equations using the Harten-Lax-van Leer-Discontinuities (HLLD) Riemann solver (Miyoshi & Kusano, 2005). The combined system of equation that we solve can be written in following form

$$\frac{\partial \boldsymbol{U}}{\partial t} + \boldsymbol{\nabla} \cdot \boldsymbol{F} = \boldsymbol{S}, \tag{2.28}$$

where $\boldsymbol{U}$ is the quantity vector, $\boldsymbol{F}$ the flux and exchange terms and $\boldsymbol{S}$ represents the source terms. They are given by

$$\boldsymbol{U} = \begin{pmatrix} \rho \\ \rho\boldsymbol{v} \\ e \\ e_{\text{cr}} \\ \boldsymbol{B} \end{pmatrix}, \ \boldsymbol{F} = \begin{pmatrix} \rho\boldsymbol{v} \\ \rho\boldsymbol{v}\boldsymbol{v}^{\text{T}} + P\boldsymbol{1} - \boldsymbol{B}\boldsymbol{B}^{\text{T}}/(4\pi) \\ (e + P)\boldsymbol{v} - \boldsymbol{B}(\boldsymbol{v} \cdot \boldsymbol{B})/(4\pi) \\ e_{\text{cr}}\boldsymbol{v} - \kappa_e\boldsymbol{b}(\boldsymbol{b} \cdot \boldsymbol{\nabla}e_{\text{cr}}) \\ \boldsymbol{B}\boldsymbol{v}^{\text{T}} - \boldsymbol{v}\boldsymbol{B}^{\text{T}} \end{pmatrix}, \ \boldsymbol{S} = \begin{pmatrix} 0 \\ \boldsymbol{0} \\ P_{\text{cr}}\boldsymbol{\nabla} \cdot \boldsymbol{v} + \Lambda_{\text{th}} + \Gamma_{\text{th}} \\ -P_{\text{cr}}\boldsymbol{\nabla} \cdot \boldsymbol{v} + \Lambda_{\text{cr}} + \Gamma_{\text{cr}} \\ \boldsymbol{0} \end{pmatrix}. \tag{2.29}$$

Here, ρ is the mass density, $\boldsymbol{v}$ the three dimensional velocity vector, $\boldsymbol{B}$ the three dimensional magnetic field and $\boldsymbol{1}$ the three dimensional unity matrix. The total energy density

$$e = \frac{\rho\boldsymbol{v}^2}{2} + e_{\text{th}} + e_{\text{cr}} + \frac{\boldsymbol{B}^2}{8\pi} \tag{2.30}$$

involves kinetic, thermal, CR and magnetic energy contributions. The CR energy density is computed separated from the total energy density. The total pressure consists of thermal, CR and magnetic pressure described by

$$P = P_{\text{th}} + P_{\text{cr}} + P_{\text{mag}} \tag{2.31}$$

$$= (\gamma_{\text{th}} - 1)e_{\text{th}} + (\gamma_{\text{cr}} - 1)e_{\text{cr}} + \frac{\boldsymbol{B}^2}{8\pi}. \tag{2.32}$$

The described set of equations contains both a fluid treatment of CRs and thermal gas. This leads to a combined equation of state with effective adiabatic index

$$\gamma_{\text{eff}} = \frac{\gamma_{\text{th}}P_{\text{th}} + \gamma_{\text{cr}}P_{\text{cr}}}{P_{\text{th}} + P_{\text{cr}}} \tag{2.33}$$

with $\gamma_{\text{th}} = 5/3$ and $\gamma_{\text{cr}} = 4/3$ for thermal gas and CRs, respectively. In the diffusion tensor, κ_e, we set a value of 0 perpendicular and vary the value parallel to the magnetic field lines in multiple simulations. We assume values of $10^{28}\,\text{cm}^2\,\text{s}^{-1}$, $3 \times 10^{28}\,\text{cm}^2\,\text{s}^{-1}$ and $10^{29}\,\text{cm}^2\,\text{s}^{-1}$, which are closely related to observed values (Zweibel, 2013). $\Gamma_{\text{th, cr}}$ and $\Lambda_{\text{th, cr}}$ are explicit source and loss terms to the thermal and CR energy densities.

2.3.1 Shocks & Riemann problem

Shocks

Hydrodynamical flows can develop waves traveling faster than the local sound speed. If those waves hit slower moving gas they create a discontinuous change of several quantities (density, velocity etc.). Shocks can be produces by any supersonic compressible disturbance resulting from e. g. SNe, supersonic gas accretion or merging events. Shocks can be divided into collisional and collisionless ones. They are classified as collisionless if the mean free path of a particle within the shock, is smaller than the corresponding coulomb interaction radius $\lambda_{\text{mfp}} < \lambda_{\text{coulomb}}$ what prevents particles from interacting. With the conservation laws of mass, momentum and energy the well known Rankine-Hugoniot jump conditions can be derived for a plane parallel shock in the shock rest frame:

$$\rho_2 v_2 - \rho_1 v_1 = 0 \tag{2.34}$$

$$\rho_2 v_2^2 + P_2 - (\rho_1 v_1 + P_1) = 0 \tag{2.35}$$

$$\frac{1}{2} v_2^2 + e_{2,\text{th}} + \frac{P_2}{\rho_2} - (\frac{1}{2} v_1^2 + e_{2,\text{th}}) = 0 \tag{2.36}$$

with the up- and downstream regimes indicated by subscript 1, 2 respectively, density ρ, velocity v, pressure P and specific thermal energy e_{th}.

The jump conditions lead to a characterization of the shock. For tangential shocks the solution of the first condition (2.34) is given by the trivial case $v_1 = v_2 = 0$ which implies $P_1 = P_2$. Therefore there is no mass flux through tangential discontinuities due to the constant velocity component in the shock's rest frame. At the tangential discontinuities arbitrary jumps of density are allowed but need to be compensated by the same jump in temperature in the other direction. The other type of solution with $\rho_1 v_1 \neq 0$ inherits a mass flux though the discontinuity which is labeled as a shock.

Shocks can be characterized by their strength that is measured by the shocks Machnumber. The Machnumber is calculated via

$$\mathcal{M}_1 = \frac{v_1}{c_{s,1}} = \sqrt{\frac{m v_1^2}{\gamma k_B T_1}} \tag{2.37}$$

Riemann problem

The Riemann problem is an initial value problem of two piece-wise constant states that share a common boundary at time 0. There are left and right states each consisting of a set of primitive variables like density, pressure and velocity, e.g. see Figure 2.7 left panel with initial pressure set on a higher value on the left-hand side and lower value on the right-hand side. The states are separated in the middle (vertical red line). The time evolution of the state can be solved analytically for an ideal gas (Toro & Billett, 1997). The state evolves with time as shown in the right panel side of Figure 2.7 where three different waves can be identified a shock wave, contact discontinuity and a refraction wave. The shock wave
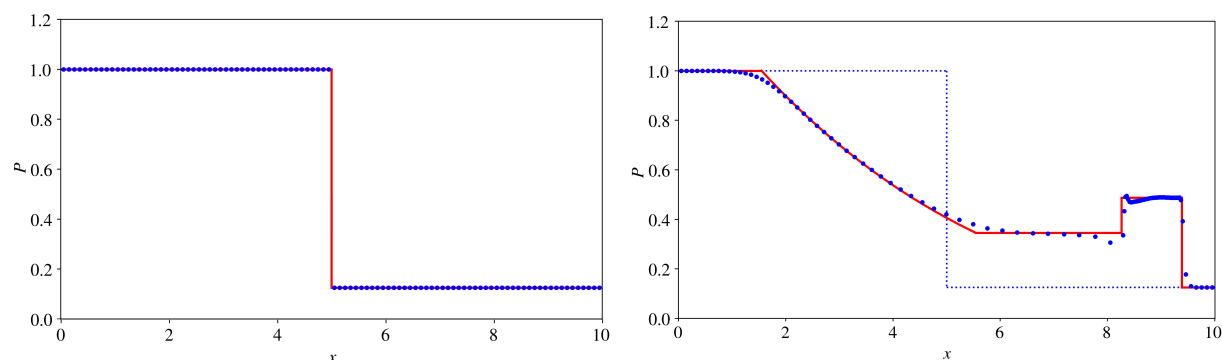
Figure 2.7: Riemann problem showing the evolution of one primitive variable (pressure). The left panel shows the initial state. The right panel shows a time stamp after the evolution of initial state, blue dots represent the simulation data points and the red line gives the analytic solution to the given problem. Take from (Pfrommer et al., 2016)

or just the shock is advancing in space at speed larger than the local sound speed towards the right-hand side with low pressure and compresses the fluid. At the shock front there is a discontinuous change in the quantities indicated by the sudden vertical jump and the large vertical red line at the right. Across the shock the properties are constant and at the contact discontinuity which is the original border between both states advancing the value drops slightly. The connection of the initial left state and the advancing shock is hold by the refraction wave. This is the information for the system that the material is now flowing form left to right.

2.3.2 Finite volume scheme

Consider the following set of equations

$$\partial_t \boldsymbol{U} + \boldsymbol{\nabla} \cdot \boldsymbol{F} = 0 \tag{2.38}$$

with $\partial_t = \partial/\partial t$, current state vector $\boldsymbol{U}$ and flux vector $\boldsymbol{F}$. Solving this in a continuous manner is impossible and hence it is broadly solved in a discretized way. Therefore the volume is subdived into a set of disjoint cells that fill the entire volume.

The state vector $\boldsymbol{U}$ is then not expressed as a function but as spatial averages over regions at a certain time t_n. We note the time step as subscript for the time and as superscript for all other variables. The spatial average is taken over the interval (1D) $\left[x_{i-\frac{1}{2}}, x_{i+\frac{1}{2}}\right]$ of length $\Delta x_i = x_{i+\frac{1}{2}} - x_{i-\frac{1}{2}}$. The interval represents the computational cell centered at $x_i = (x_{i-\frac{1}{2}} + x_{i+\frac{1}{2}})/2$ or short the i-th cell. At time t_n the averaged state vector of cell i is given by

$$\boldsymbol{U}_i^n = \frac{1}{\Delta x_i} \int_{x_{i-\frac{1}{2}}}^{x_{i+\frac{1}{2}}} \boldsymbol{U}(x, t_n) \mathrm{d}x. \tag{2.39}$$
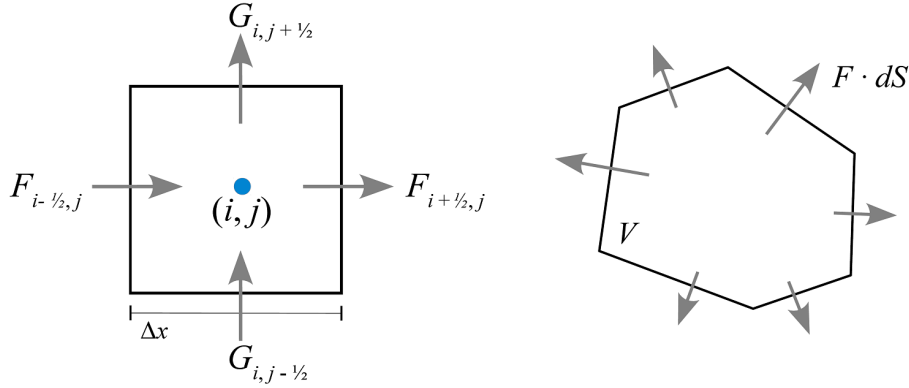
Figure 2.8: Illustration of a multidimensional flux flow through a cartesian cell/grid (left) and an unstructured grid (right). Taken from (Springel et al., 2019)

When solving (2.38) by integrating both sides over $\left[x_{i-\frac{1}{2}}, x_{i+\frac{1}{2}}\right]$ and $[t_n, t_{n+1}]$ this leads to

$$\boldsymbol{U}_i^{n+1} = \boldsymbol{U}_i^n - \Delta t \cdot \frac{\boldsymbol{F}_{i+\frac{1}{2}} - \boldsymbol{F}_{i-\frac{1}{2}}}{\Delta x_i}. \tag{2.40}$$

The term $\boldsymbol{F}_{i-\frac{1}{2}}$ gives the flux flowing from left into the cell and $\boldsymbol{F}_{i+\frac{1}{2}}$ respectively the flux out of the cell into the next one. The flux vectors are given by the time independent solution of a Riemann problem $\boldsymbol{F}_{i+\frac{1}{2}} = \boldsymbol{F}_{\text{Riemann}}\left(\boldsymbol{U}_i^n, \boldsymbol{U}_i^{n+1}\right)$ that further gives the factor Δt.

Using the Riemann problem to update the state vector goes back to Godunov and hence are referred to as Godunov schemes. The problem behind this scheme is it assumes all independent Riemann problems that describe an infinite two side problem. The independence of each problem then constrains the usable time steps. The time steps are constrained by the CFL-time step criterion that ensures the approximated independence of each problem with $\Delta t \leq \Delta x / c_{\text{max}}$ and maximum sound speed c_{max}. This scheme is for the one dimensional case and of first order of accuracy, thus can be extended into multiple dimensions and higher accuracy.

In three dimensions equation (2.38) is then described by the individual fluxes in x-, y- and z-direction ($\boldsymbol{F}(\boldsymbol{U})$, $\boldsymbol{G}(\boldsymbol{U})$, $\boldsymbol{H}(\boldsymbol{U})$) resulting in

$$\partial_t \boldsymbol{U} + \partial_x \boldsymbol{F} + \partial_y \boldsymbol{G} + \partial_z \boldsymbol{H}. \tag{2.41}$$

This equation can be easily solved for with an unsplit scheme that simultaneously applies all fluxes in x-, y- and z-direction. An advantage of the unsplit scheme is it can be applied for any kind of cell either regular or irregular (see Figure 2.8). In the unsplit scheme the update of the state vector is calculated via

$$\boldsymbol{U}^{n+1} = \boldsymbol{U}^n - \frac{\Delta t}{V} \int_{\partial V} \boldsymbol{F} \cdot \mathrm{d}\boldsymbol{S} \tag{2.42}$$

in which the integration is over the entire cell surface and $\mathrm{d}\boldsymbol{S}$ are the individual outwards pointing face area vectors.

In order to reach higher accuracy the quantities of the state vector $\boldsymbol{U}$ have to be linearly reconstructed instead of being set constant. The second order Godunov scheme estimates the gradients by linear difference of the quantities for each cell and thus limits the slope.

$$\partial_x \boldsymbol{U}_i = \mathrm{minmod}\left(\frac{\boldsymbol{U}_i - \boldsymbol{U}_{i-1}}{x_i - x_{i-1}}, \frac{\boldsymbol{U}_{i+1} - \boldsymbol{U}_i}{x_{i+1} - x_i}\right) \tag{2.43}$$

with the minmod-function given by

$$\mathrm{minmod}(a, b) = \frac{\mathrm{sign}(a) + \mathrm{sign}(b)}{2}\min(|a|, |b|) \tag{2.44}$$

Therefore the fluxes in the previous scheme (2.40) are calculated differently by using the linear reconstruction within $\boldsymbol{U}$, in expression

$$\boldsymbol{U}^L_{i+\frac{1}{2}} = \boldsymbol{U}_i + (\partial_x \boldsymbol{U}_i)\frac{\Delta x}{2} \tag{2.45}$$

$$\boldsymbol{U}^R_{i+\frac{1}{2}} = \boldsymbol{U}_{i+1} - (\partial_x \boldsymbol{U}_{i+1})\frac{\Delta x}{2} \tag{2.46}$$

and the Riemann problem is then solved for $\boldsymbol{F}_{\mathrm{Riemann}}(\boldsymbol{U}^L_{i+\frac{1}{2}}, \boldsymbol{U}^R_{i+\frac{1}{2}})$. To make this even more accurate and stable the gradient estimation should be extended by a prediction of the time evolution as it is part of the total change of state. This leads to the following set of equations

$$\boldsymbol{U}^L_{i+\frac{1}{2}} = \boldsymbol{U}_i + (\partial_x \boldsymbol{U}_i)\frac{\Delta x}{2} + (\partial_t \rho_i)\frac{\Delta t}{2} \tag{2.47}$$

$$\boldsymbol{U}^R_{i+\frac{1}{2}} = \boldsymbol{U}_{i+1} - (\partial_x \boldsymbol{U}_{i+1})\frac{\Delta x}{2} + (\partial_t \rho_{i+1})\frac{\Delta t}{2} \tag{2.48}$$

With $\partial_x \boldsymbol{U}_i$ we got a slope limited estimation of the gradient in cell i and have to include a comparable expression for the time derivation. This can be done by rewriting (2.38)

$$\partial_t \boldsymbol{U} = -\partial_x \boldsymbol{F} = -\frac{\partial \boldsymbol{F}}{\partial \boldsymbol{U}} \cdot \partial_x \boldsymbol{U} = -\boldsymbol{A}(\boldsymbol{U}) \cdot \partial_x \boldsymbol{U} \tag{2.49}$$

with $\boldsymbol{A}(\boldsymbol{U})$ being the Jacobian matrix. Thus this finally leads to the set of equations

$$\boldsymbol{U}^L_{i+\frac{1}{2}} = \boldsymbol{U}_i + \left[\frac{\Delta x}{2}\boldsymbol{1} - \frac{\Delta t}{2}\boldsymbol{A}(\boldsymbol{U}_i)\right] \cdot (\partial_x \boldsymbol{U}_i) \tag{2.50}$$

$$\boldsymbol{U}^R_{i+\frac{1}{2}} = \boldsymbol{U}_{i+1} - \left[\frac{\Delta x}{2}\boldsymbol{1} + \frac{\Delta t}{2}\boldsymbol{A}(\boldsymbol{U}_{i+1})\right] \cdot (\partial_x \boldsymbol{U}_{i+1}) \tag{2.51}$$

which are know as MUSCL Hancock scheme as extension of a second order Godunov scheme. There are further extensions and higher orders of accuracy but the MUSCL-Hancock scheme is used slightly adapted (Springel, 2010) in AREPO.

2.4 AREPO

AREPO (Springel, 2010) is a Lagrangian code which allows to move cells with flow. The principle is shown in Figure 2.9. Individual cells marked by red dots are moved with their velocity indicated by the arrows within the initial mesh. The mesh adopts according to the cell movements. The cell interactions are calculated in the reference frame of the shared boundary between two cells. As the cells are moving with the dynamical flow of the system only the relative velocity between each cells needs to be accounted for in the flux calculation. This is a great advantage as it reduces the error of the velocity component significantly. Therefore, AREPO provides a numerical advantage compared to fixed meshes in which the total flux of gas needs to be treated as flux through each cell.

2.4.1 Spatial discretization

We know how to calculate the conserved and primitive quantities of particles/cells once we got the discretization. This discretization is achieved by constructing a particle mesh. The particle mesh used in AREPO is based on a voronoi tessellation. A voronoi tessellation splits up the area (2D) or volume (3D) into non overlapping cells, with each cells containing exactly one mesh generating point. Each cell further contains all points that are closest to that point of generation and boundaries of neighboring cells are thus equally distant from both cell generating points, see Figure 2.10.

Geometrically this seems counter intuitive as it requires more complicated cell interaction calculations due to the non uniform shape. However it provides crucial properties that allow a reduced error in the calculation. One of these properties is that the mesh is galilean invariant which allows the calculation frame to be moved along the mesh. This reduces the resulting velocity to the relative velocity between individual cells and hence provides a smaller source of errors. With moving mesh generating points the voronoi mesh is generated in each time step anew.

2.4.2 Refinement & derefinement

In order increase and decrease the resolution in highly dynamically active and low active regions AREPO uses a refinement and derefinement criteria, i. e. it adaptively increases or decreases the number of cells in a given volume of the box. The are multiple criteria which allow the cells to be split up or merge. For both the cell to be refined or derefined it has to fulfill certain criteria. For the refinement the shape of the individual cell is checked. If the cell is not in a spherical shape it will not be refined. Therefore an angle α is calculated for each surface boundary:

$$\alpha = \sqrt{\frac{A_{\text{face}}}{\pi}} \cdot h^{-1} \tag{2.52}$$

where A_{face} corresponds to the boundary surface area, and h is the distance of the surface from the mesh generating point. Only if the maximum angle of a cell is smaller than a selected maximum value the cell can be refined if other refinement criteria match.
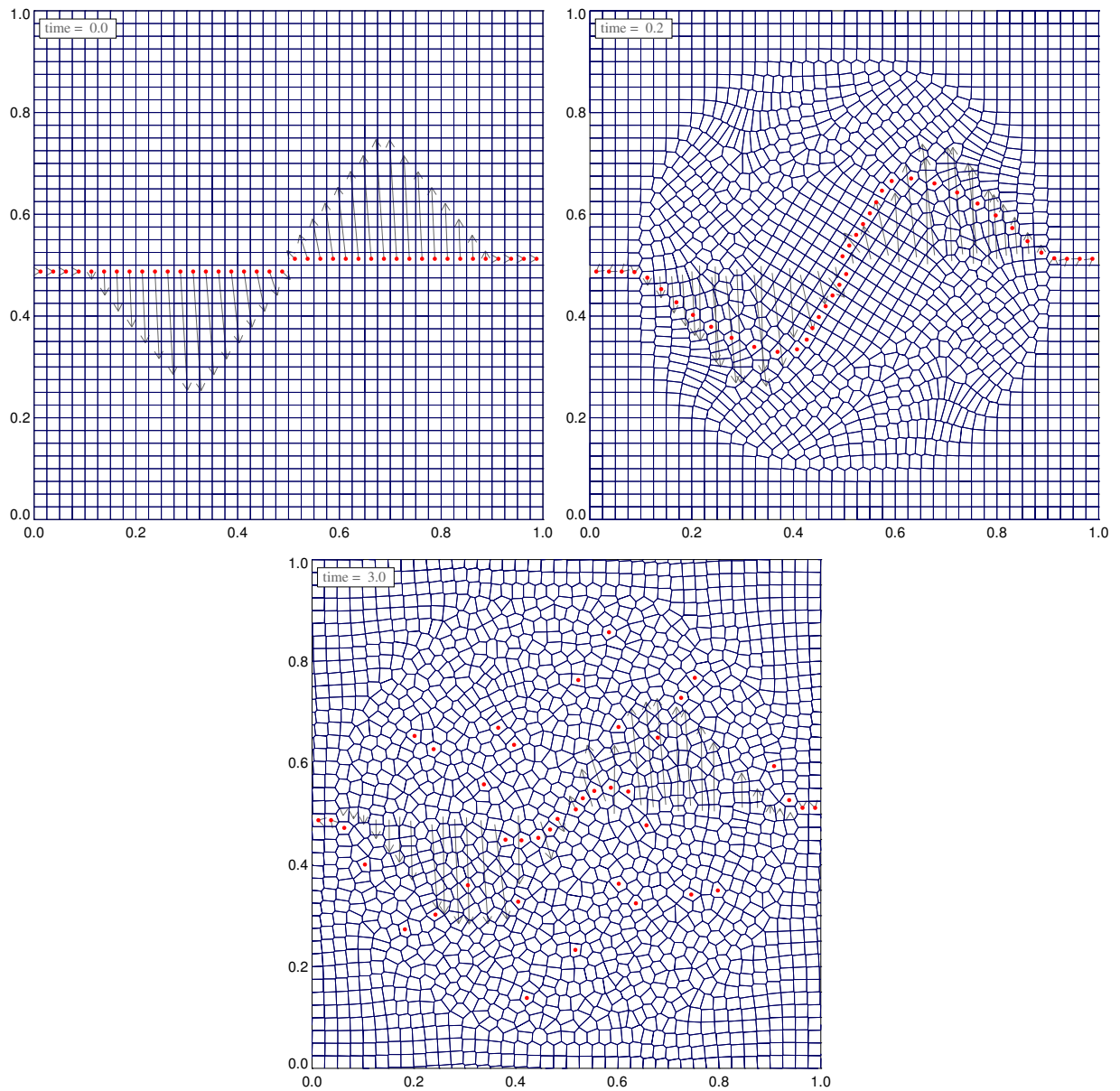
Figure 2.9: Illustration of the Lagrangian character of the mesh used in AREPO. (Top left): Initial conditions of a vortex setup, we see a cartesian grid/cells and some cells marked with red dots. The arrows indicate the initial velocities. (Top right): first time evolution of initial conditions. The points are moved with the velocities reshaping the voronoi mesh. (bottom): Grid after several time steps. The mesh is the middle is completely different from the initial one. The cells continuously move and the initially marked cells are completely redistributed, this illustrated the Lagrangian character of the mesh. Taken from (Springel, 2010).
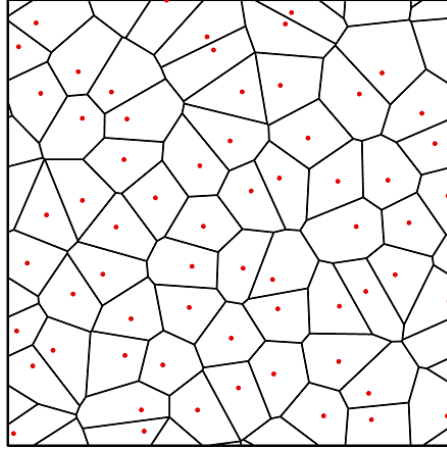
Figure 2.10: Illustration of a 2D spatial discretization by a voronoi tessellation of 64 mesh generating points (red dots). Taken from (Springel, 2010).

When the cells matches the derefinement criteria, it gets removed from the mesh, see Figure 2.11 (middle, right) There are different criteria that determine whether the cell is actually split or merged. We aim for cells with similar mass to avoid extreme momentum transfer. Hence we prescribe the mass to be within an interval of factor 2 to a target mass. If the cell mass is outside the interval the cell gets de- or refined. Further previous simulations indicate the cell should be split if its volume is larger than 8 times the volume of one of its neighbors. For our highly dynamical setup we additionally include a criterion based on the gradient (see. 3.2).

The cell is derefined if the cell mass drops below 0.5 times the prescribed cell mass. We combined this scheme with the gradient based derefinement (see 3.2).

When a cell is split the mesh generating point is replaced by a pair of very close points, hence keeping the surrounding mesh unchanged. The points are randomly positioned at $0.025 \, r_{cell}$ from the original point position, with cell radius

$$r_{cell} = \left(\frac{3V}{4\pi} \right)^{1/3} .$$

(2.53)

The quantities of the cell are then distributed conservatively along the cells according to their volume ratio. In the derefinement case a point is removed from the mesh (see Figure 2.11 and its quantities are distributed to the neighboring cells according to their volumes.
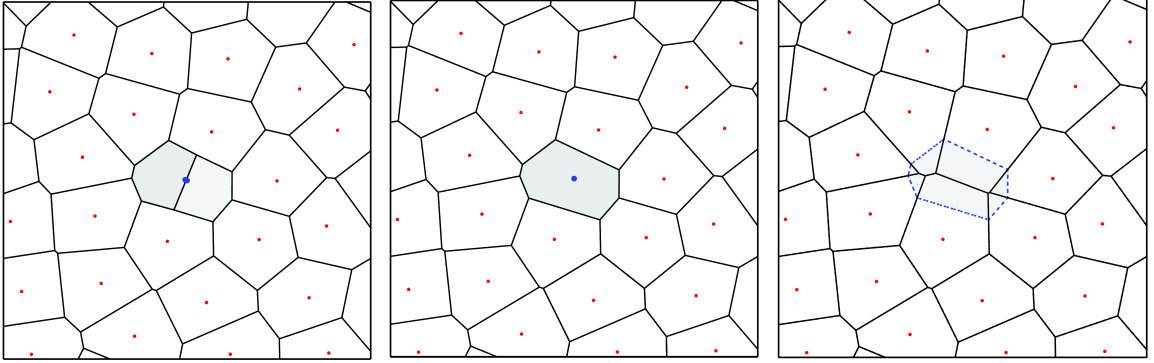
Figure 2.11: Example refine and derefinement of 2D voronoi mesh. (left) (middle) (right), extracted from (Springel, 2010)

2.4.3 Local time steps

Generally in homogeneous systems are simulated with a single time step. This is usually done by a CFL scheme that uses the sound speed

$$c_s = \sqrt{\frac{\gamma P}{\rho}} \tag{2.54}$$

with pressure P and density ρ, to calculate the maximum allowed time step for each cell i by

$$\Delta t_i = C_{\text{CFL}} \frac{R_i}{c_i + |\boldsymbol{v}'_i|}. \tag{2.55}$$

$R_i = (3\pi/4V_i)^{1/3}$ is the cell radius estimated by assuming a spherical cell, $C_{\text{CFL}} \sim 0.3 - 0.8$ the Courant-Friedrichs–Levy and $\boldsymbol{v}'_i = \boldsymbol{v}_i - \boldsymbol{w}$ is the relative velocity of the gas to the grid motion. We choose $C_{\text{CFL}} = 0.3$, according to previous simulations. The overall time step is then selected as

$$\Delta t = \min_i \Delta t_i \tag{2.56}$$

which prescribes the entire system evolution and can become very small in high temperature and dynamical regions. Hence AREPO provides the feature of locally adaptive individual time steps.

The code uses time steps within a power-of-two hierarchy in which the time step of each cell Δt_i is determined by the largest power of 2 subdivision that is smaller than the criterion of eq. (2.55). AREPO provides individual adapted time evolution of each cell in its local environment. This allows for highly dynamical parts to be evolved with a smaller time step and less dynamical ones with a larger one. Leaving larger parts of the mesh unaffected leads to an computational advantage.

That leads to an overall and partial synchronization of cells after their individual evolution. If neighboring cells have different time steps the shared face is evolved with the smaller step. This is illustrated in Fig. 2.12. There are three different time steps used ($\Delta t/2$, Δt,
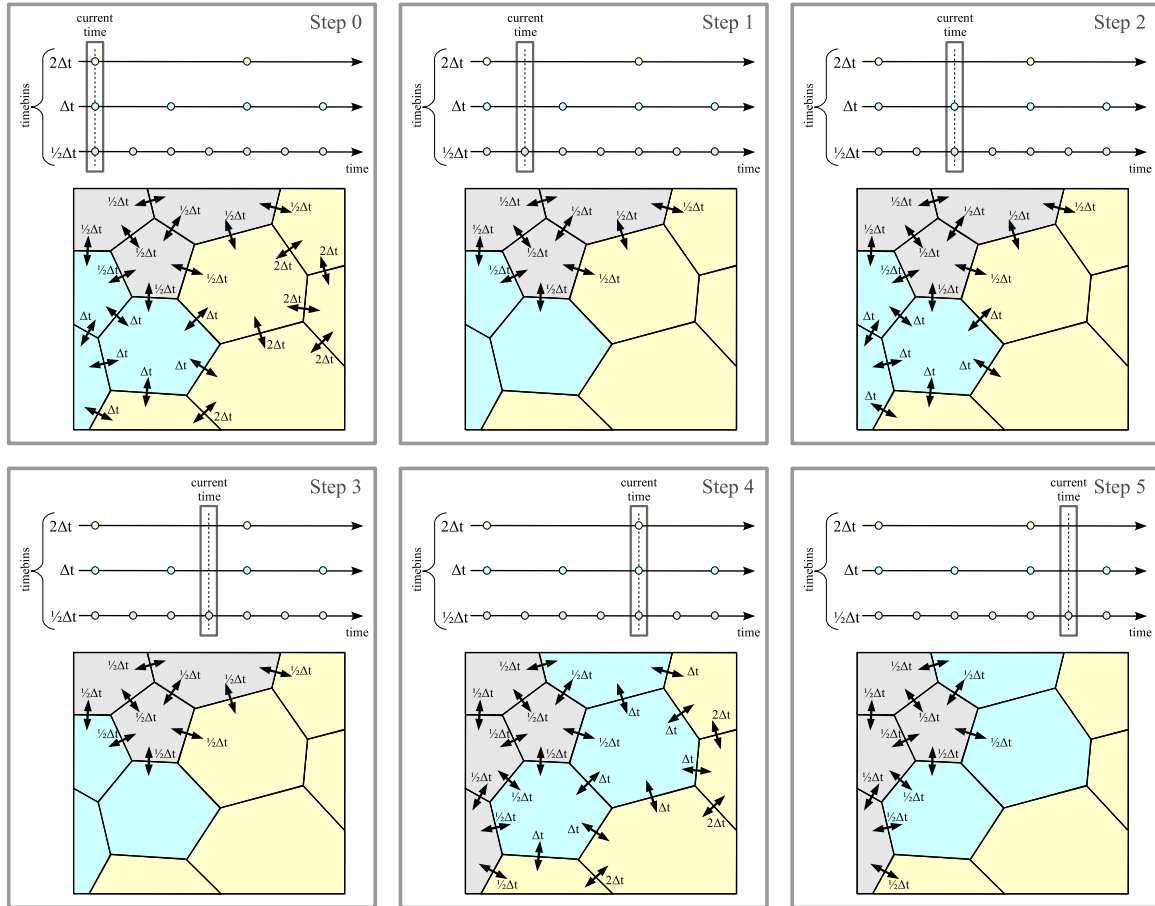
Figure 2.12: Sketch of the individual time integration scheme used in AREPO for the hydrodynamics. The mesh cells in this example occupy three different time-bins, and are colored accordingly in the sketch. In each time-step, fluxes are calculated for all faces where at least one of the cells is active on the current time-step. The cells then exchange conserved quantities on the smaller of the two time-step sizes of the two neighboring cells of each active face. A cell has the possibility to reduce its time-steps at the end of each step, but can only move to a time-step twice larger every second step in order to maintain a nested synchronization of the time-step hierarchy. Taken from (Springel, 2010)

$2\Delta t$) indicated by different coloring of the cells (grey, blue, yellow). The current step that synchronizes all cells is shown in "Step 0". After the synchronization the voronoi mesh is generated for all cells and the fluxes are estimated. With those the conservative variables (mass, momentum, energy) are updated for each neighboring pair of cells. "Step 1" represents the next step in which cells with the smallest local time step $\Delta t/2$ are advanced together with their shared faces. The interaction is calculated and the conservative variables are updated for all cells that had interacting faces in this time step. The primitive variables (density, velocity, pressure) are only updated for those cells that completed their time step with that step (grey).

In "Step 1" only a few faces are active and hence only those cells with at least one active face are constructed in the mesh. For those cells the process repeats and the conservative variables are updated, see "Step 2" and 3.

Whenever a cell fully completes its time step the primitive variables of that cell are updated according to the accumulation of changes of its conservative variables. Now the time step can be adapted to the local dynamics by either be set larger, smaller or remain constant. The cells time step can be lowered every time the cells time step passed. However it can only set to a larger value whenever all local cells are synchronized. This is illustrated in "Step 4" in which cells both grew or lowered their time step. With "Step 5" the process restarts for the new mesh. It has been tested (Springel, 2010) that this method is as accurate as advancing the mesh with global time steps.

This processing works for cell velocities below the local sound speed. In shocks this is no longer true, thus in highly dynamical regions the time step has to be further constrained. Therefore the idea is to calculate a connecting signal speed for each individual pair of cells

$$v_{ij}^{\mathrm{sig}} = c_i + c_j - \frac{\boldsymbol{v}_{ij} \cdot \boldsymbol{r}_{ij}}{|\boldsymbol{r}_{ij}|} \tag{2.57}$$

with sound speeds $c_{i,j}$ and relative velocity $\boldsymbol{v}_{ij}$ and position $\boldsymbol{r}_{ij}$. With that the time step is assigned according to

$$\Delta t_i = \min_{i \neq j} \left(\frac{|\boldsymbol{r}_{ij}|}{v_{ij}^{\mathrm{sig}}}, \frac{R_i}{c_i + |\boldsymbol{v}_i'|} \right). \tag{2.58}$$

However this scheme is a N^2 problem to be solved which slows down the computational speed. Hence this is combined with a tree walk to reduce it to a N log(N) problem. Therefore the maximum sound speed c^{max} and velocity of cells v^{max} are stored for each node. First the head node is assigned an initial time step $\Delta t_{\mathrm{current}} = \frac{R_i}{c_i + |\boldsymbol{v}_i'|}$, that is changed if the walk hits a particle for which $\frac{|\boldsymbol{r}_{ij}|}{v_{ij}^{\mathrm{sig}}} < \Delta t_{\mathrm{current}}$. If the walk hits another node then with v^{max} and c^{max} it is checked whether any particle inside the node can have a smaller time step. If that is true, the node is opened and other wise the node is ignored. When the tree walk is finished the time step is assigned the value

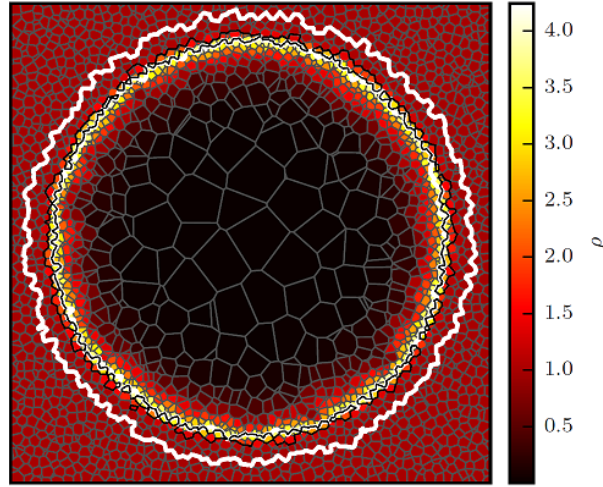$$\Delta t = C_{\mathrm{CFL}} \Delta t_{\mathrm{current}}. \tag{2.59}$$

Figure 2.13: Illustration of the shock zone (white contour lines) and surface (black contour lines) on in a slice through density profile of a 3D Sedov Taylor point explosion. It further contains the voronoi mesh (grey lines surrounding the cells) (Pfrommer et al., 2016).

2.4.4 Shock finder

We would like to identify shocks in our simulations, to be able to compare CR shock acceleration at SN remnants with CR injection in SN explosion. This needs a proper identification of the shocks. Therefore we include the shock finder developed for AREPO by Schaal & Springel (2014). The methodology of the shock finder is explained below.

There are several steps on finding the shock (Ryu et al., 2003; Skillman et al., 2008; Hong et al., 2014). In first place three criteria are checked that narrow down the volume that contains the shock, i. e. define the so called shock zone. The criteria are given by

$$\text{(i)} \quad \boldsymbol{\nabla} \cdot \boldsymbol{v} < 0 \tag{2.60}$$

$$\text{(ii)} \quad \boldsymbol{\nabla} T \cdot \boldsymbol{\nabla} \rho > 0 \tag{2.61}$$

$$\text{(iii)} \quad \Delta \log(T) \geq \log \left(\frac{T_2}{T_1} \right) \Bigg|_{\mathcal{M}=\mathcal{M}_{min}} \wedge \; \Delta \log(p) \geq \log \left(\frac{p_2}{p_1} \right) \Bigg|_{\mathcal{M}=\mathcal{M}_{min}} \tag{2.62}$$

where (i) represents a compression criterion, which is always fulfilled wherever a shock is present. The second one ensures that the mass flow ($\boldsymbol{\nabla}\rho$) and the temperature gradient ($\boldsymbol{\nabla}T$) are aligned. This filters out spurious shock detections by (i) that might occur in shear flows or cold fronts. The third criterion is used to filter numerical noise and errors and consists out of two conditions. First ensures a minimum temperature jump across the shock and the second for the pressure respectively. This combination discriminates against tangential discontinuities and contacts. When applied in AREPO the shock finder enables to follow the shock propagation. The cells of the shock surface and zone are marked and traced. Figure 2.13 shows the shock finder applied to a Sedov-Taylor explosion in a homogeneous medium after a certain expansion time. The shock zone and surface are

colored by the white and black contour lines, respectively. Within the shock zone the shock is identified as the cell of maximum compression. For each cell the possible shock direction is calculated by the local temperature gradient of the cell given by

$$\boldsymbol{d}_s = -\frac{\boldsymbol{\nabla}T}{|\boldsymbol{\nabla}T|}. \tag{2.63}$$

The local temperature gradient $\boldsymbol{\nabla}T$ is calculated by the second-order accurate gradient operator used in AREPO (Ryu et al., 2003; Schaal & Springel, 2014).

3 Setup and adjustments

This chapter provides the basic information on our setup and how we build new initial conditions for the runs. Further we explain the major changes we brought to the code described in 2.3.

3.1 Setup

We focus on a fraction of the galactic disk to increase the spatial resolution such that we resolve the Sedov-Taylor phase of individual SNe. To study the outflow behavior we model that fraction of the disk inside a stratified, i.e. in z-direction elongated, box. We use a stratified box setup with a size of $(0.5)^2 \times (\pm 5) \, (\mathrm{kpc})^3$ and center the midplane of the galactic disk at $5 \, \mathrm{kpc}$, similar to previous works (Girichidis et al., 2016b, 2018b).

3.1.1 Initial conditions

To generate the Voronoi mesh on which this work is based, the initial positions of the particles/cells have to be prescribed. The positioning and the number of cells determine the initial resolution. For a uniform density, glass like initial conditions with an equal cell number in each dimension, e.g. 50^3, are popular, in which all cells are assigned equal masses. However our setup contains a non uniform density profile and thus needs an adaptation in cell distribution according to the set density profile.

We choose a common used Gaussian density profile described by

$$\rho(z) = \rho_{\mathrm{mid}} \left[c_{\mathrm{floor}} + \exp\left(-\left\{ \frac{z - z_{\mathrm{mid}}}{2h_z} \right\}^2 \right) \right], \tag{3.1}$$

with the midplane height z_{mid} and density ρ_{mid}, a constant density floor $c_{\mathrm{floor}} = 10^{-4}$ and the scale height (width) of the disk $h_z = 50 \, \mathrm{pc}$. The midplane density is calculated such that the overall surface mass density of the box is given by

$$\Sigma_{\mathrm{box}} = 10 \, \mathrm{M}_\odot \mathrm{pc}^{-2}, \tag{3.2}$$

similar to the solar neighborhood (Flynn et al., 2006). Thus we yield a midplane density of

$$\rho_{\mathrm{mid}} = \frac{\Sigma_{\mathrm{box}}}{\int \left[c_{\mathrm{floor}} + \exp\left(-\left\{ \frac{z - z_{\mathrm{mid}}}{2h_z} \right\}^2 \right) \right] \mathrm{d}z} = 3.79 \times 10^{-24} \, \mathrm{g \, cm}^{-3}. \tag{3.3}$$
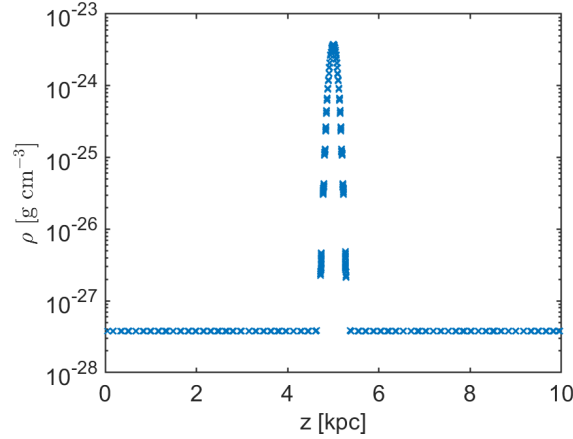
Figure 3.1: Initial density profile, where density is a function of height z.

In our setup most of the mass and hence the dynamics is focused to the midplane region. Therefore we desire a higher resolution in those parts. The outer parts are only lately influenced by the dynamics and hence we want a lower initial resolution, which further positively affects the run time in the early simulation state. To obtain such a mass based resolution the positions of the cells are linked to the applied density profile.

Further we want to ensure an equal cell mass for all cells. With this we reduce the possibility of a high mass cell transferring an large amount of its momentum to a small mass cell, that then will reach high unphysical velocities. To fit the requirements of equal cell mass and a resolution linked to the density we proceed as follows:

First we fix the initial cell number. In this work we set the initial cell number to $N_{\text{cell,tot}} = 10^5$. With the given mass surface density (3.2) we calculate the total mass contained in the box and the averaged individual cell mass

$$M_{\text{box,tot}} = \Sigma_{\text{box}} \cdot L_x^2 = 2.5 \times 10^6 \, M_\odot, \tag{3.4}$$

$$m_{\text{cell}} = \frac{M_{\text{box,tot}}}{N_{\text{cell,tot}}} = 25 \, M_\odot. \tag{3.5}$$

Given equal cell masses this results in an uneven cell distribution in z-direction, i.e. layers of different widths along the z coordinate.

In the next step we assume cubic cells in each layer of cells making the layer's cells uniform. With that we can calculate the number of cells in each layer by

$$n_{\text{cell}}(z) = n_x \cdot n_y = \frac{L_x}{\Delta x_{\text{cell}}} \cdot \frac{L_y}{\Delta y_{\text{cell}}} = \frac{L_x^2}{(\Delta z_{\text{cell}})^2}, \tag{3.6}$$

with an uniform box length in x- and y-direction $L_x = L_y$ and equal cell widths in x-, y- and z-direction $\Delta x_{\text{cell}} = \Delta y_{\text{cell}} = \Delta z_{\text{cell}}$. The layer's thickness is given by the local cell width along the z coordinate $\Delta z_{\text{layer}} = \Delta z_{\text{cell}}$.

The cell number each layer combined with the average cell mass provides the mass of the

layer. To obtain the thickness of the layer and thus the width of the cells, we calculate the mass of each layer by two different formula and set them equal. Hence we obtain

$$M_{\text{layer}} = \Sigma_{\text{layer}} \cdot L_x^2 \ \& \ M_{\text{layer}} = n_{\text{cell}}(z) \cdot m_{\text{cell}}, \tag{3.7}$$

$$\Rightarrow \Sigma_{\text{layer}} \cdot L_x^2 = n_{\text{cell}}(z) \cdot m_{\text{cell}}, \tag{3.8}$$

$$\Leftrightarrow \Sigma_{\text{layer}}(\Delta z_{\text{layer}})^2 = m_{\text{cell}} \tag{3.9}$$

with $\Sigma_{\text{layer}} = \int_{z_1}^{z_2} \rho(z)dz$ and $\Delta z_{\text{layer}} = \Delta z_{\text{cell}} = z_2\text{-}z_1$. With this we equally space all cells in each layer, starting from a small distance from the boundary positions. Further we add a random offset to the original coordinates, up to one third of the current layer thickness, to prevent the formation of a cartesian like mesh.

External gravitational potential

When simulating parts of galaxies it has to be ensured to include wide ranging effects, e.g. the gravitation of the entire galaxy disk. Hence we add a static gravitational potential of a Milky Way like galaxy to our setup. The stratified box is set within a solar neighborhood like region. The gravitational potential has two components: a baryonic disk and a dark matter halo, same as Li et al. (2017). The dark matter halo is described by a NFW profile projected to the z-direction (3.14). The baryonic component is modeled by an iso-thermal velocity dispersion and hence of the form of (3.15) These are the equations prescribing the parameters needed for calculating the gravitational potential.

$$r = \sqrt{((z\text{-}z_{\text{mid}})^2 + R_{\text{D}}^2)} \tag{3.10}$$

$$g_{\text{DM}} = GM_{\text{DM}} \cdot \frac{z\text{-}z_{\text{mid}}}{r^3} \tag{3.14}$$

$$R_{\text{S}} = \frac{R_{\text{vir}}}{c} \tag{3.11}$$

$$g_{\text{gas}} = 2\pi\Sigma_\star \cdot \tanh\left(\frac{z\text{-}z_{\text{mid}}}{z_\star}\right) \tag{3.15}$$

$$\rho_{\text{DM}} = 200 \langle\rho_{\text{DM}}\rangle \cdot c\,(c+1)^2 \tag{3.12}$$

$$g_{\text{tot}} = g_{\text{DM}} + g_{\text{gas}} \tag{3.16}$$

$$M_{\text{DM}} = 4\pi\rho_{\text{DM}}R_{\text{S}}^3 \cdot \left(\log\left(1 + \frac{r}{R_{\text{S}}}\right) - \frac{r}{r + R_{\text{S}}}\right) \tag{3.13}$$

Table 3.1 contains all parameters needed for the calculation and the values are chosen similar to observational values of the solar neighborhood. The resulting gravitational acceleration from equations (3.10)-(3.16) is illustrated in Figure 3.2. Within the midplane (5 kpc) and up to 2 kpc above and below it ($\sim$ 7 kpc) the baryonic part (red) dominates the dark matter (black).

Table 3.1: Values of physical parameters to calculate the external gravitational potential used in the simulations. These parameters are chosen to be comparable to the values of these parameters within the solar neighborhood. R_{vir} corresponds to the virial radius of the host galaxy, c is the concentration parameter $c = r_{200}/r_s$, $\langle \rho_{\mathrm{DM}} \rangle$ is the average cosmic dark matter density at redshift 0, $\Sigma_\star$ the stellar surface mass density, $z_\star$ the height of gas and stars in the stellar disk, R_{D} the distance from the galactic center within the disk plane.

R_{vir} [kpc]	200.0	(Navarro et al., 1997)
c [1]	12.0	(Navarro et al., 1997)
$\langle \rho_{\mathrm{DM}} \rangle$ [g cm^{-3}]	$0.3 \cdot 8.62 \times 10^{-30}$	(Navarro et al., 1997)
$\Sigma_\star$ [M$_\odot$ pc^{-2}]	30.0	(Binney, 2008)
$z_\star$ [pc]	300.0	(Binney, 2008)
R_{D} [kpc]	8.0	
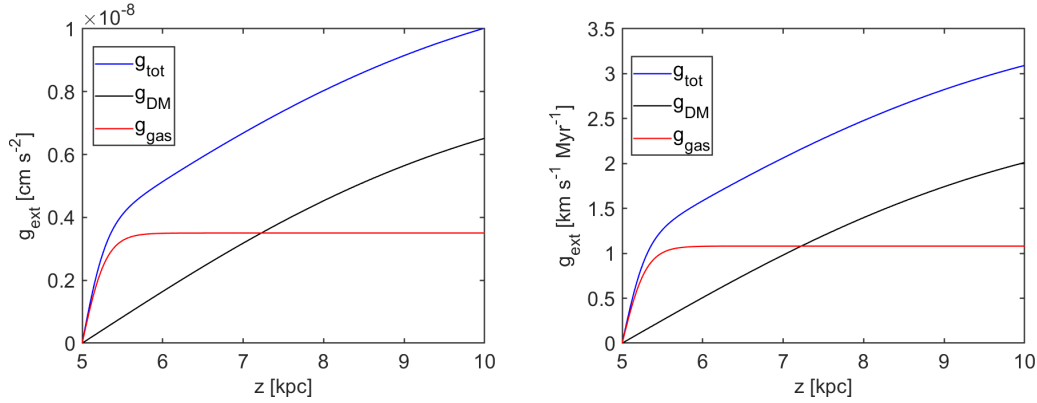
Figure 3.2: External gravitational acceleration (blue) above the midplane located at 5 kpc, consisting of stellar/gaseous component (red) and dark matter (black). (left) cgs units, (right) converted to large scale units.

Magnetic field

We include MHD and hence an initial magnetic field is included. In the initial conditions the magnetic field is aligned along the x-axis and expressed as a function of the local density

$$B_x(z) = B_{x,0} \cdot \left(\frac{\rho(z)}{\rho_{\mathrm{mid}}} \right)^{0.5}. \tag{3.17}$$

The initial peak of the magnetic field within the midplane is set to $B_0 = 3\,\mu\mathrm{G}$ as it is described by Beck & Wielebinski (2013). The density scaling is a commonly used one (Girichidis et al., 2016b). The pressure resulting from the magnetic field is given by

$$P_{\mathrm{mag}} = \frac{B^2}{8\pi} = \frac{B_0^2}{8\pi} \left(\frac{\rho(z)}{\rho_{\mathrm{mid}}} \right) \tag{3.18}$$
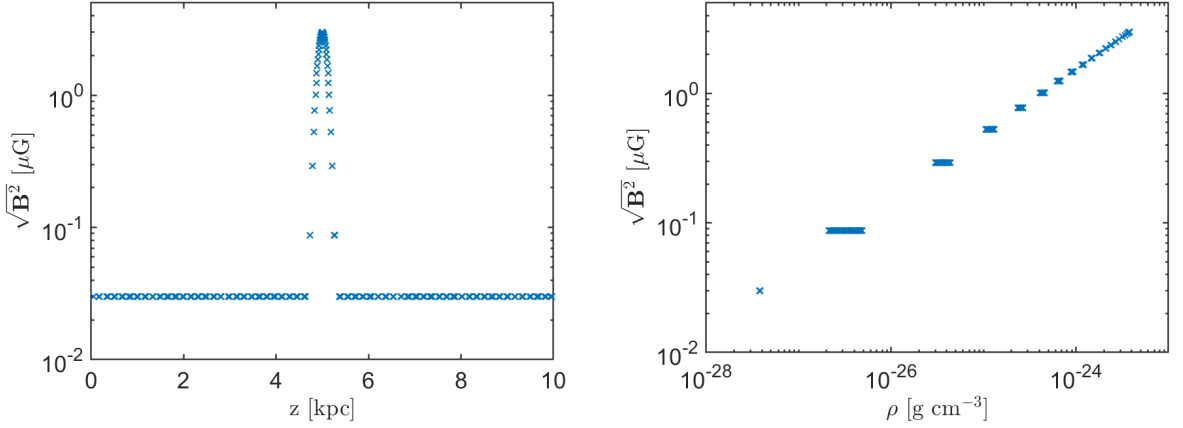
Figure 3.3: Initial magnetic field as a function of scale height (left) and density (right).

Hydrostatic equilibrium

In order to achieve a stable disk the external gravitational potential and the internal energy have to be in hydrostatic equilibrium. This is achieved by solving the following equation

$$\frac{\mathrm{d}P_{\mathrm{tot}}}{\mathrm{d}z} = -g(z)\rho(z), \tag{3.19}$$

with total pressure P_{tot}, gravitational acceleration g and density rho. The total pressure is split up into the thermal pressure P_{th} and the magnetic pressure P_{mag}. By splitting up the pressure into these two components the thermal pressure of the initial condition is obtained by rearranging (3.19) to

$$\frac{\mathrm{d}P_{\mathrm{th}}}{\mathrm{d}z} = -g(z)\rho(z) - \frac{\mathrm{d}P_{\mathrm{mag}}}{\mathrm{d}z}. \tag{3.20}$$

By integrating both sides (3.20) with respect to z, it can be solved for the thermal pressure at height z $P_{\mathrm{th}}(z)$

$$\int_0^z \frac{\mathrm{d}P_{\mathrm{th}}}{\mathrm{d}z'}\mathrm{d}z' = \int_0^z -g(z')\rho(z')\mathrm{d}z' - \int_0^z \frac{\mathrm{d}P_{\mathrm{mag}}}{\mathrm{d}z'}\mathrm{d}z' \tag{3.21}$$

$$\Leftrightarrow P_{\mathrm{th}}(z) = P_{\mathrm{th}}(0) - \int_0^z g(z')\rho(z')\mathrm{d}z' - [P_{\mathrm{mag}}(z) - P_{\mathrm{mag}}(0)] \tag{3.22}$$

$$\Rightarrow P_{\mathrm{th}}(z) = P_{\mathrm{th}}(0) + \frac{B_0^2}{8\pi\rho_{\mathrm{mid}}}[\rho(0) - \rho(z)] - \int_0^z g(z')\rho(z')\mathrm{d}z'. \tag{3.23}$$

The integral over the gravitational acceleration times the density is solved numerically and hence this method can be used for any density profile applied. The thermal pressure at position $z = 0$, the lower box boundary, is assumed to be given by an ideal thermal gas, outside the galaxy, with a temperature of 10^6 K. With the thermal pressure the internal energy u is calculated by:

$$u = \frac{P_{\mathrm{th}}}{(\gamma - 1)\rho} \tag{3.24}$$
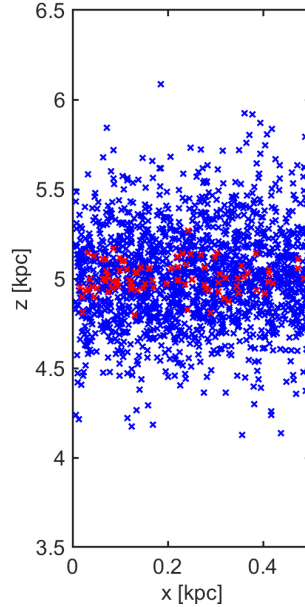
Figure 3.4: Vertical projected distribution of the included SNe positions. Blue crosses are individual and red ones clustered SNe.

3.1.2 Determining the supernova positions

We determine the SN positions with an external code written by Philipp Girichidis and save the times and positions in a text file. With this we ensure identical regions in which the SNe explode. The positions are determined by the following scheme.
Following Kennicutt Jr (1998) we determine a global star formation rate surface density

$$\Sigma_{\text{SFR}} = 2.5 \times 10^{-4} \left(\frac{\Sigma_{\text{gas}}}{1 M_\odot \, \text{pc}^{-2}} \right)^{1.4} M_\odot \, \text{yr}^{-1} \, \text{kpc}^{-2} = 0.00628 \, M_\odot \, \text{yr}^{-1} \, \text{kpc}^{-2}, \quad (3.25)$$

from which we then calculate the star formation rate of the entire box

$$\dot{M}_{\text{SFR}} = \Sigma_{\text{SFR}} \cdot L_x^2 = 1570 \, M_\odot \, \text{Myr}^{-1}. \quad (3.26)$$

We assume a Salpeter initial mass function (Salpeter, 1955), with a low-mass cutoff at $0.01 \, M_\odot$ and a high-mass cutoff at $60 \, M_\odot$, which yields one massive star (M$> 8 \, M_\odot$) per $100 \, M_\odot$ and hence we obtain a constant SN rate of ~ 15 SN Myr^{-1}. Following averaged observational constrains on the SN positions and types, we split up the total number of SNe into a fraction of 0.2 SN type I and 0.8 type II SNe. Energetically they are similar but come with different scale heights within the galaxy and hence have to be differentiated when determining the positions. Type II SNe are split up into clusters of SNe and individual ones. We choose the fraction of type II SNe exploding in stellar clusters is 0.6 (Cowie et al., 1979). The positions of the clustered SNe are fixed. They have a different scale heights as individual type II SNe too. We choose a scale height of 325 pc, 80 pc and 240 pc for type I, clustered type II and individual type II SNe respectively, adopted to Miller & Scalo (1979);

Heiles (1987); Tammann et al. (1994); de Avillez & Breitschwerdt (2004).

The positions are determined according to a Gaussian distribution with their individual scale heights σ_i of the SN types and hence are given by

$$z_i = \exp\left(-\frac{z^2}{2\sigma_i^2}\right). \tag{3.27}$$

Within the x- and y-plane the SNe are distributed uniformly.

Each cluster of SNe is different. They contain at least $n_{\min} = 7$ and up to $n_{\max} = 40$ SNe per cluster. The exact number per cluster is determined by

$$N_{\mathrm{SN}} = \frac{1}{\alpha \cdot \left(\frac{1}{n_{\max}} - \frac{1}{n_{\min}}\right) + \frac{1}{n_{\min}}} \tag{3.28}$$

with a random number α between 0 and 1 which is linked to the probability P of a cluster hosting N_{SN}. The probability follows a power law distribution with $P \propto N_{\mathrm{SN}}^{-2}$ (Kennicutt Jr et al., 1989; McKee & Williams, 1997; Clarke & Oey, 2002). We include clusters with an average life time of $\tau_{\mathrm{clus}} = 40\,\mathrm{Myr}$ which then leads to a supernova timing within the cluster of

$$dt_{\mathrm{SN}} = \frac{\tau_{\mathrm{clus}}}{N_{\mathrm{SN}}}. \tag{3.29}$$

An illustration all SN positions over 200 Myr is shown in Figure 3.4. Each point represents a SN. This is a projection of the SN positions onto the x-z-plane. Individual SNe (blue) can reach out up to $\sim 1\,\mathrm{kpc}$ above/below the midplane, where as clusters (red) are located within 200 pc above and below.

Supernovae treatment in AREPO

We generate a table with SN times and positions. In each time step we then check whether a SN is due. Therefore we compare the SN times to the current and previous times. If they lie in between we proceed by passing the SN position(s) to further proceedings.

For all SN position AREPO then finds the nearest neighbors within a sphere. Initially the search radius is set to the average cell radius. We seek for 27 injections cells to resolve the Sedov-Taylor phase. If there are less than 27 cells within the sphere of initial radius, the radius is doubled and the procedure repeats. When there are more than 27 cells the radius is reduced. Once we found exactly 27 cells the energy is distributed among them according to their mass fractions.

We try to inject a total amount of $10^{51}\,\mathrm{erg}$ for each SN. However this energy is split up into thermal energy and CR energy, depending on the chosen CR fraction in the SNe. To enhance performance we further build in a maximum temperature threshold that cannot be exceeded by injection. Here we choose $10^9\,\mathrm{K}$. If the injection would lead to higher temperatures, we only inject the difference to our maximum temperature as thermal energy. When the cell already is at a temperature larger than $10^9\,\mathrm{K}$ we do not inject any energy into that cell. With this we obtain a difference between the tabulated energy and the effectively
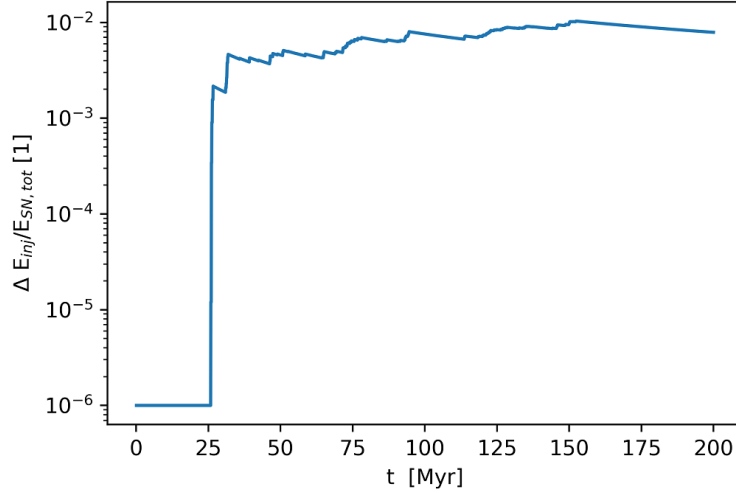
Figure 3.5: Time evolution of the energy difference induced by maximum temperature threshold.

injected energy, however that error is negligibly small, see Figure 3.5 and enhances the code performance tremendously. The total SN energy is the summed up theoretical injection (SN rate times SN energy times time). ΔE_{inj} is the summed up amount of energy we do not inject due to the threshold. This only effects the simulation after ~ 25 Myr and only rises up to slightly less than one percent. Hence we keep this scheme to boost the performance.

3.2 Code adaptations

In our work we investigate the highly dynamical ISM, which required additions and modifications to the code.

Gradient-based refinement

The highly dynamical environment of the ISM results in steep gradients to which the basic refinement and derefinement included are not able to adapt (see Figure 3.6 (left 2)). The cells grow too big and especially the elongated cells are source of errors as they connect very low and high density regions by only one cell. Therefore we provide a further criterion based on gradients. We check the gradient of the total magnetic field B, total velocity v and density ρ of the cells and compare them to the total values of the properties. We refine the cell by splitting it in 2 subcells if the cells quantities match the following criterion

$$\frac{\boldsymbol{\nabla}\alpha \cdot r_{\text{cell}}}{|\alpha|} \geq 1.2, \tag{3.30}$$

here α represents either B, v, ρ and r_{cell} is the averaged cell radius assuming a spherical cell. The value 1.2 is the critical value that determines harshness of the refinement and is
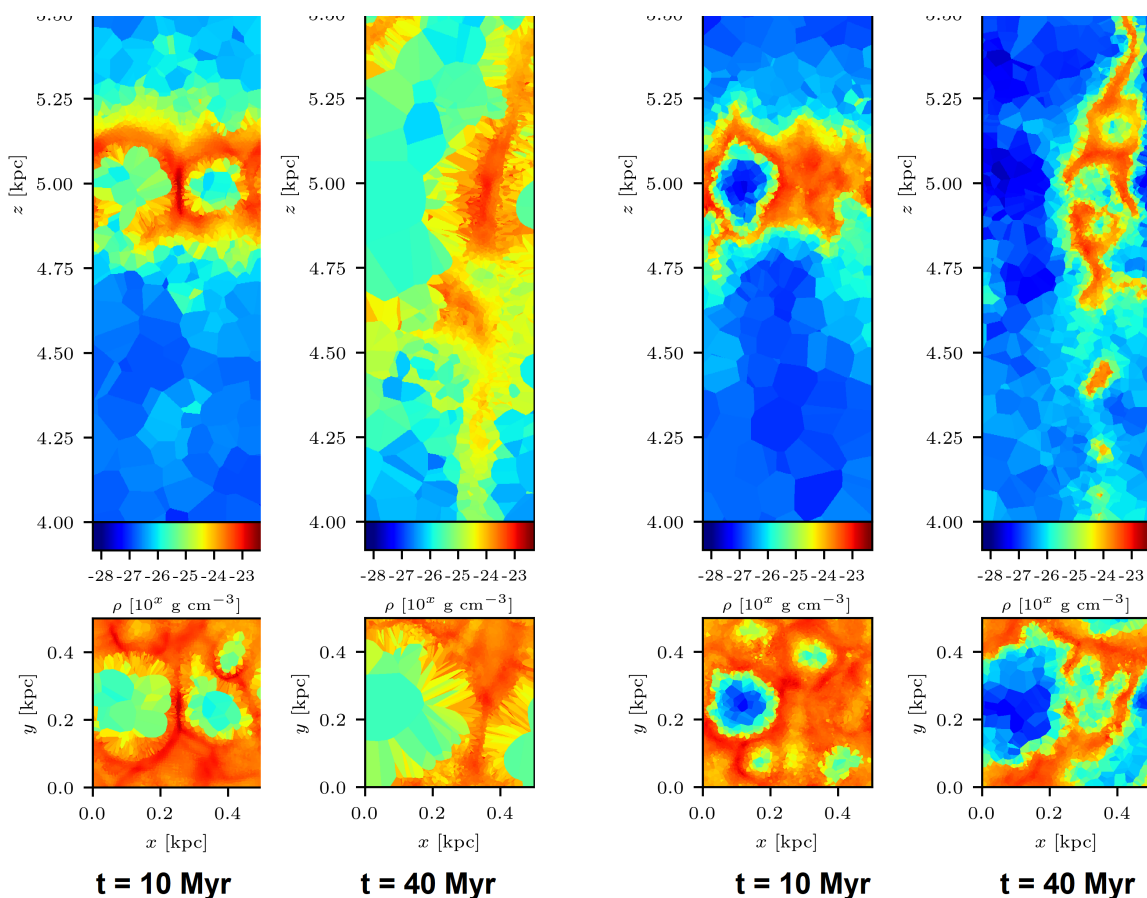
Figure 3.6: Example of cells to which the refinement was not able to adapt without the gradient-based refinement (left panels). In comparison are the right panels show the image where the included gradient refinement has no problem adopting to the dynamics.

set to its value to reach an in-/decrease of a property value by a factor of 10 over the next 10 cells. With this cells remain a more spherical shape.

The same is done for the derefinement. If the gradient is flat enough we allow for cells merging. The derefinement criterion is given by

$$\frac{\boldsymbol{\nabla}\alpha \cdot r_{\text{cell}}}{|\alpha|} \leq 0.3, \tag{3.31}$$

with the same variables from 3.30. The critical factor of derefinement is set to $\frac{1}{4}$ of the refinements factor.

Additionally to the new included refinement criterion, we softened the roundness property of the refinement. This criterion checks whether the cell is in a rudimentary spherical shape. The clustered SNe drive strong and fast changes, to which the mesh adopts by reshaping the cells. This may lead to non spherical cells which then no longer fit the checkup criterion of the refinement. With this we ensure more spherical cells in all regions.

The result of the new refinement is shown on the two right panels of Figure 3.6. The cells are smooth and "rounder" compared to the left ones without refinement. Even at early times (10 Myr) it has a huge impact and at later times (40 Myr) is indispensable for running the simulations. Note that there are two different SN tables used for the left and right panels. However the effect is independent on the exact position.

4 Results

4.1 Initial conditions

In order to obtain reliable results from the simulation it is crucial that the initial conditions do not inherit any wide ranging dynamics by itself. Therefore it is important to create
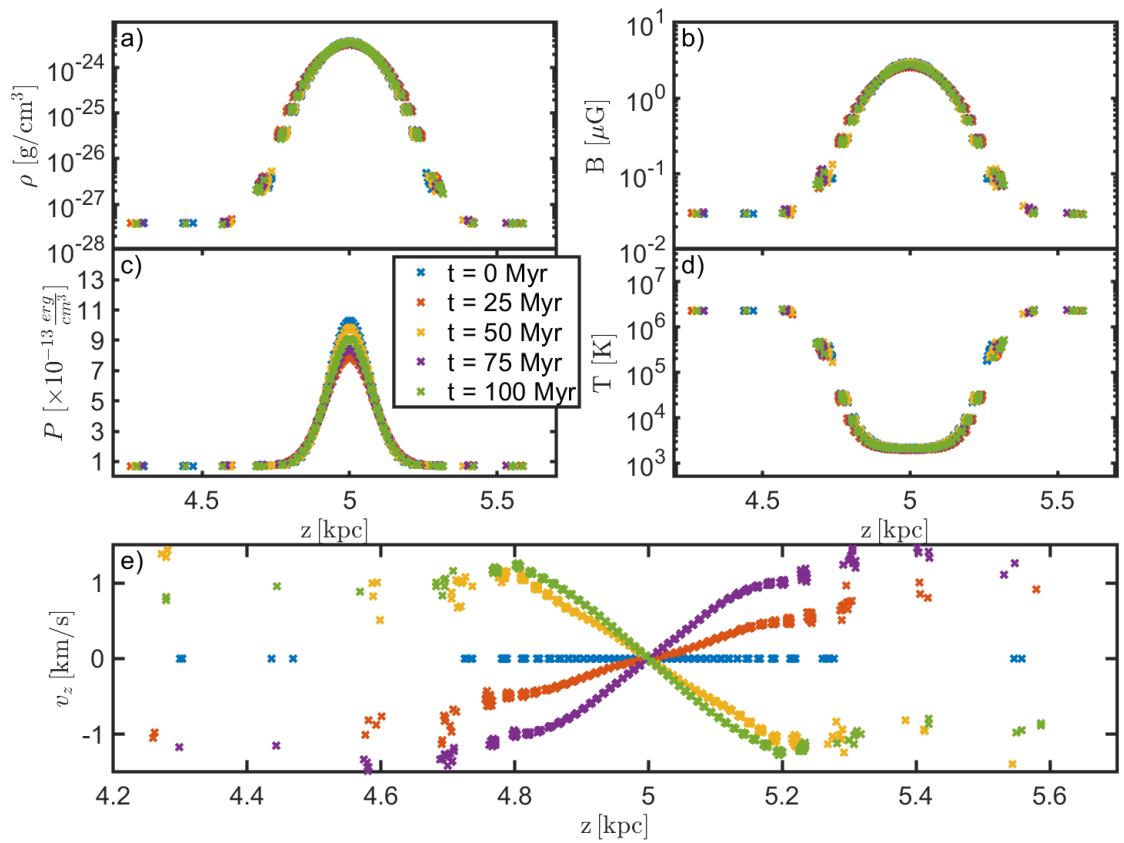
Figure 4.1: Time evolution of the initial state in hydrostatic equilibrium. a) displays the evolution of the density profile, b) the magnetic field, c) the total pressure, d) the temperature and e) the local velocities. The different colors indicate different times (see legend).

physical initial conditions that are stable under the influence of gravity. Thus the hydrostatic equilibrium described above is applied to the initial conditions. Figure 4.1 contains
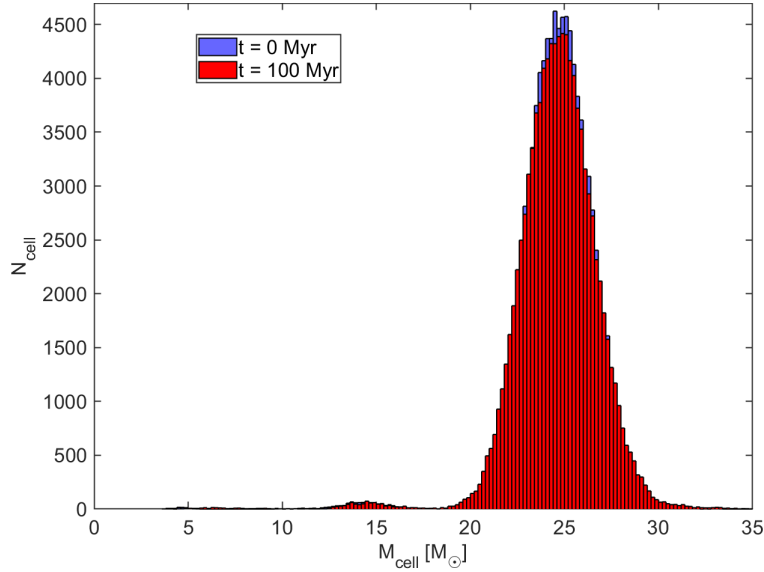
Figure 4.2: Histogram of the cell mass in the initial conditions (blue) bins and after 100 Myr in hydrostatic equilibrium run (red).

the evolution (indicated by differently colored marks) of initial parameters as function of z-coordinate, plotted in close range of the disk centered at 5 kpc. We show only every tenth. The figure contains the density profile (a), total pressure (b), total magnetic field strength (c), temperature (d) and velocity in z-direction (e) for various evolution times given in the legend.

The initial conditions are given by the blue crosses at t = 0 Myr. As the system evolves over time there are only slight changes in all of the parameters, which leads to an overall conservation of the disk structure. The disk evolves with minor velocity components in z direction (panel e) that show a minor expansion and contraction oscillation. However this are minor dynamics with $v_z \approx 1 \mathrm{km\ s}^{-1}$ which do not drive major changes in the disk structures (panel a, b, c, d). With this we ensure that the dynamics of the disk itself do not influence our results.

As mentioned before, we want to ensure that the cell masses do not lead to large errors due to momentum transfer. Hence we ensure that the cell mass only varies by a factor of two with respect to our desired average value Figure 4.2 shows the mass histogram of the initial conditions (blue) and after time evolution in hydrostatic equilibrium to 100 Myr (red). The overall structure of the number distribution of cells with a certain mass is conserved. The distribution is peaked around 25 M$_\odot$ and follows a Gaussian shape, which is consistent with the prescribed density profile.

With both the real hydrostatic equilibrium and small mass variations we keep those two possible sources of errors as small as possible.

4.2 Global evolution

4.2.1 Simulations

Table 4.1 contains the parameters we used for the different simulations to investigate the properties of the ISM and outflows. The first column contains the simulation label, with INJ labeling the runs where we inject CR directly with the SNe energy and SF where we accelerated CRs at shock fronts identified by the shock finder. The second one the CR injection fraction, i.e. that amount of SNe energy we put in CR energy for the INJ runs and the acceleration efficiency, i.e. the effectiveness of energy transfer at shocks to CRs energy. The third column contains the applied CR diffusion coefficient for anisotropic diffusion perpendicular to the magnetic field.

We mainly compare the INJ simulations to each other and give a first statement on the applicability of the shock finding routine on the highly dynamical environment of the ISM.

Table 4.1: Overview of the simulation

Label	CR injection fraction	CR diffusion coefficient
INJ01	0.05	1×10^{28}
INJ02	0.05	3×10^{28}
INJ03	0.05	1×10^{29}
INJ04	0.10	1×10^{28}
INJ05	0.10	3×10^{28}
INJ06	0.10	1×10^{29}
INJ07	0.20	1×10^{28}
INJ08	0.20	3×10^{28}
INJ09	0.20	1×10^{29}
	acceleration efficiency	
SF01	0.10	3×10^{28}
SF02	0.10	1×10^{28}
SF03	0.10	1×10^{29}

All our INJ simulations involve structures similar to observed ones in galaxies. They contain multiple phases with a comparable distribution. We exclude the results of the SF runs until section 4.5, as the simulations are limited in their time to ~ 40 Myr. Figure 4.3 shows our initial conditions in the stratified box setup. The upper plots show a vertical slice through the center and the lower ones through the midplane and the quantities are color coded. The first panel shows the initial density profile following equation (3.1). The second panels show the total magnetic field strength that is linked to the density according to equation (3.17). In the third panel the fraction of CR pressure and thermal pressure is plotted, that is zero at the beginning as we do not include CRs in the initial conditions. The last panels (right) show of the temperature of the box.
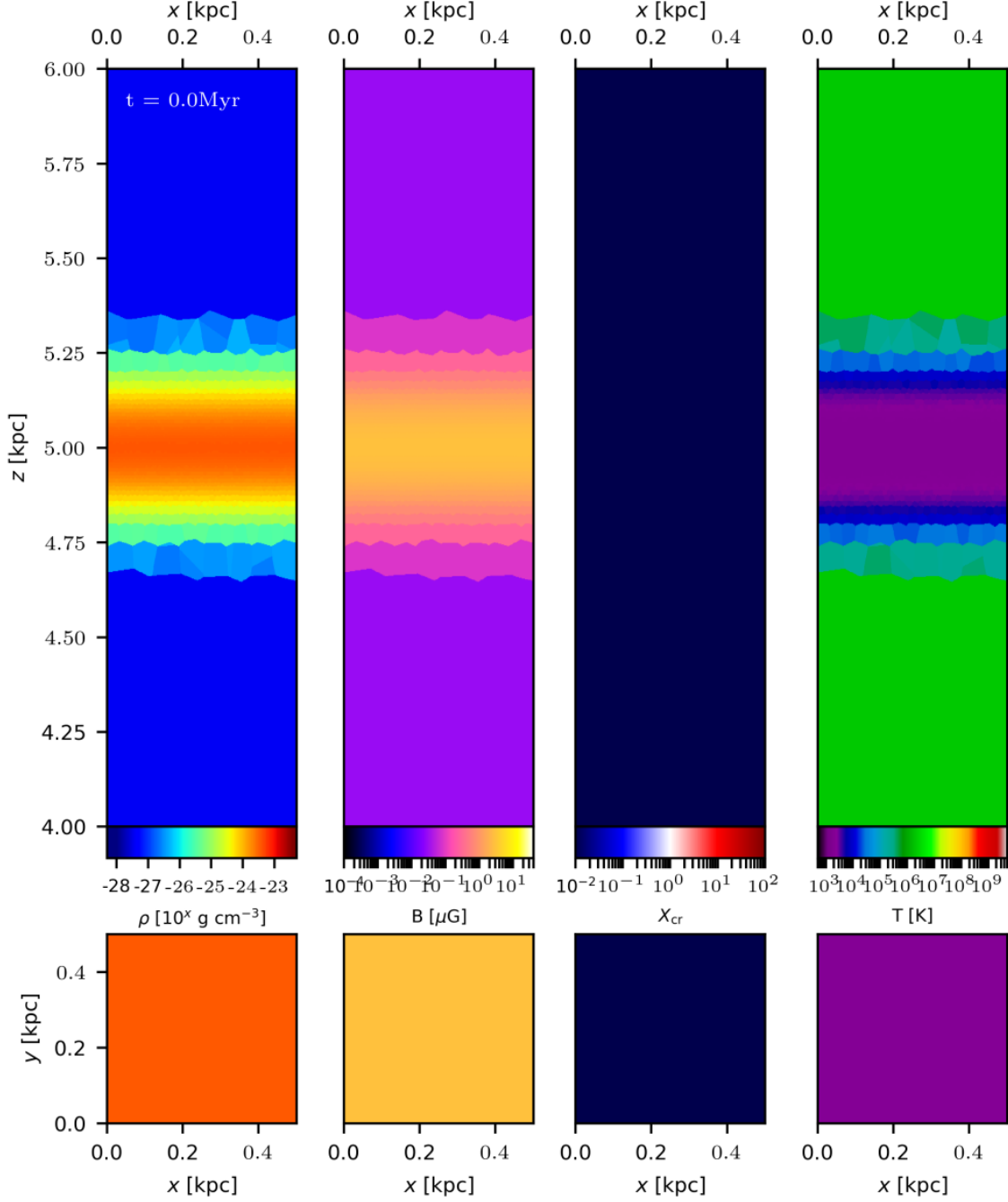
Figure 4.3: Illustration of a vertical and horizontal slice through the center of the box at t = 0 Myr, which is the same for all our simulations. From left to right we plot density, magnetic field strength, the ratio of cosmic ray to thermal pressure X_{cr} and the temperature.
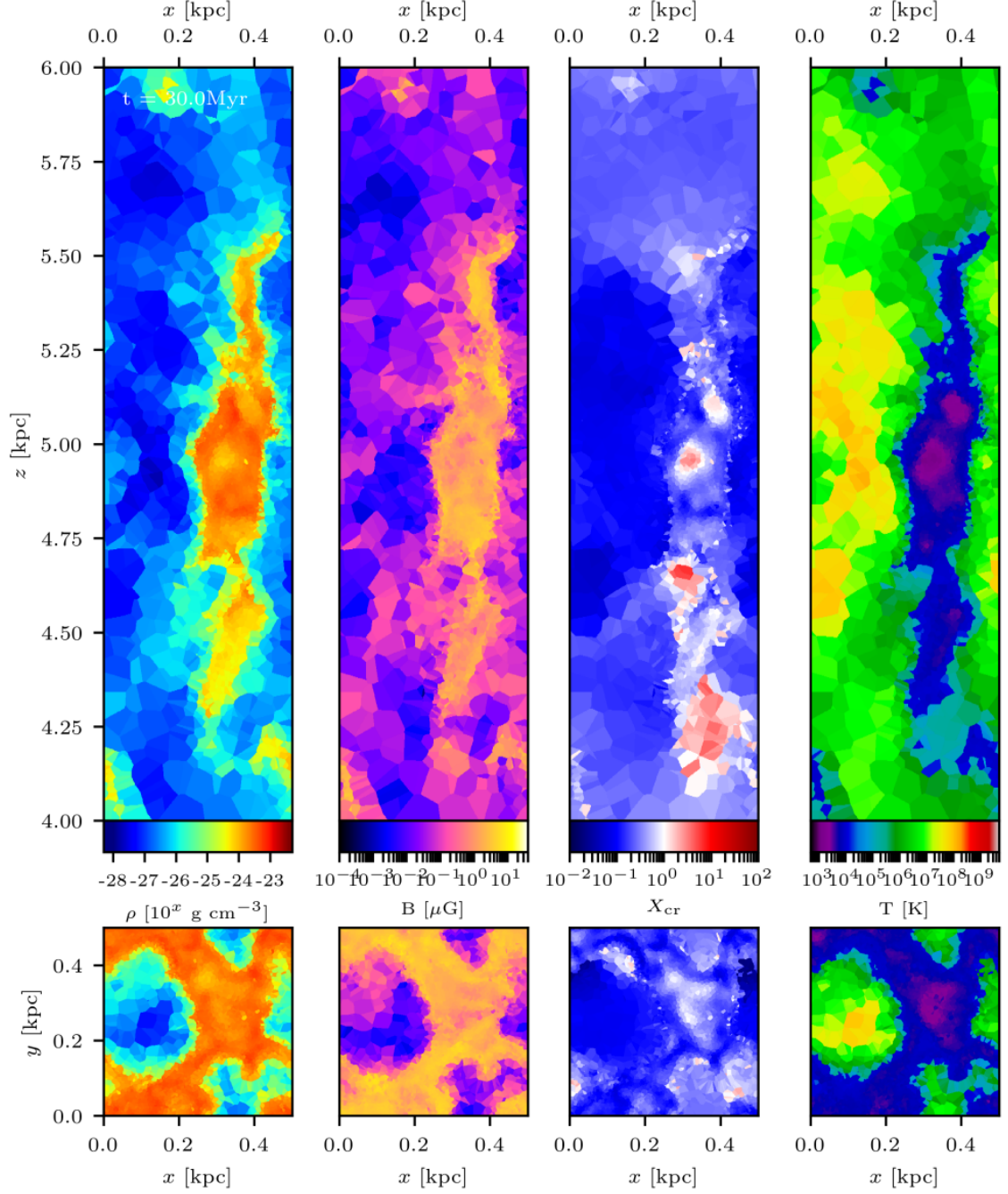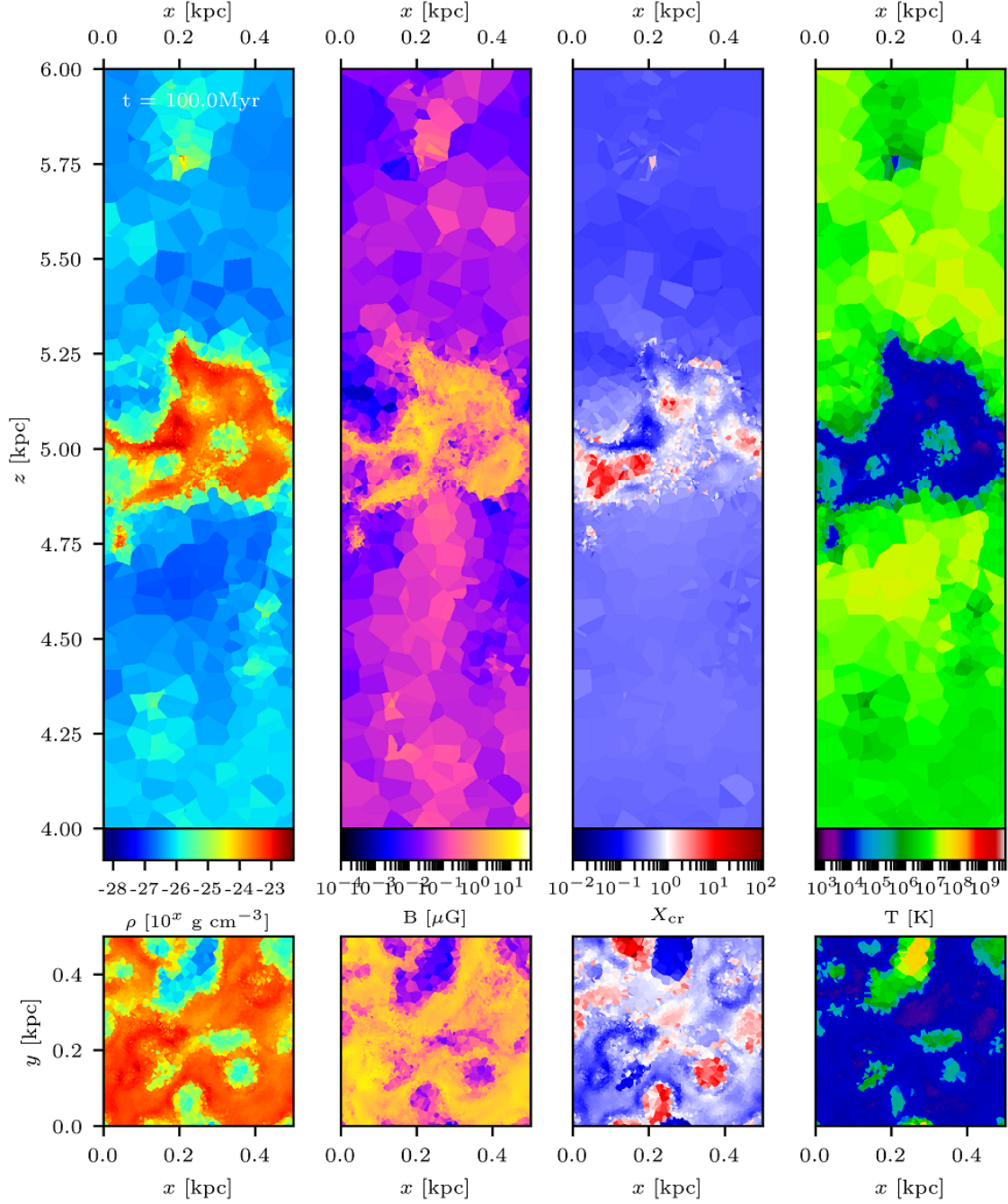
Figure 4.4: Illustration of a vertical and horizontal slice through the center of the box at t = 30 Myr, which is the same for all our simulations. From left to right we plot density, magnetic field strength, the ratio of cosmic ray to thermal pressure X_{cr} and the temperature.

Figure 4.5: Illustration of a vertical and horizontal slice through the center of the box at t = 100 Myr, which is the same for all our simulations. From left to right we plot density, magnetic field strength, the ratio of cosmic ray to thermal pressure X_{cr} and the temperature.
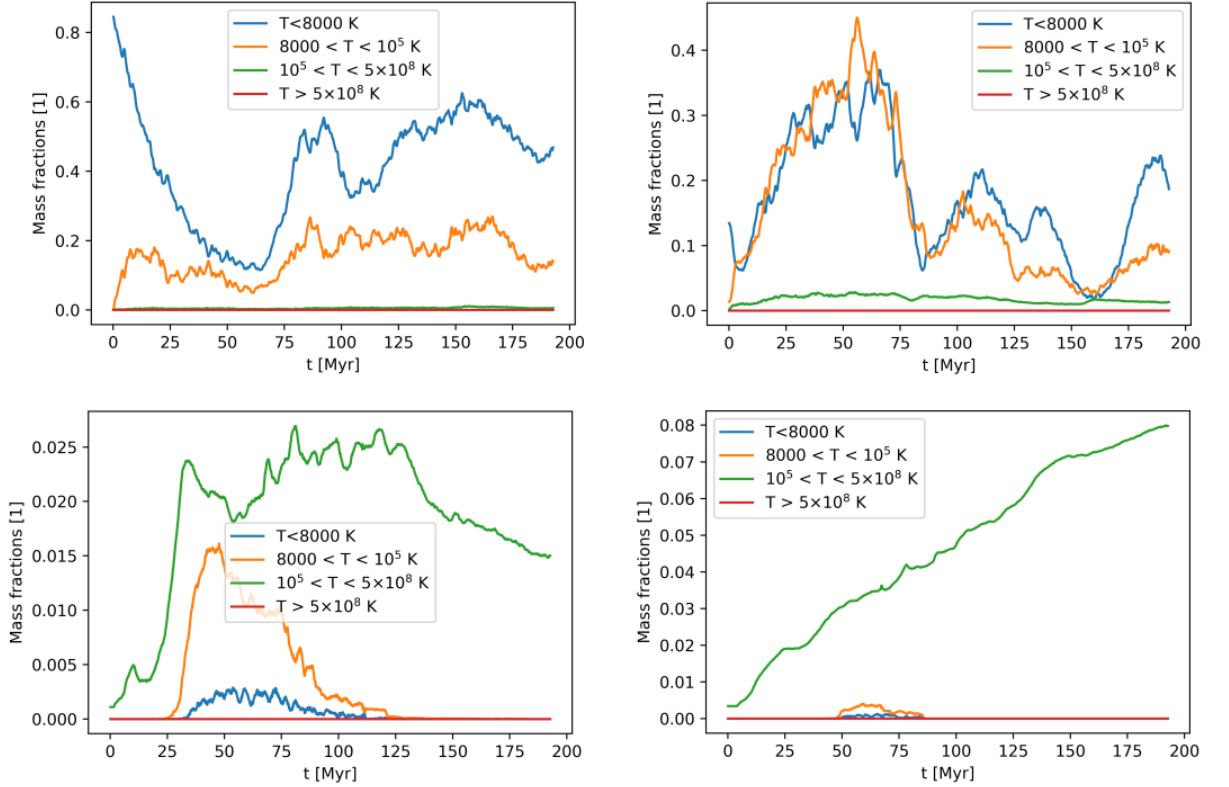
Figure 4.6: Total mass fractions of different gas temperatures over time for different box regions of simulation INJ04. (top left): disk region $|z-z_{\mathrm{mid}}| < 100\,\mathrm{pc}$, (top right): $100\,\mathrm{pc} < |z-z_{\mathrm{mid}}| < 1.0\,\mathrm{kpc}$, (bottom left): $1.0\,\mathrm{kpc} < |z-z_{\mathrm{mid}}| < 2.0\,\mathrm{kpc}$, (bottom right): $|z-z_{\mathrm{mid}}| > 2.0\,\mathrm{kpc}$.

4.3 ISM structure and phases

4.3.1 Gas distribution

The vertical gas distribution is complex to analyze and hence we focus on qualitative conclusion drawn from the local and overall gas distributions. One part that allows to investigate the gas distribution and evolution are the mass and volume fractions of different gas temperature regimes. We analyze them in different regions: the disk region which is 100 pc above and below the midplane $|z - z_{\mathrm{mid}}| < 100\,\mathrm{pc}$, the inner region between the disk and 1 kpc distance from the midplane ($100\,\mathrm{pc} < |z - z_{\mathrm{mid}}| < 1.0\,\mathrm{kpc}$), the middle region above 1 kpc and below 2 kpc ($1.0\,\mathrm{kpc} < |z - z_{\mathrm{mid}}| < 2.0\,\mathrm{kpc}$) and the outer region above 2 kpc ($|z - z_{\mathrm{mid}}| > 2.0\,\mathrm{kpc}$). Within these regions we define different temperature ranges, cold gas with $T < 8000\,\mathrm{K}$ (blue), warm gas within $8000\,\mathrm{K} < T < 10^5\,\mathrm{K}$ (orange), hot gas within $10^5\,\mathrm{K} < T < 5 \times 10^8\,\mathrm{K}$ (green) and gas with $T > 5 \times 10^8\,\mathrm{K}$ (red). We note that the highest temperature regime is primarily chosen as a numerical check rather than a physically motivated regime.
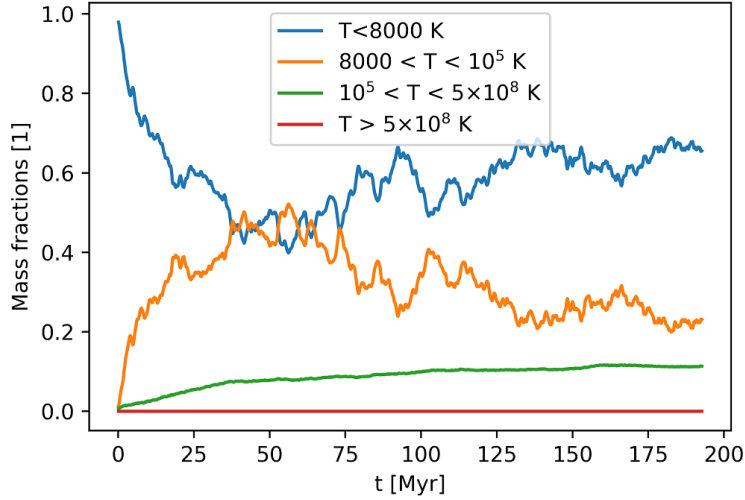
Figure 4.7: Time evolution of the total mass fractions within the entire box. Different temperature regimes are color coded.

Figure 4.6 shows the mass fractions of the different temperature regions within the disk (top left panel), inner part (top right panel), middle part (bottom left panel) and outer parts (bottom right panel) and Figure 4.7 shows it for the entire box. These values correspond to the run of INJ04, however they are very similar in their shapes and have comparable values for all the runs 4.8. Thus we focus on the differences and implications drawn from them.

At the beginning the SNe within the disk drive the gas outwards resulting in a decrease in the cold gas fraction within the disk (top left panel of 4.6) and an increase in the inner regions (top right panel 4.6). The warm gas fraction increases and reaches a smaller but a more stable fraction within the disk. At around 60 Myr both the cold and warm gas reach a minimum value inside the disk, in which their fractions are almost equal. After that both increase again and peak at around 85 Myr as the gas starts falling back onto the disk. Again after that peak the warm gas fraction stabilizes at around 0.2 of the total mass. The cold gas fraction drops and slowly increases again up to 0.6. This implies that after 100 Myr cold gas is mainly located in the disk region, where each SN has a smaller impact on it and thus reduces the cycling of the gas between the disk and the inner parts above and below. The fraction of hot gas does not contribute noticeably inside the disk, as only a small part starts rising at 100 Myr until reaching about 1% at 150 Myr.

Inside the inner region (top right 4.6) the fraction of warm and cold gas share a similar shape in their time evolution. They steeply increase at the beginning, as a larger fraction of cold gas gets pushed away from the disk and the thermal energy released by the SNe distributes over the local volume. After the steep increase the cold and warm gas peak around 55 Myr and 60 Myr respectively, with the warm gas reaching larger fractions $\sim$ 0.45 than the cold gas $\sim$ 0.38. Their initial evolution is also slightly complementary in which the fraction of either increases whereas the fraction of the other decreases (see peak
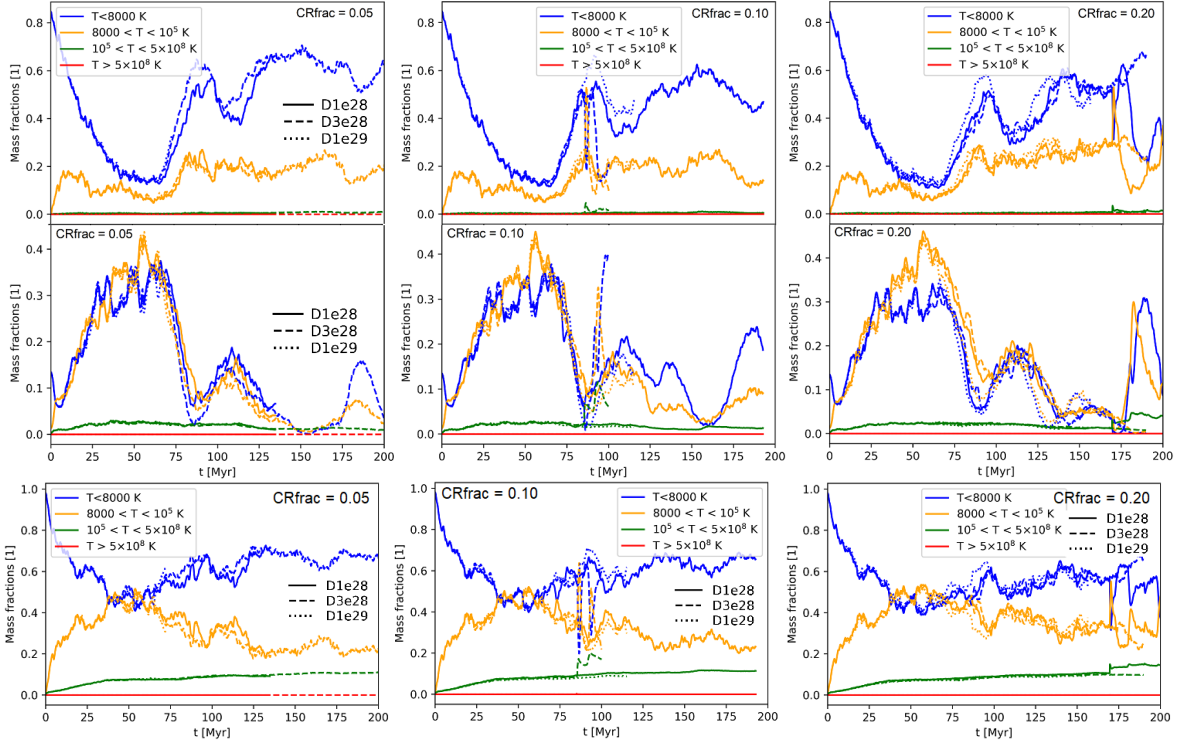
Figure 4.8: Comparison of the mass fractions of all INJ runs. Top down we show the disk region, the inner region and the total box. Different temperature regimes are color coded, the CR fractions increase from left to right and the corresponding diffusion coefficient is given by the line style.

of warm gas and dip of cold gas around 55 Myr). Later gas falls back into the disk region, thus decreasing both cold and warm gas fractions almost equally to a minimum at around 85 Myr. The gas cycles further between the disk and the inner part as both de- and increase again. Inside the inner part there is a small but stable fraction of hot gas that contributes to ∼ 4% of the total gas mas.

The middle region (bottom left panel 4.6) is mostly filled by hot gas. Its fraction steeply increases up to ∼ 2% and remains at around that value. After 30 Myr warm and slightly later warm and cold gas are pushed up in that region. The warm gas shares a steep increase similar to the hot gas, peaks at 40 Myr at 1.5% and decays over time until 125 Myr. The cold part remains more stable at ∼ 0.25% but also drops again.

Far outside the galactic disk, in the outer region (bottom right panel 4.6), the hot gas increases alternatingly with plateau phases, at which the fraction remains roughly constant over a short time span. It continues until the mass fraction of hot gas reaches about 8% at the end of the run, which indicates an almost constant flow of hot gas away from the disk and the inner regions. A detailed analysis of outflows is carried out in 4.4. There are smaller amounts of cold and warm gas that are driven out here between 50 Myr and 80 Myr, which is not the case for all runs.
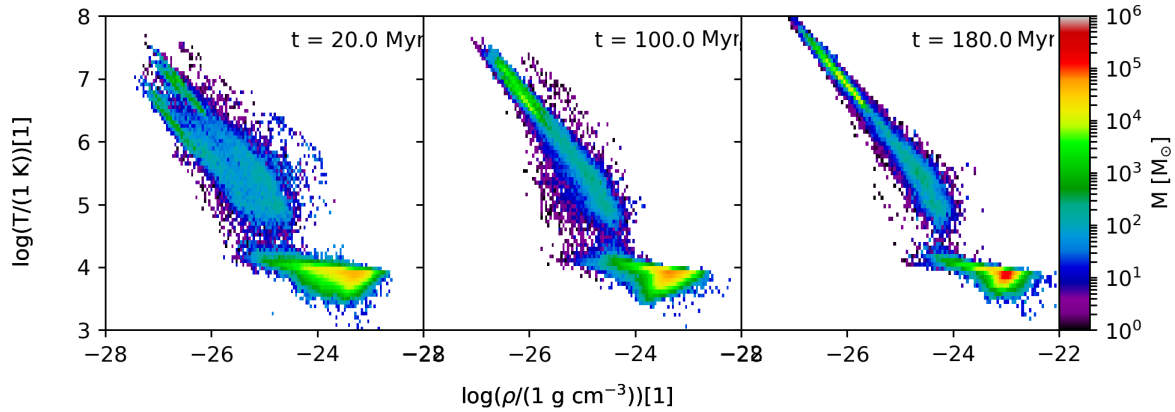
Figure 4.9: Time evolution of mass weighted 2D histogram of the gas temperature and density for run INJ04.

Figure 4.7 shows the evolution of the mass fractions of the entire box. With the thermal energy input form the SNe the cold gas fraction decreases until it reaches almost equal values of the rising warm gas at 60 Myr. Afterwards the fraction of warm gas shows a decreasing trend, where as the cold gas slightly increases. The hot gas increases constantly with a larger slope in the first 40 Myr that then flattens and remains roughly constant.

Inside the disk region there are minor differences between the different runs but the overall evolution is similar. Some runs contain larger discrepancies but we can not conclude it as a systematic effect of the different diffusion or CR fraction. However there is a pattern for the gas of the entire box, as the gap between the cold and warm gas fraction gets smaller after reaching roughly equal values, for larger CR fractions. Within the middle region the warm gas fraction slightly increases with larger CR fraction. Nevertheless the run INJ09 shows one of the smallest warm and cold gas fractions. In the inner part the runs with larger CR fraction show a clear separation of the warm gas from the cold gas at early times and less separation in the later stages, the values are almost equal. The runs with less CRs show a smaller gap between warm and cold gas at early times and a larger at later times (Figure 4.6 top right panel). In the outer parts the hot gas in all simulations rise to a similar value of 8%. The runs INJ03, INJ04, INJ08 and INJ09 show warm and cold gas fractions but they occupy very small values $\sim$ 0.2-0.4%. There seems to be no difference in the hot gas and no pattern for the cold and warm gas.

The correlation between temperature and density is given by the 2D histograms in Figure 4.9. These are mass weighted histograms of INJ04 run at different time stamps. The evolution shows an initial mass peak for cold gas $\sim 10^4$ K at high densities $\sim 10^{-23.5}$ g cm^{-3}, that remains over time but a second mass peak evolves after ~ 60 Myr. This second peak acquires more mass and involves gas within the temperature range of 10^6-10^8 K and densities from $10^{-25.5}$-10^{-27} g cm^{-3}. All runs share a comparable relation of temperature and density and there are no noticeable effects of these minor differences. This similarity
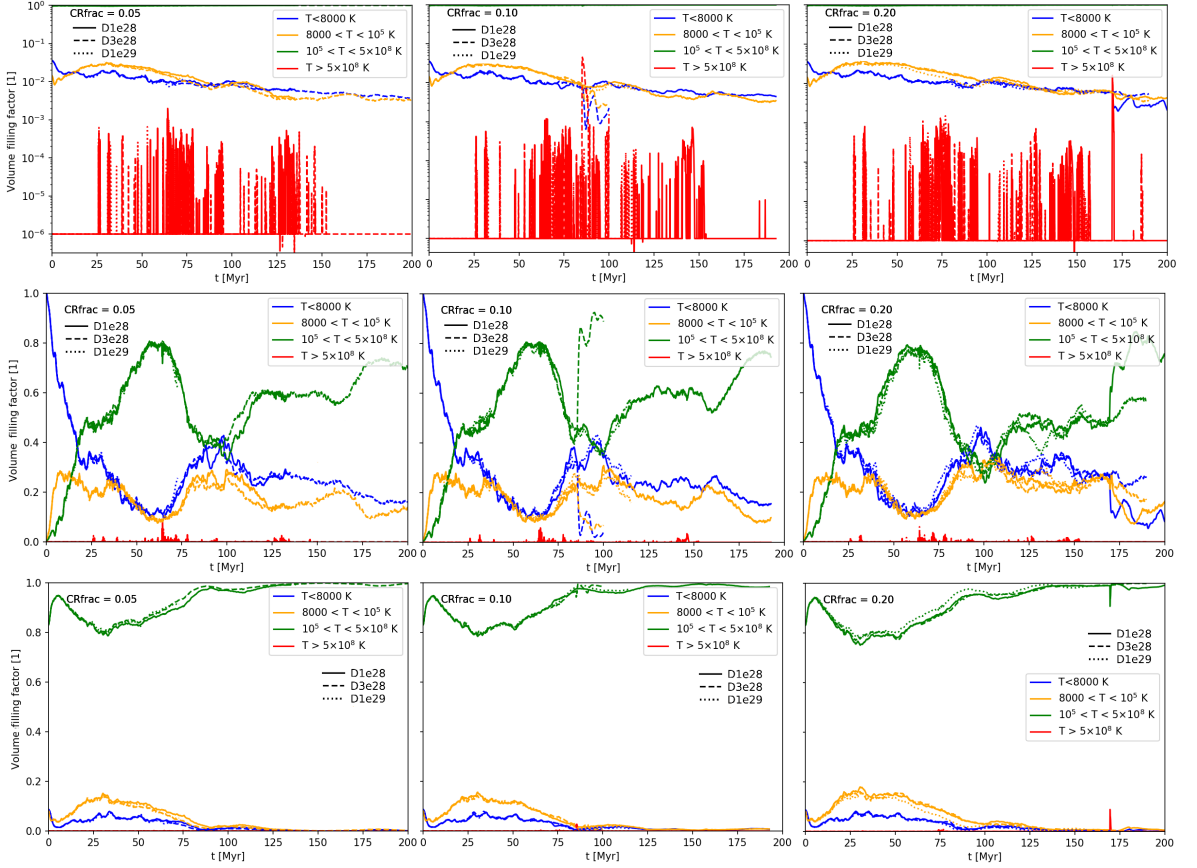
Figure 4.10: Evolution of the volume filling factors inside the entire box (top row), the disk region (central row) and inner region (bottom row). From left to right the panels show an increasing CR injection fraction. The different line styles define the corresponding diffusion coefficient.

likely means that the gas occupies equilibrium phases, which is then given by the cooling function.

When we look at the volume filling factors (VFFs) of the same temperature regimes, shown in Figure 4.10, we find all regions to be mostly filled with hot gas (green). The top row shows the VFFs inside the entire box, the central row inside the disk region and the bottom row inside inner regions. From left to right we show increasing CR injection fractions and the line styles represent different diffusion coefficients, increasing with along with solid, dashed and dotted line styles. They are measured with respect to their environment. The middle and outer region are almost fully filled by hot gas only and therefore are not included in Figure 4.10.

We find the different VFFs to be quasi identical for all runs. In the entire box (top row) the hot gas fills up almost the entire volume over the simulation time. The warm gas increase at early times and reaches a maximum value around 3% before it steadily decreases. The cold gas fraction decreases over the simulation below 1%. There are several spikes in gas
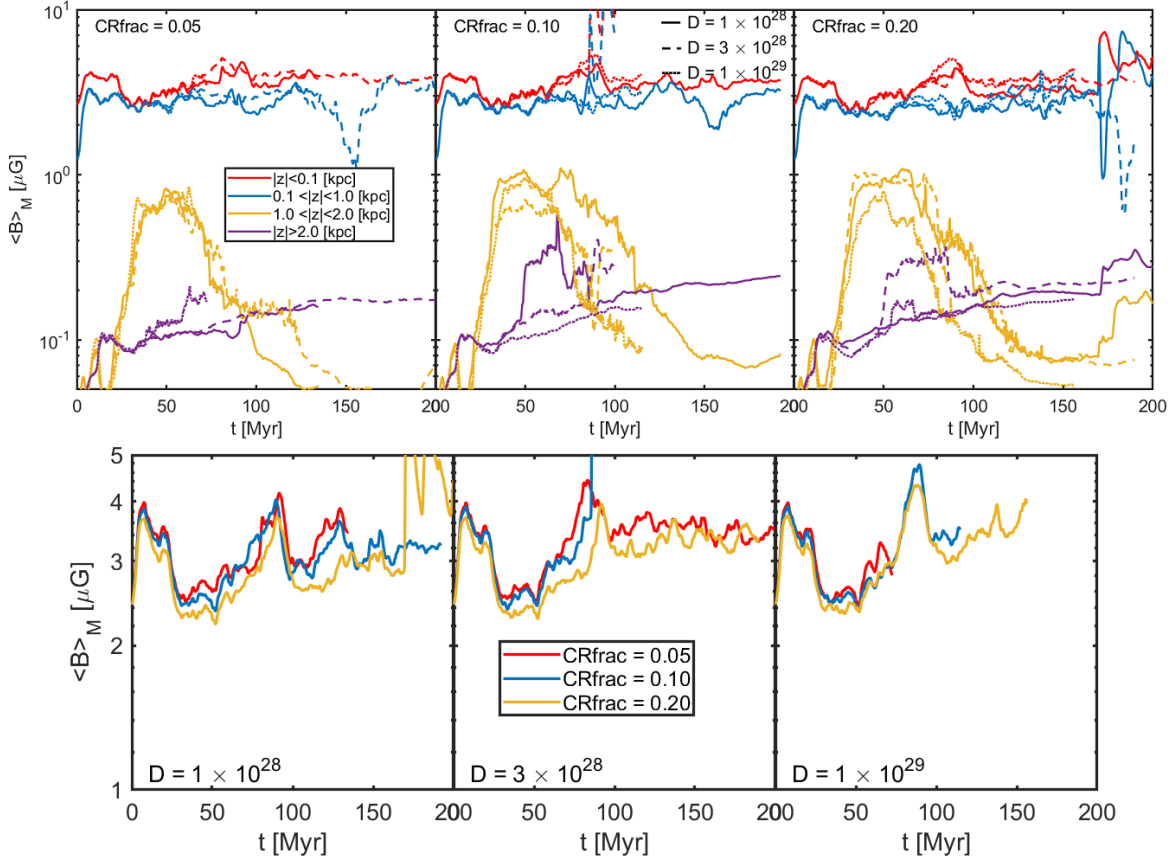
Figure 4.11: Mass weighted mean value of the magnetic field strength within different box regions (color coded in the top row) and for the entire box (bottom row). The top panels show different CR injection fractions, increasing from left to right and different diffusion coefficients are illustrated by different line styles. The bottom panels involve runs with an equal diffusion coefficient increasing from left to right.

with $T > 5 \times 10^8$ K resulting from SN clusters, however their fraction is negligible.

4.3.2 Magnetic field evolution

For all our runs we find a comparable evolution of the magnetic field strengths and their mean values, see Figure 4.11. In the top row we show the time evolution of the mass weighted mean values of the magnetic field strength, which is calculated by $\langle B \rangle_M = \frac{\sum_{i=1}^{N} M_i B_i}{\sum_{i=1}^{N} M_i}$, within different box regions given by the color coding. The panels show different CR injection fractions, increasing from left to right, and the corresponding diffusion coefficient are indicated by the line style. The bottom row illustrated the mass weighted mean values of the magnetic field strength for the entire box. The panels involve the runs with equal diffusion coefficients and the colors encode the different CR injection fraction. Inside the top row, the red color encodes the disk, blue the inner, yellow the middle and
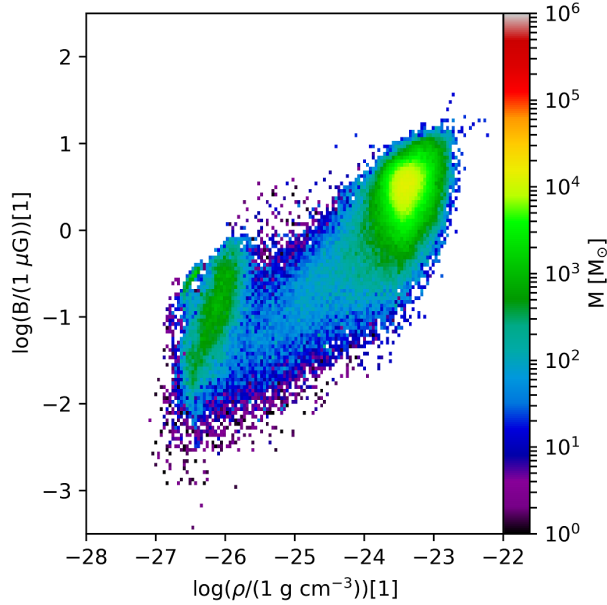
Figure 4.12: Mass weighted 2D histogram of the magnetic field strength and density at 100 Myr for the INJ04 run.

purple the outer regions. The diffusion coefficients are given by the line style solid for $D = 10^{28}\,\mathrm{cm^2\,s^{-1}}$, dashed for $D = 3 \times 10^{28}\,\mathrm{cm^2\,s^{-1}}$ and dotted for $D = 10^{29}\,\mathrm{cm^2\,s^{-1}}$. Within the disk region our simulations yield time stable average magnetic field strengths of ~ 3-$4\,\mu$G, which is comparable to the initial magnetic field. The inner regions show a steeper increase to $\sim 3\,\mu$G and remain a stable value of ~ 2.5-$3\,\mu$G. The middle regions shows a steep increase to ~ 0.6-$1\,\mu$G at $\sim 35\,$Myr and remain at similar values for $\sim 50\,$Myr before decreasing again. Within the outer regions the magnetic field strength shows a continuous increase after an initial peak at $0.1\,\mu$G at $\sim 15\,$Myr.

The reached values indicate the diffusion coefficient to have a minor impact on the overall magnetic field evolution, as the runs with larger diffusion coefficient reach slightly larger values (bottom panels). However there are non systematic differences in form of steep increases in the value within the outer regions (purple lines) and a longer remain of higher values in the middle region (yellow). These can be explained by small amounts of cold and warm gas reaching the outer regions (bottom right panel of Figure 4.6) which contain a stronger magnetic fields and higher densities.

For the entire box (bottom panels) we find the CR injection fraction to slightly vary the magnetic field strength. For all diffusion coefficients we find the low CR injection runs (red) to reach only slightly higher values than high CR injection, which can be explained by the stronger coupling of thermal/kinetic feedback to the magnetic field. The average magnetic field strength steeply increases from $2.3\,\mu$G to $\sim 4\,\mu$G within the first 15 Myr and drops after the first 2 peaks down to $\sim 2.2\,\mu$G at 60 Myr. After the minimum the value steadily increases, peaking $\sim 85\,$Myr with a slightly larger value than the initial peak. Afterwards it drops down and remains more stable between ~ 2.5-$4\,\mu$G.

Additionally we find a very comparable evolution for all runs in the coupling of the magnetic field to the gas, shown in the mass weighted 2D histogram of the magnetic field strength and the density in Figure 4.12. There are two regions in all histograms that contain the largest mass fraction. One is centered at high density $\sim 10^{-23.5}\,\mathrm{g\ cm^{-3}}$ with a magnetic field strength of a few μG, represented by the yellow spot in each of the nine histograms. This peak is explained by the magnetic field being bound to the gas which is centered in the disk plane where the gas is compressed by gravity.

The second region is located at $\rho \sim 10^{-26.5}\,\mathrm{g\ cm^{-3}}$ and $B \sim 10^{-1}\,\mu G$, whilst the surrounding and connecting regions contain only small amounts of mass. Outflows (see section 4.4 drag the magnetic field with them, thus leading to a second mass peak but with only small magnetic field strength.

4.3.3 Cosmic ray scale height

We investigate the distribution of CRs in our box by their scale heights. We select the CR scale height as the vertical distance to the midplane at which the integrated CR energy reaches 70% of the total CR energy. This corresponds to a one sigma deviation of Gaussian distribution $\sim 68\%$.

Figure 4.13 shows the CR scale heights of all our runs. The black colored lines indicate the runs with 5%, blue with 10% and red with 20% CR injection fraction. Respectively the dashed lines correspond to the runs with a diffusion coefficient of $D = 10^{28}\ \mathrm{cm^2\,s^{-1}}$, the solid lines to the runs with $D = 3 \times 10^{28}\ \mathrm{cm^2\,s^{-1}}$ and the dashed dotted lines to the runs with $D = 10^{29}\ \mathrm{cm^2\,s^{-1}}$. Starting from the initial conditions without CRs, all simulations show a steep increase in their CR scale height until $\sim 20\,\mathrm{Myr}$. After that the scale height steeply drops to a certain value depending on the diffusion coefficient. However the total drop is of different strength for different diffusion coefficients. The larger the diffusion coefficient, the smaller the total drop. After the drop at $t \sim 30\,\mathrm{Myr}$ all scale heights show a moderate increase from which all start to grow until they reach an almost constant value at $t \sim 160\,\mathrm{Myr}$. This value is similar for all runs at $z \sim 3.25\,\mathrm{kpc}$ for a diffusion coefficient of $D = 10^{28}\ \mathrm{cm^2\,s^{-1}}$ and $z \sim 3.4\,\mathrm{kpc}$ for the other two.

Considering the overall evolution we see that the CR scale height at the beginning is mainly determined by the chosen diffusion coefficient and not, or only minimally, influenced by the injected CR fraction in the SNe.

4.3.4 Distribution of cosmic ray and thermal pressure

To investigate the energy densities of CRs locally we calculate the volume weighted average values of X_{CR} with

$$X_{\mathrm{CR}} = \frac{P_{\mathrm{CR}}}{P_{\mathrm{th}}} \tag{4.1}$$

in different regions inside the box. Figure 4.14 shows the volume weighted average values of X_{CR} for all simulations with an increasing CR injection fraction from bottom to top. The columns show runs with an equal diffusion coefficient increasing from left to right.
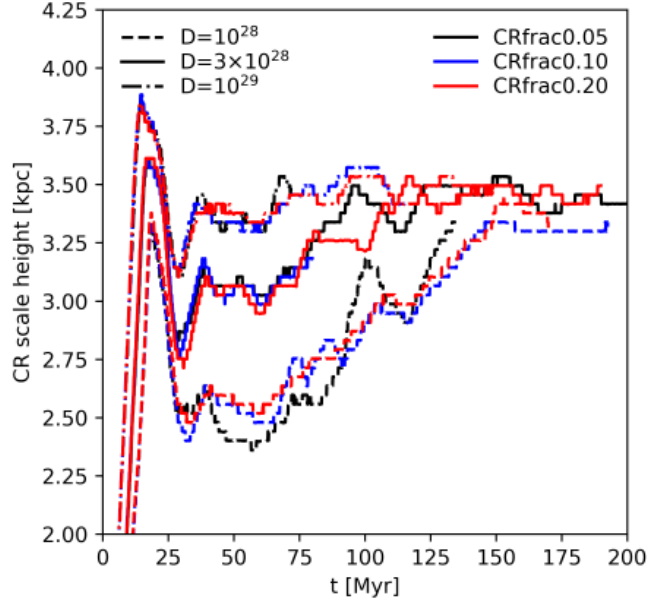
Figure 4.13: All CR scale heights as function of time. The black line colors indicates the simulations with CR injection fraction of 5%, blue of 10% and red of 20%. The dashed lines represent the runs with diffusion coefficient of 10^{28}, the solid lines the runs with 3×10^{28} and the dashed dotted lines are the runs of 10^{29} $\mathrm{cm^2\,s^{-1}}$

Different box regions are shown by different line colors. To reduce fluctuations in the average values, we further average those over five consecutive values. The shape of the volume averages of X_{CR} is comparable for all runs and except for the outer regions we find stable values inside the disk, inner and middle region, that neither show an increasing or decreasing trend.

Within the outer (purple) region the X_{CR} first steeply increases and reaches a small plateau after which the values slightly drop and increases slightly over time. The middle region (yellow) also shows a steep increase in X_{CR} at early times and then peaks at $\sim 30\,\mathrm{Myr}$, after which it slightly decreases. It reaches very comparable values to the outer region. In both the outer and mid region the increase of X_{CR} takes time, as it takes time for turbulence to restructure the magnetic field lines, such that the CRs can diffuse outwards from the inner regions (Simpson et al., 2016). Inside the inner part (blue) the ratio of CR to thermal pressure increases, to e.g. ~ 0.8-1.0 for the 20% CR injection runs, and remains an almost constant value before it slowly decreases to reach comparable values to the outer and middle regions ~ 0.2. Within the disk (red) the X_{CR} value increases and decreases afterwards, where it is smaller than in the inner and middle region. Afterwards it increases again and exceeding the inner region values and remains more stable.

Different diffusion coefficients have a small but noticeable impact on the evolution of X_{CR}. A larger diffusion coefficient results in larger values of X_{CR} in the outer regions (purple) at early times. Nevertheless lower values for smaller diffusion coefficients reach a comparable values, within a factor of 2, at later times depending on the CR injection fraction, e.g.
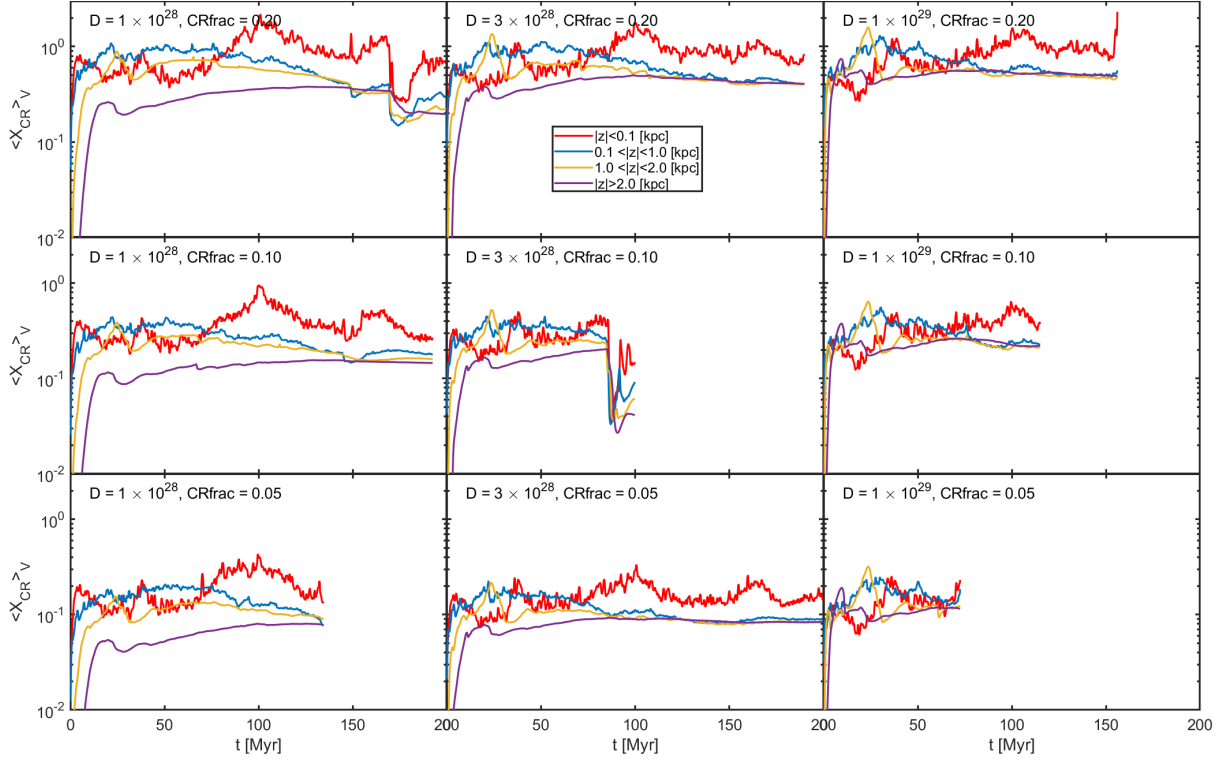
Figure 4.14: Time evolution of the volume weighted mean values of X_{CR} for different CR fractions and diffusion coefficients. The columns contain the runs with equal diffusion coefficient and the rows the ones with equal CR injection fraction. The colors indicate different box regions.

~ 0.4 for the runs with 20% CR injection fraction (top row).

Inside the disk and middle region a larger diffusion coefficient results in overall slightly smaller and higher values. Larger diffusion coefficients lead to a stronger peak within the middle region and a smaller compensating low in the disk region at $\sim 30\,\mathrm{Myr}$.

The inner region seems to be only minorly effected by the diffusion coefficients. Overall the inner, middle and outer regions later contain an equal ratio of CR to thermal pressure. The larger the diffusion coefficient the earlier this equal ratio is reached.

Different CR injection fractions only result in minor shape differences of the X_{CR} evolution. The values increase by a factor of ~ 2, comparing 5% to 10% and 10% to 20% CR injection fraction. In case of only 5% CR injection (bottom row) the thermal pressure becomes more dominant as it varies between $\sim$2-10, within the disk, and $\sim$5-20, in the other regions, times the CR pressure. For a CR injection fraction of 20% the ratio of CR to thermal pressure varies between ~ 0.3-2 inside the disk and 0.2-1.0 at early times in the other regions. At late times the thermal pressure dominates all other regions with $X_{CR} \sim 0.2$.

Comparing our values for all runs to previous studies (Girichidis et al., 2018a), we find them to be significantly smaller. This can be explained by our cooling model, as we are only able to cool down to few1000 K efficiently. The inclusion of further cooling, down to
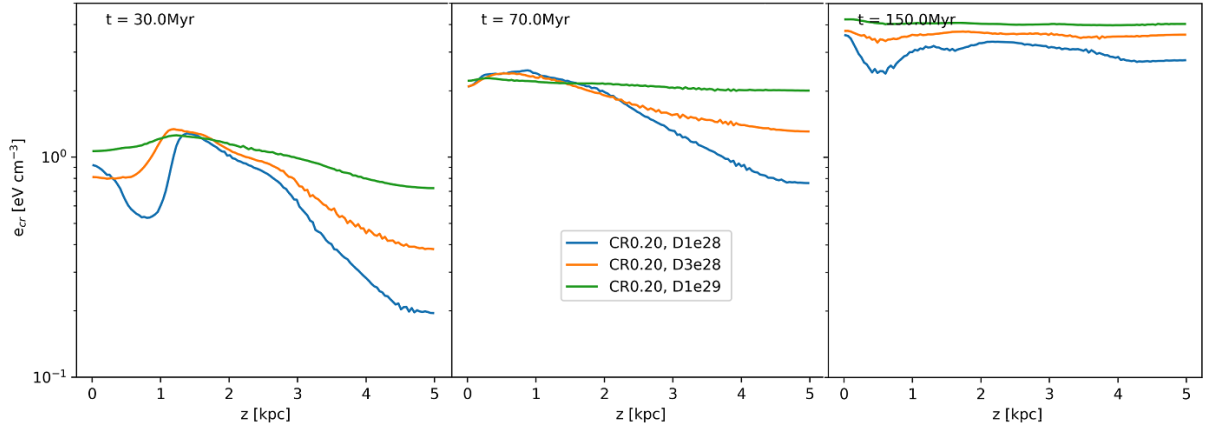
Figure 4.15: Volume weighted CR energy distribution of runs with 20% CR injection fraction at 30 Myr (left), 70 Myr (central) and 150 Myr (right).

few100 K, would be likely to increase the X_{CR} by at least one order of magnitude and lead to more comparable values.

4.3.5 Cosmic ray energy distribution

In the CR energy we find similar behavior over time for all CR injection fraction that only differs by the values reached. Larger diffusion coefficients lead to an faster expansion into the outer regions and hence larger e_{CR} values at early evolution stages (left panel Figure 4.15). This trend remains for all later times but the differences becomes minor over time (central and right panel 4.15). Thus all runs of the same CR injection fractions end up reaching very comparable values in their CR energy density. Hence when compared to observations it is difficult to constrain the diffusion coefficient. The runs with 5% CR injection reach values of $\sim$0.9-1.2 eV cm^{-3}, the 10% runs $\sim$ 2-2.5 eV cm^{-3} and the 20% runs $\sim$ 3-4 eV cm^{-3} at times larger than 150 Myr.

The upper row of Figure 4.16 shows the CR energies, indicated by the green line, over time. The left panel illustrates the runs with 5%, the central one the runs with 10% and the right one the runs with 20% CR injection fraction. The theoretical CR energy input is shown by the red line. In all three images the smaller diffusion coefficients $D = 1 \times 10^{28}$ cm^2 s^{-1} (solid green) and $D = 3 \times 10^{28}$ cm^2 s^{-1} (dashed green) are slightly underneath the theoretical energy input. However the runs with $D = 1 \times 10^{29}$ cm^2 s^{-1} (dotted green) show a higher CR energy than the theoretical input. This might be explained by the relatively high diffusion coefficient. When CRs advance slowly, given by a small diffusion coefficient, there are local points of higher CR presence. Thus the locally increased CR amount leads to an increased interaction probability with the by SNe accelerated gas. This explains the slight deficit in CR energy other than the cooling. If they advance fast, such that the local CR amount decreases significantly before accelerated gas reaches that region, the interaction probability is smaller, which results in less energy loss. Further a compression of the local gas (which contains only a small amount of CR energy) can lead to an increased net
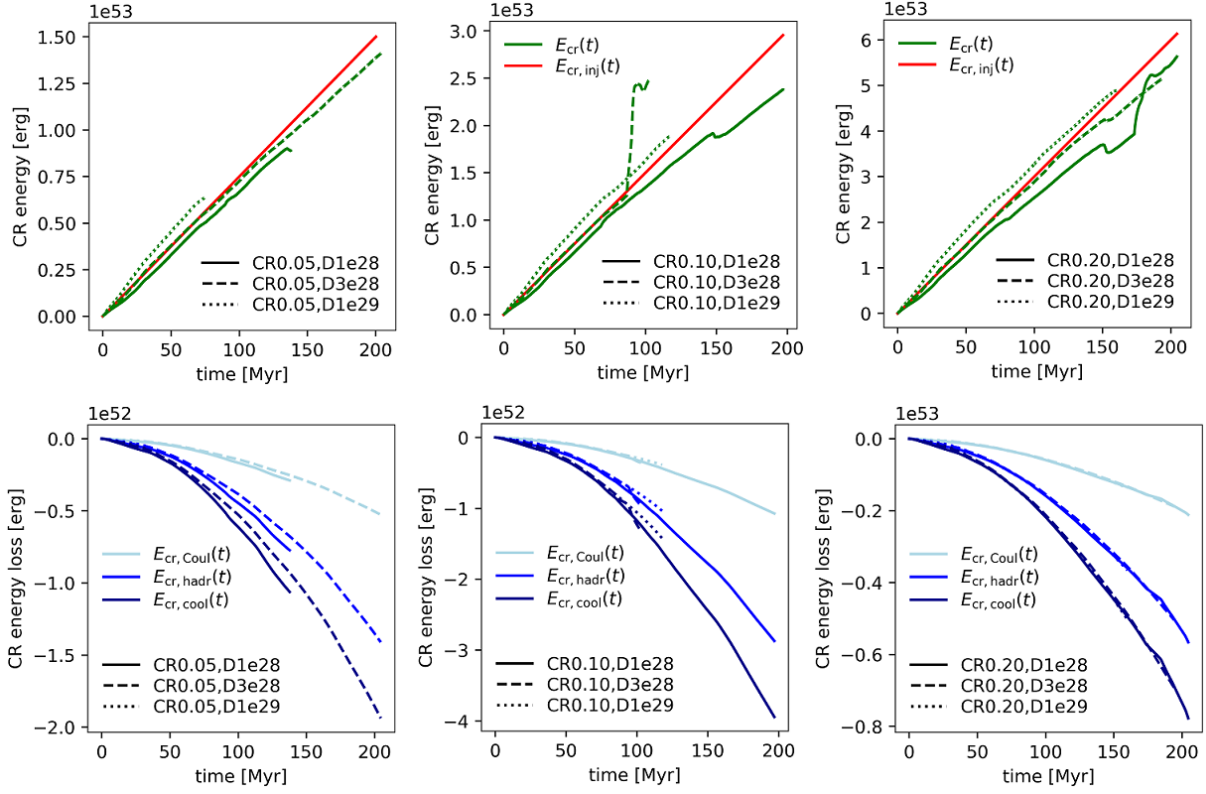
Figure 4.16: CR energy (top row) and energy losses (bottom row) over time. (left column) shows it for 5%, (central column): 10% and (right column): 20% CR injection fraction.
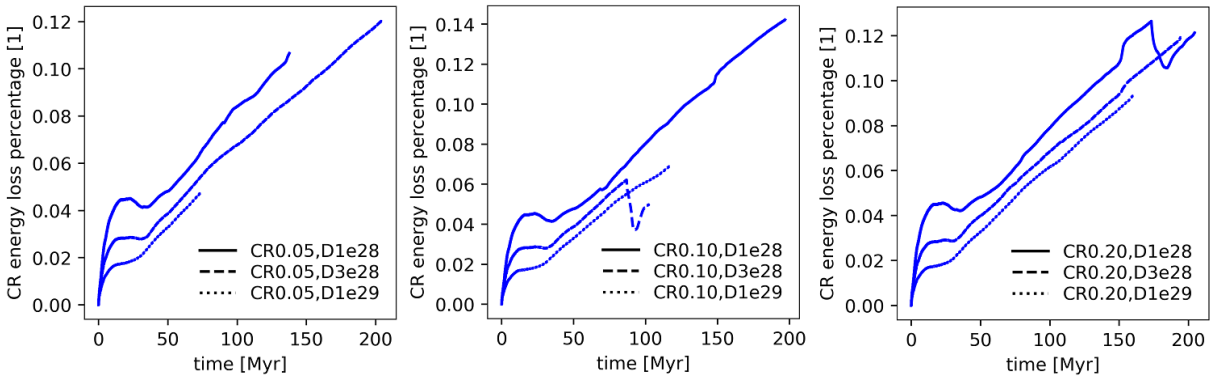

Figure 4.17: Summed up CR energy loss percentage of CR cooling (hadronic and Coulomb cooling), over time. From left to right we increasingly plot the different CR injection fractions (5, 10, 20%).

transfers of kinetic energy to the present CRs. That process can lead to a net CR energy gain, thus increasing the CR energy over the theoretical input.

The lower row of Figure 4.16 shows the CR energy losses by Coulomb interactions (light blue), by hadronic losses (blue) and their sum as total CR cooling (dark blue), with the same splitting as above. In case of the runs with 20% (right panel) CR fraction runs the energy losses are the same for the different diffusion coefficients. For the 10% runs (central panel) only the lowest diffusion coefficient (solid line) shows slightly more significant losses than the larger ones (they are the same). This trends continues for the low CR fraction runs (left panel) as the solid line now clearly separates from the overlaying dashed and dotted lines.

The energy losses can be explained by the transport of CRs. With 5% CR fraction (left panel) there is only a small amount of CRs injected that can loose energy. With a small diffusion coefficient they are more strongly bound the local gas which leads to a larger interaction rate. Thus with a small diffusion coefficient they loose more energy. With higher diffusion coefficients the local CRs escape before interacting, hence reducing the loss. At larger CR injection fractions (central, right panel) the total CR energy loss increases linearly with the fraction. Additionally the diffusion coefficient only minorly impacts the CR energy loss, as the overall interaction probability strongly increases with the overall CR amount. Therefore the separation between small and larger diffusion coefficient becomes less clear (central) and negligible in the right panel.

Nevertheless, for all runs the total energy loss percentage, by CR cooling, namely hadronic and Coulomb cooling, evolves equally with a separation between the different diffusion coefficients, see Figure 4.17. Overall the runs with the smallest diffusion coefficient show the largest losses in terms of percentage of the total CR energy. The runs with larger diffusion coefficient show a comparable shape over time but with 0.5-2% less total loss. Larger CR injection fractions do not influence the percentage of total losses significantly. However the same total loss percentages are reached slightly earlier, which can be explained by more CR being present, which supports a higher interaction rate.

4.4 Outflows and massloading

We investigate outflows driven in our simulations by the mass transported away from the galactic disk. We select a reference scale height of 1 kpc above and below the midplane and compare the masses above and below to estimate the outflowing mass. We further average over five snapshots to reduce the impact of local fluctuations at the chosen outflow boundary. The panels of Figure 4.18 shows the mass loading factors for different CR injection fractions, increasing from left to right. The blue lines correspond to a diffusion coefficient of $D = 10^{28} \, \text{cm}^2 \, \text{s}^{-1}$, red orange to $D = 3 \times 10^{29} \, \text{cm}^2 \, \text{s}^{-1}$ and green to $D = 10^{29} \, \text{cm}^2 \, \text{s}^{-1}$. The mass loading peaks for all runs after $\sim 30 \, \text{Myr}$ with $\eta \sim$ 3-8. There are no noticeable patterns that let conclude the strength of the peak depending on CR injection fraction and diffusion coefficients. The further evolution of η are comparable too, as for all runs after 70 Myr η fluctuates slightly below unity and only exceeds it at a few times.
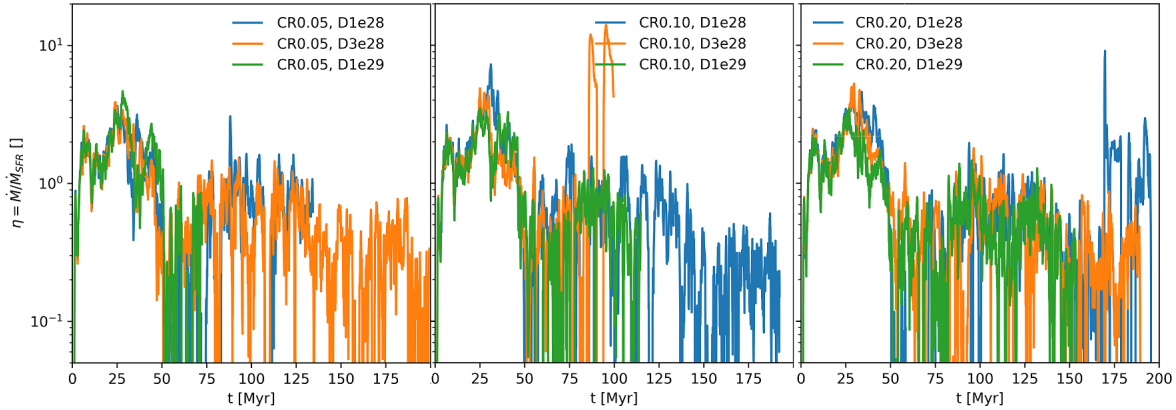
Figure 4.18: Time evolution of the mass loading factor at 1 kpc above and below the midplane.

We find similar behavior for the mass loading at 2 kpc above and below the midplane. There are also peaks at 10 and 40 Myr with comparable strengths for all runs with $\eta \sim$ 2.5-2.8 and $\eta \sim$1.5 respectively. Only the run INJ08 reaches higher values of $\eta \sim$ 2.4 at 40 Myr. Only a few times η again exceeds unity in later evolution.

Inside the inner region at 0.5 kpc above and below the midplane the mass loading exceeds unity for the first 45 Myr with a peak after 30 Myr at $\eta \sim$ 18-23. For the time span between 45 to 70-100 Myr there is only inwards falling gas, thus the mass loading becomes negative. After that time mass is accelerated outwards again which leads to a mass loading ~ 0.5.

As the mass loading factor strongly fluctuates, we further consider the time evolution of the total mass located above our reference boundary, shown in Figure 4.19. The panels show runs with identical CR injection fraction, increasing from left to right, and the corresponding diffusion coefficients are color coded. We find very comparable values for the first ~ 30 Myr after which the lines clearly separate. The runs with smallest diffusion coefficients (blue) drive slightly more mass above our boundary, in case of 10 and 20% CR injection fraction (central, right panel). Overall they are still very similar in shape and values. Therefore we conclude that the effect of different CR injection fractions and diffusion coefficients do not systematically determine the gas distribution and outflowing mass.

The mass fractions discussed before allow us to conclude what type of gas is flowing to the outer regions. The constantly increasing mass fraction of hot gas 2 kpc above and below the midplane implies the outflows mainly consist of hot gas. This statement is further supported for all runs by the 2D histograms the outwards pointing velocity and temperature given in Figure 4.20. We find two main regions in the histograms that contain most of the mass, the cold gas region at and slightly below 10^4 K ranging from several m s^{-1} up to 70 km s^{-1} driving the interior dynamics. The second one inside hot gas regions, which correspond to the low density gas (see Figure 4.9), centered at $\sim 10^{6.5}$ K at which the gas moves outwards with a few km s^{-1} up to 100 km s^{-1}. The low density gas is located
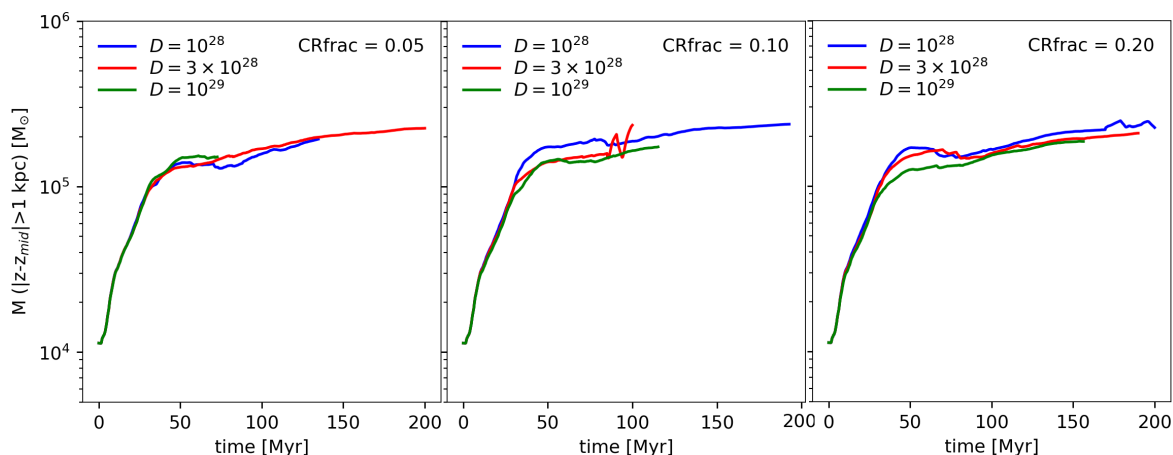
Figure 4.19: Time evolution of the total mass located in the outer regions $|z - z_{\mathrm{mid}}| > 1\,\mathrm{kpc}$.
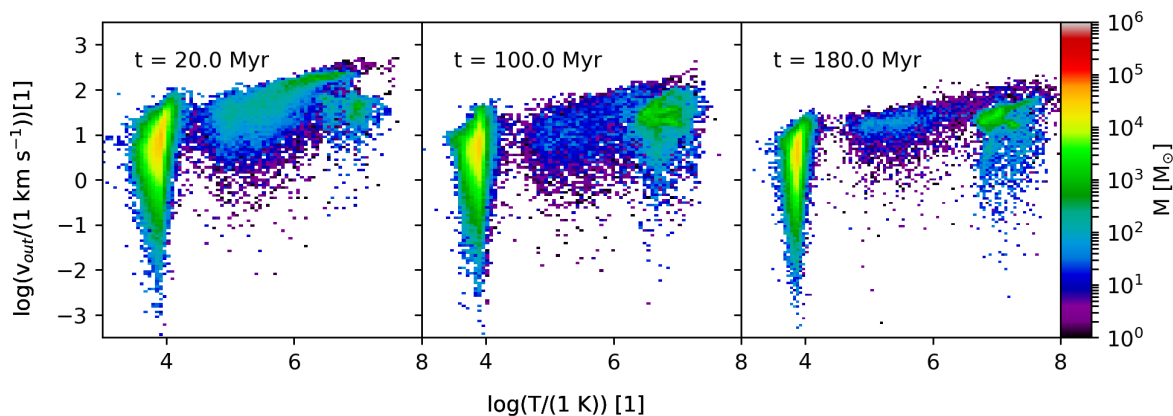

Figure 4.20: Time stamps of the mass weighted 2D histogram of the outflow velocity and temperature for the INJ04 run.

further away from the midplane region and hence the out flowing velocities are sufficient to drive the gas up to 2 kpc above and below midplane and beyond. Surprisingly the different CR injection fractions and diffusion coefficients seem to have only a minor impact on the outflow that reach 2 kpc and beyond.

4.5 Applied shock finder

As a further step we want to compare the previous results of CR injection at SNe to CR acceleration at SN remnant shocks. Therefore we apply the discussed shock finder (see section 2.4.4) to our setup. Figure 4.21 shows the detected shock zones (white contour) and surfaces (black contour) within the density plots for different simulation times. Further it includes plots of the strength of the shocks given by the Machnumber $\mathcal{M}$. At very early times (top panels) the detection is reasonable, although there are different detection arti-
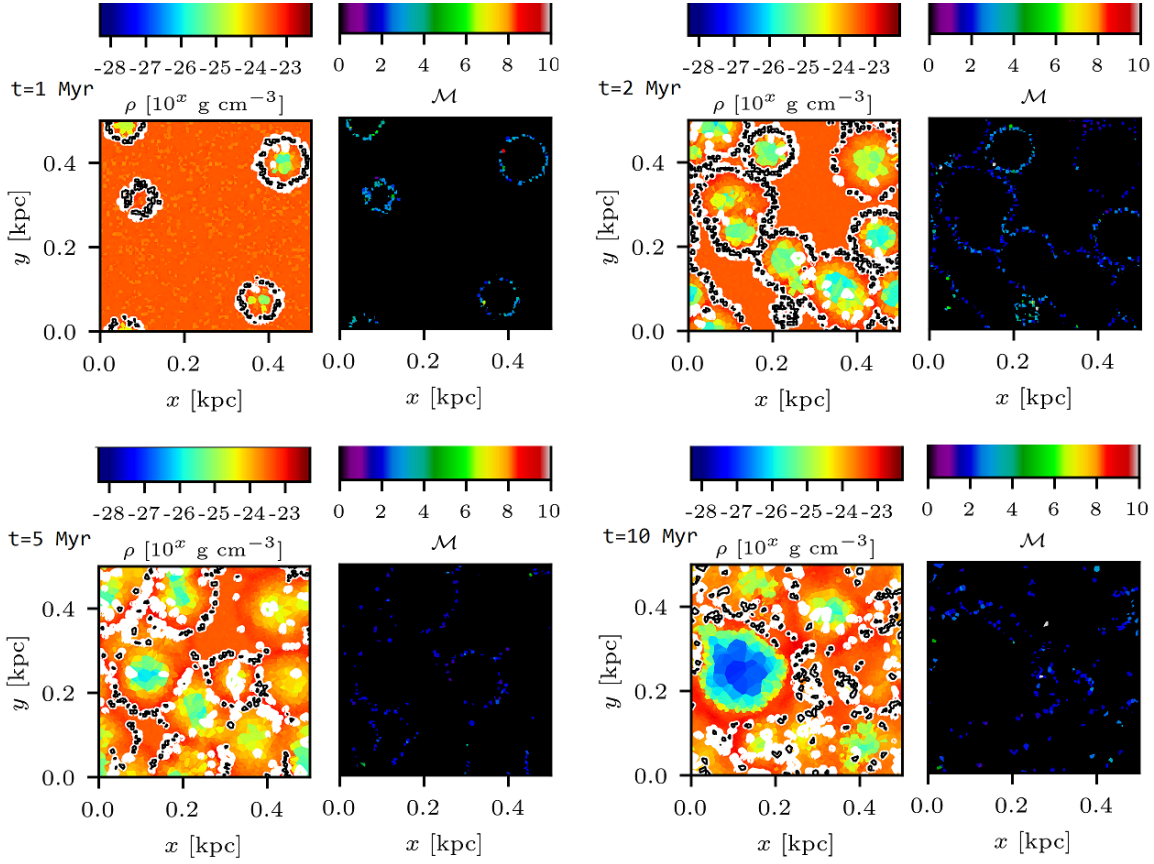
Figure 4.21: Shock detection within the galactic midplane at different times (top left): 1 Myr, (top right): 3 Myr, (bottom left): 5 Myr and (bottom right): 10 Myr of simulation SF01. Plot of the density and Machnumber slice through the midplane. The shock surface and zone are marked by the black and white contour lines within the density plot.

facts, such as unexpectedly broader and thinner shock zones and surfaces, represented by circles in the Machnumber plots. However, shortly after first structure formation (bottom panels) the detected shock zones contain an unexpectedly low numbered and unreasonable shock zones and surfaces. Therefore the provided shock finder is in first place applicable to our setup and causes no problems, but nevertheless it seems to need further development for such a highly dynamical environment. Further steps will included a detailed analysis of the shock finder procedure within highly dynamical test environments.

The output of the runs with shock finder are limited by their simulation time $\sim 40\,\text{Myr}$, as they take an enormous computational time. This can be explained by the thermal energy input that occupies the entire energy input, as the CRs are accelerated by the expanding shock waves. Therefore locally higher temperatures are reached that lead to very small time steps.

Within the $\sim 40\,\text{Myr}$ simulation time the SF runs yield comparable values in structure, CR energies and outflows to the runs with the CR injection. Therefore, even though the
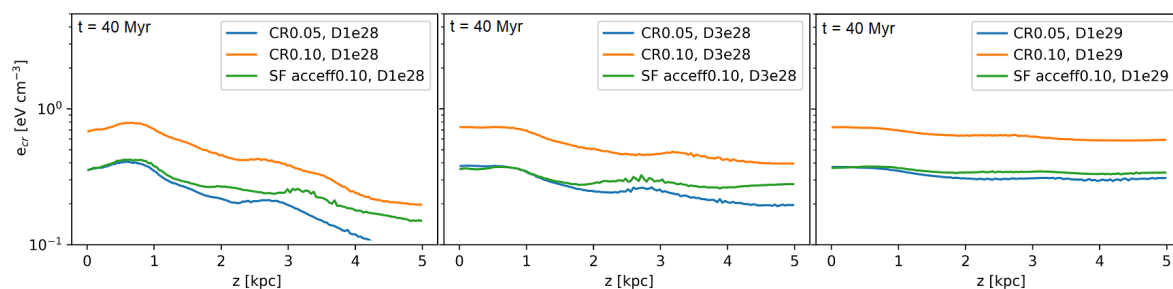
Figure 4.22: Volume weighted CR energy density as function of distance from the midplane. From left to right we plot the increasing diffusion coefficients. Different CR injection fractions and the shock acceleration efficiency are color coded.
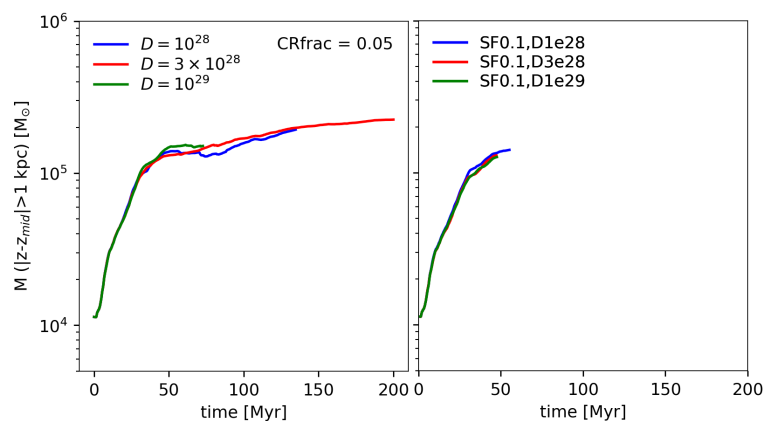

Figure 4.23: Gas mass located above our reference boundary of 1 kpc above and below the midplane for the 5% INJ (left panel) and SF runs (right panel).

shock finding routine has to be advanced, the application of this shock finding routine is reasonable. The correlation between the CR energy densities of the INJ runs and SF runs is shown in Figure 4.22. The panels show the runs with equal diffusion coefficient, increasing from left to right, and further include the 5 and 10% CR injection fraction runs as well as the corresponding shock finder runs, given by the color. The energy density of the CRs in the SF runs settles in between the two CR injection fraction runs, but slightly closer to the 5% runs. This is true for all three diffusion coefficients.

In case of the smallest diffusion coefficient (left panel), the CRs occupy a slightly larger energy density. This can be explained by shocks of infalling gas, detected in the outer regions. The higher the diffusion coefficient the less the difference between the 5% INJ runs and the corresponding SF run.

Concerning the outflows driven by the SF runs, they are very similar to the 5% injection runs. The similarity is shown in Figure 4.23. The left panel shows the mass located above our reference boundary at 1 kpc above and below the midplane for the 5% CR injection runs and the right panel for the SF runs. There are no noticeable differences between the CR injection and the SF runs.

However with the artifacts within the shock zone and surface shown in Figure 4.21 and limited simulation time these are only first results that need further development. Removing the artifacts and further optimize the run time this work builds the bases of future work.

5 Discussion

ISM phases

For all our runs we yield similar disk structures which are comparable to Girichidis et al. (2016a), even though we do not form molecular gas and high densities. Comparing the VFFs they are identical for all our runs. The overall state of hot gas filling most of the volume is the same as in Li et al. (2017); Pardi et al. (2017). But the molecular, cold and warm VFFs, to which we all refer to as cold gas with $T < 8000\,\mathrm{K}$, fill up a significant amount of volume with summed up VFFs $\sim$ 0.1-0.2. In comparison we find a cold gas VFF of < 0.04. Both our and their values show a decreasing value over time, but nevertheless our cold gas VFFs do not get comparable to theirs. This for sure can be partially explained by the missing of efficient cooling at lower temperatures $T \sim 10^{3-4}\,\mathrm{K}$, but not fully. Inside the disk region however we yield comparable values for the hot gas as Girichidis et al. (2018a).

Magnetic field

Our initial magnetic field evolves relatively stable inside the disk, the inner region and with respect to the entire box. In the outer regions the mass weighted field strength constantly increases and cool and warm gaseous outflows further lead to a steep increase. In the middle region we find a strongly tied evolution to gas dynamics as the magnetic field strength first steeply rises and then drops of again. However, other studies find magnetic field strength to slightly increase (Girichidis et al., 2018b) or show a more stable evolution (Pardi et al., 2017) with respect to the entire box.

CR distribution and energies

We find a CR scale height, which corresponds to 70% of integrated CR energy, of $\sim$ 3-3.5 kpc above the midplane, which is slightly smaller than the region occupied by CRs, traced by the $\mathrm{Be}^{10}/\mathrm{Be}^9$ ratio, up to 4-10 kpc (Grenier et al., 2015). However, these values are for entire galaxies and still uncertain (Strong et al., 2007; Putze et al., 2010; Trotta et al., 2011).

Within the inner region we find comparable small values of the ratio of CR to thermal pressure X_{cr} to other studies (Girichidis et al., 2016a), i.e. a factor 10-100 less, as our cooling becomes inefficient at temperatures $T \sim 10^4\,\mathrm{K}$ and below. Inside the disk our runs with 20% CR injection fraction yield similar values $X_{\mathrm{cr}} \sim 1$, but in Girichidis et al. (2018a) they used only 10% CR injection, which again stresses the importance of cooling. Nevertheless in the hot outer regions, we find the thermal pressure to dominate the CR

pressure by a factor of 5-20, the results differ even more as Girichidis et al. (2018a) found the CR pressure to be 10-100 times the thermal pressure. This can be explained by the temperature differences in the outflows we drive (see below).

Regarding the CR energies we find larger diffusion coefficients to slightly increase the CR energies at a given time and with the largest diffusion coefficient $D = 10^{29}\,cm^2\,s^{-1}$ even exceed the theoretical input. To our knowledge this phenomenon has not been reported yet and therefore we carefully use our explanation from above. However this would need further individual testing of the suspected effect.

We find the total loss percentage of CR energy by CR cooling to increase with time up to 15% and is stronger for smaller diffusion coefficients. This is in agreement with the results of Girichidis et al. (2018a), where they found stronger hadronic losses for smaller diffusion coefficients that add up to 5-25% of the injected CR energy. However, to our knowledge there are no observational constrains on the CR energy loss via hadronic interactions.

Outflows

We find mainly hot gas $10^5 < T < 5 \times 10^8\,K$ being ejected from the surrounding region of the galactic disk and no systematic outflows of cold and warm gas. This is quite different from Girichidis et al. (2018a) as they found their outflow to be around $T \sim 10^4\,K$ but partially in agreement with results from Li et al. (2017) as their main outflowing mass is within a hot phase $T > 10^5\,K$ similar to our hot phase.

Concerning the mass evolution above our reference boundary we find differences in the diffusion coefficients, as the runs with smaller coefficient yield slightly larger values than the larger ones at times $\sim 70\,Myr$. This is in agreement to previous studies by (Girichidis et al., 2018a). In outer regions this effect becomes smaller. In the inner regions at $\pm 0.5\,kpc$ reference we find a comparable evolution of mass located above the reference independent of CR injection fraction and diffusion coefficient.

Overall our mass loading factors are within the range of other studies on galactic scales (Creasey et al., 2013) and smaller but still comparable on local scales (Girichidis et al., 2018a), i.e. similar setups of stratified boxes.

Applied shock finder

To our knowledge nobody has applied a comparable shock finding routine to a similar setup yet. Our time restricted results show comparable structures and values of this first shock finder application in such a high dynamical environment. The overall CR energy is similar as the volume weighted CR energy distribution along the z-coordinate settles between the 5 and 10% CR injection runs with a tendency to the 5% ones. The early outflows are of comparable strength. However this routine needs further development as the simulation time is limited and artifacts in the shock zone and surface originate from the highly dynamical environments.

Caveats

Overall our results with respecting given limitations are on the same orders of magnitude as other studies. Nevertheless these limitations are essential to further develop more physically reasonable setups. First of all the efficiency of our cooling does not allow for the formation of very cold gas as this would require the inclusion of molecular gas, thus including and modeling chemistry could be one of the next steps to improve the simulations. This would further allow the usage of a background stellar radiation field (UV) which is shielded by high density regions and further induces new processes to be modeled such as photo dissociation.

Additionally we do not model self-gravity of the gas and proper star formation. The formation of stars and including momentum and mass transfer of SN explosions would be a further step.

6 Conclusion

We started this work by building up initial conditions that allow an immediate simulation start in AREPO with cells that do not need to be adapted in first place. To investigate the effect of the diffusion coefficient and the CR injection fraction and perhaps constrain them, we ran a full set of nine simulations varying both parameters in a stratified box with an external gravitational potential and conditions similar to the solar neighborhood. We improved the code performance as we further added a gradient based refinement criterion to the refinement scheme and limited the temperature of the cells, among which the SNe energy is distributed. Additionally, we applied a shock finding procedure in three runs to make the first steps and build a foundation to a complete comparison between the two coexisting models of CR injection in SNe and their acceleration in the resulting shock waves.

We find all our runs to produce reasonable gas structures and phases, as far our modeling allows, as we neither include self gravity nor molecular cooling that would result in very cold gas regions. This lack of efficient cooling at low temperatures $T < 10^4$ K is likely to explain the differences to other studies (see above) in all cases.

Regarding the CRs, we find the diffusion coefficient to mainly influence the CR scale height within the first 150 Myr, after which the scale heights become very similar, independent of the CR injection fraction. The CR injection fraction itself regulates the CR energy distribution along the z-coordinate, where we reach volume weighted average values of up to 3-4 eV cm^{-3}, for 20% injection fraction, that are only slightly effected by the diffusion coefficient.

Furthermore, all simulations are able to drive outflows that are comparable in strength $\eta \sim 0.1$-8 to previous studies. However in contrast to them, we do find hot gas occupying the largest amount of gas that is driven outwards. The smaller diffusion coefficients drive slightly more mass over time through our selected reference boundaries.

Within the limited simulation time of the application of the shock finder, we find comparable gas structures and outflow behavior to the runs with the CR injection scheme. This stresses that the used shock finder is indeed applicable to such a setup in first place. Nevertheless the ISM is highly dynamical environment in which the used shock finder is not able to perform at its best without further adaptation.

Thus with the gained knowledge of the critical points this work lays down a foundation and a guidance for next steps to be performed in order to advance the used shock finding procedure and compare the two existing models of CR energy gain.

Bibliography

Ackermann M., Ajello M., Allafort A., et al., 2013, Science, 339, 6121, 807

Aumer M., White S. D., Naab T., 2014, Monthly Notices of the Royal Astronomical Society, 441, 4, 3679

Axford W., Leer E., Skadron G., 1977, Plovdiv, 11, 132

Baade W., Zwicky F., 1934, Physical Review, 46, 1, 76

Beck R., Wielebinski R., 2013, Planets, Stars and Stellar Systems: Volume 5: Galactic Structure and Stellar Populations, 641–723

Bell A., 1978, Monthly Notices of the Royal Astronomical Society, 182, 2, 147

Binney J., 2008, HB). Published by Princeton University Press, Princeton, NJ USA, 2008

Blandford R. D., Ostriker J. P., 1978, The Astrophysical Journal, 221, L29

Blasi P., 2013, The Astronomy and Astrophysics Review, 21, 1, 70

Blitz L., Fukui Y., Kawamura A., Leroy A., Mizuno N., Rosolowsky E., 2006, arXiv preprint astro-ph/0602600

Boulares A., Cox D. P., 1990, The Astrophysical Journal, 365, 544

Breitschwerdt D., McKenzie J., Völk H., 1993, Astronomy and Astrophysics, 269, 54

Carilli C., Dwarakanath K., Goss W. M., 1998, The Astrophysical Journal Letters, 502, 1, L79

Caselli P., Walmsley C., Terzieva R., Herbst E., 1998, The Astrophysical Journal, 499, 1, 234

Chevalier R. A., 1977, Annual Review of Astronomy and Astrophysics, 15, 1, 175

Chisholm J., Matsushita S., 2016, The Astrophysical Journal, 830, 2, 72

Chisholm J., Tremonti C. A., Leitherer C., Chen Y., 2017, Monthly Notices of the Royal Astronomical Society, 469, 4, 4831

Clarke C., Oey M. S., 2002, Monthly Notices of the Royal Astronomical Society, 337, 4, 1299

Contursi A., Poglitsch A., Carpio J. G., et al., 2013, Astronomy & Astrophysics, 549, A118

Cowie L., Songaila A., York D., 1979, The Astrophysical Journal, 230, 469

Cox D. P., 2005, Annu. Rev. Astron. Astrophys., 43, 337

Cox D. P., Smith B. W., 1974, The Astrophysical Journal, 189, L105

Creasey P., Theuns T., Bower R. G., 2013, Monthly Notices of the Royal Astronomical Society, 429, 3, 1922

de Avillez M. A., Breitschwerdt D., 2004, Astronomy & Astrophysics, 425, 3, 899

de Avillez M. A., Breitschwerdt D., 2005, Astronomy & Astrophysics, 436, 2, 585

Dorfi E., Breitschwerdt D., 2012, Astronomy & Astrophysics, 540, A77

Enßlin T. A., Pfrommer C., Springel V., Jubelgas M., 2007, Astronomy & Astrophysics, 473, 1, 41

Ferriere K. M., 2001, Reviews of Modern Physics, 73, 4, 1031

Field G., Goldsmith D., Habing H., 1969, The Astrophysical Journal, 155, L149

Flynn C., Holmberg J., Portinari L., Fuchs B., Jahreiß H., 2006, Monthly Notices of the Royal Astronomical Society, 372, 3, 1149

Gaensler B., Madsen G., Chatterjee S., Mao S., 2008, Publications of the Astronomical Society of Australia, 25, 4, 184

Gatto A., Walch S., Low M.-M. M., et al., 2015, Monthly Notices of the Royal Astronomical Society, 449, 1, 1057

Gatto A., Walch S., Naab T., et al., 2016, Monthly Notices of the Royal Astronomical Society, 466, 2, 1903

Gatto A., Walch S., Naab T., et al., 2017, Monthly Notices of the Royal Astronomical Society, 466, 2, 1903

Geen S., Rosdahl J., Blaizot J., Devriendt J., Slyz A., 2015, Monthly Notices of the Royal Astronomical Society, 448, 4, 3248

Genzel R., Schreiber N. F., Rosario D., et al., 2014, The Astrophysical Journal, 796, 1, 7

Girichidis P., Naab T., Hanasz M., Walch S., 2018a, Monthly Notices of the Royal Astronomical Society, 479, 3, 3042

Girichidis P., Naab T., Walch S., et al., 2016a, The Astrophysical Journal Letters, 816, 2, L19

Girichidis P., Seifried D., Naab T., et al., 2018b, Monthly Notices of the Royal Astronomical Society, 480, 3, 3511

Girichidis P., Walch S., Naab T., et al., 2016b, Monthly Notices of the Royal Astronomical Society, 456, 4, 3432

Glover S. C., Clark P. C., 2012, Monthly Notices of the Royal Astronomical Society, 421, 1, 9

Gnat O., Ferland G. J., 2012, The Astrophysical Journal Supplement Series, 199, 1, 20

Gould R., 1972, Physica, 58, 3, 379

Grenier I. A., Black J. H., Strong A. W., 2015, Annual Review of Astronomy and Astrophysics, 53, 199

Haffner L., Dettmar R.-J., Beckman J., et al., 2009, Reviews of Modern Physics, 81, 3, 969

Haid S., Walch S., Naab T., Seifried D., Mackey J., Gatto A., 2016, Monthly Notices of the Royal Astronomical Society, 460, 3, 2962

Hanasz M., Lesch H., Naab T., Gawryszczak A., Kowalik K., Wóltański D., 2013, The Astrophysical Journal Letters, 777, 2, L38

Heckman T. M., Alexandroff R. M., Borthakur S., Overzier R., Leitherer C., 2015, The Astrophysical Journal, 809, 2, 147

Heckman T. M., Lehnert M. D., Strickland D. K., Armus L., 2000, The Astrophysical Journal Supplement Series, 129, 2, 493

Heckman T. M., Thompson T. A., 2017, Handbook of Supernovae, 1–24

Heiles C., 1987, The Astrophysical Journal, 315, 555

Helder E., Vink J., Bykov A., Ohira Y., Raymond J., Terrier R., 2012, Space Science Reviews, 173, 1-4, 369

Heyer M. H., Brunt C., Snell R. L., Howe J. E., Schloerb F. P., Carpenter J. M., 1998, The Astrophysical Journal Supplement Series, 115, 2, 241

Hong S. E., Ryu D., Kang H., Cen R., 2014, The Astrophysical Journal, 785, 2, 133

Hopkins P. F., Kereš D., Oñorbe J., et al., 2014, Monthly Notices of the Royal Astronomical Society, 445, 1, 581

Hoyle F., Ellis G., 1963, Australian Journal of Physics, 16, 1, 1

Hu C.-Y., Naab T., Walch S., Glover S. C., Clark P. C., 2016, Monthly Notices of the Royal Astronomical Society, 458, 4, 3528

Isenberg P. A., 1997, Journal of Geophysical Research: Space Physics, 102, A3, 4719

Jenkins E. B., 2013, The Astrophysical Journal, 764, 1, 25

Joung M. R., Mac Low M.-M., Bryan G. L., 2009, The Astrophysical Journal, 704, 1, 137

Jubelgas M., Springel V., Enßlin T., Pfrommer C., 2008, Astronomy & Astrophysics, 481, 1, 33

Kennicutt Jr R. C., 1998, The Astrophysical Journal, 498, 2, 541

Kennicutt Jr R. C., Edgar B. K., Hodge P. W., 1989, The Astrophysical Journal, 337, 761

Kim C.-G., Kim W.-T., Ostriker E. C., 2011, The Astrophysical Journal, 743, 1, 25

Kim C.-G., Ostriker E. C., 2018, The Astrophysical Journal, 853, 2, 173

Kim C.-G., Ostriker E. C., Kim W.-T., 2013, The Astrophysical Journal, 776, 1, 1

Klessen R. S., Glover S. C., 2016, in Star Formation in Galaxy Evolution: Connecting Numerical Models to Reality, 85–249, Springer

Krumholz M. R., McKee C. F., 2005, The astrophysical journal, 630, 1, 250

Krumholz M. R., Thompson T. A., 2007, The Astrophysical Journal, 669, 1, 289

Kulkarni S. R., Heiles C., 1987, in Interstellar processes, 87–122, Springer

Kulsrud R., Pearce W. P., 1969, The Astrophysical Journal, 156, 445

Leroy A. K., Walter F., Martini P., et al., 2015, The Astrophysical Journal, 814, 2, 83

Li M., Bryan G. L., Ostriker J. P., 2017, The Astrophysical Journal, 841, 2, 101

Macdonald J. R., Brown M. D., 1972, Physical Review Letters, 29, 1, 4

Mannheim K., Schlickeiser R., 1994, Interactions of cosmic ray nuclei, Tech. rep.

Marinacci F., Pakmor R., Springel V., 2013, Monthly Notices of the Royal Astronomical Society, 437, 2, 1750

McKee C. F., Ostriker J. P., 1977, The Astrophysical Journal, 218, 148

McKee C. F., Williams J. P., 1997, The Astrophysical Journal, 476, 1, 144

Meyer J.-P., Drury L. O., Ellison D. C., 1997, The Astrophysical Journal, 487, 1, 182

Mierkiewicz E., Reynolds R., Roesler F., Harlander J., Jaehnig K., 2006, The Astrophysical Journal Letters, 650, 1, L63

Miller G. E., Scalo J. M., 1979, The Astrophysical Journal Supplement Series, 41, 513

Miyoshi T., Kusano K., 2005, Journal of Computational Physics, 208, 1, 315

Morlino G., Caprioli D., 2012, Astronomy & Astrophysics, 538, A81

Navarro J. F., Frenk C. S., White S. D., 1997, The Astrophysical Journal, 490, 2, 493

Newman S. F., Genzel R., Förster-Schreiber N. M., et al., 2012, The Astrophysical Journal, 761, 1, 43

Padoan P., Pan L., Haugbølle T., Nordlund Å., 2016, The Astrophysical Journal, 822, 1, 11

Pakmor R., Pfrommer C., Simpson C. M., Kannan R., Springel V., 2016, Monthly Notices of the Royal Astronomical Society, 462, 3, 2603

Pardi A., Girichidis P., Naab T., et al., 2017, Monthly Notices of the Royal Astronomical Society, 465, 4, 4611

Pettini M., Shapley A. E., Steidel C. C., et al., 2001, The Astrophysical Journal, 554, 2, 981

Pfrommer C., Ensslin T. A., 2004, Astronomy & Astrophysics, 413, 1, 17

Pfrommer C., Pakmor R., Schaal K., Simpson C., Springel V., 2016, Monthly Notices of the Royal Astronomical Society, 465, 4, 4500

Pineda J. L., Langer W. D., Velusamy T., Goldsmith P. F., 2013, Astronomy & Astrophysics, 554, A103

Putze A., Derome L., Maurin D., 2010, Astronomy & Astrophysics, 516, A66

Rahner D., Pellegrini E. W., Glover S. C., Klessen R. S., 2017, Monthly Notices of the Royal Astronomical Society, 470, 4, 4453

Ramaty R., Kozlovsky B., Lingenfelter R. E., Reeves H., 1997, The Astrophysical Journal, 488, 2, 730

Reynolds R., 1989, The Astrophysical Journal, 339, L29

Reynolds R., Scherb F., Roesler F., 1973, The Astrophysical Journal, 185, 869

Rogers H., Pittard J., 2013, Monthly Notices of the Royal Astronomical Society, 431, 2, 1337

Rupke D. S., Veilleux S., Sanders D., 2005, The Astrophysical Journal Supplement Series, 160, 1, 87

Ryu D., Kang H., Hallman E., Jones T., 2003, The Astrophysical Journal, 593, 2, 599

Salpeter E. E., 1955, The Astrophysical Journal, 121, 161

Schaal K., Springel V., 2014, Monthly Notices of the Royal Astronomical Society, 446, 4, 3992

Schaye J., Crain R. A., Bower R. G., et al., 2014, Monthly Notices of the Royal Astronomical Society, 446, 1, 521

Schlickeiser R., 1989, The Astrophysical Journal, 336, 243

Shapiro M. M., 1999, in LiBeB Cosmic Rays, and Related X-and Gamma-Rays, vol. 171, 138

Simpson C. M., Pakmor R., Marinacci F., et al., 2016, The Astrophysical Journal Letters, 827, 2, L29

Skilling J., 1975, Monthly Notices of the Royal Astronomical Society, 172, 3, 557

Skillman S. W., O'Shea B. W., Hallman E. J., Burns J. O., Norman M. L., 2008, The Astrophysical Journal, 689, 2, 1063

Springel V., 2010, Monthly Notices of the Royal Astronomical Society, 401, 2, 791

Springel V., Pfrommer C., Girichidis P., 2019, Lecture notes for Modern Computational Astrophysics: Concepts and Applications

Strong A. W., Moskalenko I. V., Ptuskin V. S., 2007, Annu. Rev. Nucl. Part. Sci., 57, 285

Tammann G., Loeffler W., Schroeder A., 1994, The Astrophysical Journal Supplement Series, 92, 487

Thomas T., Pfrommer C., 2019, Monthly Notices of the Royal Astronomical Society, 485, 3, 2977

Toro E., Billett S., 1997, IMA journal of numerical analysis, 17, 1, 61

Trotta R., Jóhannesson G., Moskalenko I., Porter T., De Austri R. R., Strong A., 2011, The Astrophysical Journal, 729, 2, 106

Veilleux S., Cecil G., Bland-Hawthorn J., 2005, Annu. Rev. Astron. Astrophys., 43, 769

Walch S., Girichidis P., Naab T., et al., 2015, Monthly Notices of the Royal Astronomical Society, 454, 1, 238

Weiß A., Walter F., Neininger N., Klein U., 1999, arXiv preprint astro-ph/9904081

Wolfire M. G., McKee C. F., Hollenbach D., Tielens A., 2003, The Astrophysical Journal, 587, 1, 278

Zank G., Lu J., Rice W., Webb G., 2000, Journal of plasma physics, 64, 4, 507

Zank G. P., 2014, Lect. Notes Phys., 877, 1

Zweibel E. G., 2013, Physics of Plasmas, 20, 5, 055501

Zweibel E. G., 2017, Physics of plasmas, 24, 5, 055402